Mapping the Universe with weak lensing

by

Benjamin Samuel Mawdsley

This thesis is submitted in partial fulfilment of
the requirements for the award of the degree of
Doctor of Philosophy of the University of Portsmouth.

Abstract

Cosmological observations have led to the development of a standard model of cosmology, known as ΛCDM. In this model, we believe the majority of the Universe consists of matter and energy which does not interact electromagnetically, and the main challenge to the field is how to detect these invisible, yet dominant components of the Universe.

One avenue lies in the fact that the dark matter does feel the force of gravity. Furthermore, gravitational potentials influence the path of photons in such a way that images become distorted, in an effect known as gravitational lensing. Through the use of gravitational lensing, dark matter can be detected despite it being non luminous, as it is believed to constitute the majority of the matter in the Universe. Using measurements of lensing across large areas of the sky, it is possible to produce maps of the dark matter.

In this thesis, I present mass maps that have been made using lensing measurements from a leading current experiment, the Dark Energy Survey. I develop a new pipeline to produce these mass maps in a more accurate way, thoroughly testing them using a wide range of statistics. I also present work that analyses how these mass maps can be used to provide us with constraints on the fundamental properties of the Universe, through measuring the topology of the maps, and find that such an approach can lead to improving cosmological constraints. Finally, I present work examining the immediate future of the field of mass mapping, evaluating the likely quality of the next generation of mass maps and the extent to which they can improve our knowledge of the Universe.

Table of Contents

List of Figures

Declaration

Whilst registered as a candidate for the above degree, I have not been registered for any other research award. The results and conclusions embodied in this thesis are the work of the named candidate and have not been submitted for any other academic award.

Word count: 34,409 words.

Acknowledgements

This thesis would not have been possible without the help and support of many people, and I will try and acknowledge as many of them as I can here.

Firstly, my thanks go to my supervisor David for everything he has done to help me over the previous four years. When I started my PhD, I knew next to nothing about weak lensing and mass mapping, and it is predominantly thanks to him that I now know slightly more. Diligent in his duties and a motivating, educational colleague, I could not have asked for a better supervisor. My thanks also go to Chihway Chang, who has helped me in the Dark Energy Survey, and to Gary Burton, who enabled many of the super-computing applications presented within this thesis.

When I think of my time as a PhD student at the ICG, it is the people that I shared my time with that come to mind first, and to my colleagues I express my thanks for making my time there such a stimulating, fun and engaging place to study. I am grateful to those in my year - Ben, Marco, Paul, Pier, Rob, Taniya and honorary member Michael, for sharing the experience with me, and to Dan and Matt for introducing me to the Portsea Beer Festival and many fantastic pubs in Portsmouth.

Finally, my utmost thanks go to my family. To Kariza, for her love and support and fantastic choice of colour schemes. To Mum, Dad, Thomas and Nanna, for their continuing support and unrelenting encouragement that I will succeed, despite not being entirely sure exactly what it is I am doing. For Grandma and Grandad. I could not have done it without you all.

Dissemination

Chapter 2 includes work originally presented in Chang et al. (2018).
The work presented in Chapter 3 was originally presented in Mawdsley et al. (2019).
Chapters 4 and 5 contain original work that is in preparation for publication.

Acronyms and Abbreviations

2LPT - 2nd order Lagrangian Perturbation theory

BAO - Baryon Acoustic Oscillations

BPZ - Bayesian Photometric redshift

CALCLENS - Curved sky gravitational lensing for cosmological lightcone simulations

CCD - Charge coupled device

CFHTLenS - Canada France Hawaii Telescope Lensing Survey

COLA - Comoving Lagrangian acceleration

COSMOS - Cosmic evolution survey

CMB - Cosmic Microwave Background

DES - The Dark Energy Survey

DES SV - Dark Energy Survey Science Verification data

FF - Forward fitted maps

HSC - Hyper Suprime Cam

IA - Intrinsic alignment

KiDS - Kilo-Degree Survey

KS - the Kaiser-Squires direct inversion technique for producing mass maps

MCMC - Markov Chain Monte Carlo

MACHOs - Massive Astrophysical Compact Halo Objects

PDF - Probability Distribution Function

PSF - Point Spread Function

RedMaGiC - Red-sequence matched-filter Galaxies Catalog

RedMaPPer - Red-sequence matched-filter Probabalistic Percolation clus-

ter finder

RSD - Redshift space distortions

SHAM - Subhalo abundance matching

S/N or SNR - Signal to noise ratio

WIMPs Weakly Interacting Massive Particles

Y1/Y3 - denotes years of DES data

z - denotes redshift

Λ**CDM** - Cosmological model including a dark energy component and cold dark matter.

Chapter 1

Cosmology

1.1 Introduction to the current paradigm

Cosmology has a history as old as the first humans gazing upwards at the sky and pondering our place in it. Creation myths regarding the cosmos, and the place of humanity in it, arise across civilisations. These speak to a shared human curiosity asking fundamental questions about the Universe, and as technology has improved, so have our answers.

The field has matured to such a stage that we now believe that we have the broad strokes defining the history of the Universe, from the first fractions of a second until the present day. Briefly, our standard model begins with an incredibly hot and dense plasma which undergoes a period of rapid, exponential expansion. Once this exponential expansion ceases, the Universe continues to grow and particles form. Once the Universe is sufficiently cool, electrons can bind to protons and atoms can be formed. These are predominantly hydrogen but also some helium and a fraction of lithium. After this happens, photons stop interacting with the matter as frequently and are able to stream freely through the Universe, releasing the radiation we observe known as the cosmic microwave background, or CMB.

We see more than hydrogen, helium and lithium in the Universe, so that is only the beginning of the story. Following this process, there is a prolonged

period of structure growth where the gravitational pull of massive objects pulls material together to form areas of greater and greater over-density, until these reach the point that gravitational collapse causes sufficient pressure for stars to form, and eventually galaxies. The over-densities formed at this early time define the growth of the earliest galaxies, and we will see how the structure we observe today can give us information about the Universe at the earliest times. Billions of years of growth and complex physical interactions result in the vast web of structure that we see when mapping galaxies in the sky, and cosmology today aims to question the beginnings and foundation of the Universe using observations we can make today. Being able to model the Universe across such a range of scales, times and regimes is an amazing achievement of human understanding, to which this thesis aims to add a small contribution.

1.1.1 Modern cosmology

Cosmology today is built upon two key assumptions, which can crucially be tested observationally. These are:

Isotropy - the assumption that on sufficiently large scales the Universe looks the same in all directions. Equally, this is a statement that there is no preferential direction in the Universe.
Homogeneity - the assumption that, on sufficiently large scales, properties such as density are uniform. On such scales, observations of galaxy distributions will appear uniform.

These assumptions are supported by observations, where large scale structure indicate that the distribution of galaxies becomes uniform at large scales, in all directions. A Universe could be isotropic, but not homogeneous, (e.g spherically symmetrical around the observer), but insisting that both are true will constrict the range of cosmological models possible. Isotropy can be directly observed through observations on Earth, but direct observational

proof of homogenity requires observers from two different locations both detecting isotropy. We currently infer homogeneity from observations of the cosmos at the largest scales, through combining the philosophical statement of the Copernican principle that "we are not privileged observers" to observed isotropy. These two assumptions applied together are carried to profound conclusions to derive the equations that we believe govern the motion of the Universe.

1.2 The cosmological model

The Universe is described mathematically by the Friedmann-Lemaître- Robertson Walker metric. This model is built upon the two key assumptions of isotropy and homogeneity, and I will show in this section how we can build the equations necessary to describe the evolution of the Universe using these assumptions in conjunction with a theory of gravitation.

Metric

Measurement of distances in the Universe require the adoption of a metric. On a flat two dimensional surface, the distance between two points in described by the familiar Pythagoras' theorem:

$$\mathrm{d}s^2 = \mathrm{d}x^2 + \mathrm{d}y^2 \tag{1.1}$$

where the coordinates are given in x, y coordinates and the total distance is s. This definition can be seen as a specific case of a more general definition of distance if we introduce the concept of a metric, which maps differences in coordinates to a distance. Introducing the Einstein summation convention, such that the presence of an index appearing once in subscript and once in superscript implies summation, distances could be more generally described as

$$\mathrm{d}s^2 = g_{\alpha\beta}\mathrm{d}x^\alpha x^\beta. \tag{1.2}$$

If $g_{\alpha\beta} = \delta_{\alpha\beta}$ then we can see that we recover the same distance measure as described in equation 1.1. However, this description allows for a much broader range of definitions of distance and can be expanded to as many dimensions as desired.

General relativity considers the Universe as having 4 dimensions - x^0 describing a time coordinate and $x^{1,2,3}$ describing spatial coordinates. There are a range of possible metrics that could be made in this coordinate system, but the imposition of homogeneity and isotropy constrain these possibilities.

The metric $g_{\alpha\beta}$ has 16 components, considering there are 4 dimensions in space time. The term g_{00} can be found by considering the interval between two events that appear to occur in the same location for a fundamental observer, so the interval observed across all spatial coordinates is equal to 0. This means that the interval is

$$\mathrm{d}s^2 = g_{00}\mathrm{d}t^2 \tag{1.3}$$

and g_{00} can be set to c^2.

Following Bartelmann & Schneider (2001), the spatial part of the metric can be allowed to expand or contract, but it is necessary that this expansion is only a function of time. Otherwise, different spatial locations would expand at different rates and the assumptions of isotropy and homogeneity would be violated. Distance in this scenario would be described as

$$\mathrm{d}s^2 = c^2\mathrm{d}t^2 - a^2(t)\mathrm{d}l^2 \tag{1.4}$$

where we have introduced the function $a(t)$ to describe the rate of expansion and $\mathrm{d}l^2$ refers to the spatial distance. There are many possible forms that the metric used to calculate $\mathrm{d}l^2$ could take which depend upon the underlying geometry of the Universe. A general form of the metric when considered in spherical coordinates is

$$\mathrm{d}l^2 = \mathrm{d}w^2 + f_K^2(w)(\mathrm{d}\phi^2 + \sin^2\theta\mathrm{d}\theta^2) \tag{1.5}$$

for a point at a radial distance w from an origin, with angular coordinates ϕ, θ. The function f_K can change depending upon the geometry being de-

scribed, with the different scenarios shown in equation 1.6, following the convention in Bartelmann & Schneider (2001). The constraints we impose on our cosmological model means that this function can take three forms; trigonometric, linear or hyperbolic functions of w, which correspond to an overall curvature that is positive, zero or negative.

$$f_k = \begin{cases} K^{-1/2}\sin(K^{1/2}w) & (K > 0) \\ w & (K = 0) \\ (-K)^{1/2}\sinh((-K)^{1/2}w) & (K < 0) \end{cases} \tag{1.6}$$

1.2.1 Expansion of the Universe

The remaining part of the equation that needs constraining is the form of the expansion factor $a(t)$. For a description of the relationship between matter and the curvature of space time, we turn to General Relativity, which provides a relationship between the matter density and a curvature in the metric describing the Universe. This is expressed through the Einstein field equations (Einstein, 1915; Peacock, 1998)

$$G_{\alpha\beta} = \frac{8\pi G}{c^2}T_{\alpha\beta} + \Lambda g_{\alpha\beta} \tag{1.7}$$

where $G_{\alpha\beta}$ is introduced as the Einstein tensor, $T_{\alpha\beta}$ is the stress energy tensor and Λ was introduced to allow for static solutions to the equations on cosmological scales. Today, Λ is more commonly known as the cosmological constant and is believed to drive the expansion of the Universe. The stress energy tensor describes the motion of the energy contents in the Universe, and the Einstein tensor describes the curvature of the underlying metric.

The form that the stress energy tensor can take can be constrained to that of a perfect fluid, and results in finally reaching the Friedmann equation (Friedmann, 1922; Dodelson, 2003; Peacock, 1998) to describe the expansion of the Universe.

$$\left(\frac{\dot{a}}{a}\right)^2 = \frac{8\pi G}{3}\rho - \frac{Kc^2}{a^2} + \frac{\Lambda}{3} \tag{1.8}$$

The Friedmann equation therefore shows the velocity of the expansion of the Universe directly related to a combination of the matter density present, the curvature K and the cosmological constant. A further Friedmann equation relates the acceleration of the expansion factor by

$$\frac{\ddot{a}}{a} = -\frac{4}{3}\pi G\left(\rho + \frac{3p}{c^2}\right) + \frac{\Lambda}{3} \tag{1.9}$$

where we have introduced the density ρ and pressure p which characterise the perfect fluid. Here, expansion is explicitly linked to curvature and matter content and the evolution of the Universe is seen to be intrinsically related to the constants describing it. Observation of the expansion of the Universe can therefore be linked to fundamental properties.

1.2.2 Energy contents of the Universe

The expansion of the Universe depends upon the equation of state of the material present in the Universe, relating the density ρ with the pressure p. In a cosmological context, there are three important classes of material - non-relativistic matter (ρ_m), relativistic radiation (ρ_r) and vacuum energy (ρ_Λ). Each of these components play an important role at different points in the evolution of the Universe. Following the approach of Moore (2012), the behaviour of each of these components as a function of expansion can be found using the equation of state and the following relationship:

$$\frac{\mathrm{d}}{\mathrm{d}t}(\rho a^3) = -p\frac{\mathrm{d}}{\mathrm{d}t}(a^3) \tag{1.10}$$

Matter

Non-relativistic matter includes material such as stars and galaxies, as the velocities present are significantly below the speed of light, and also impor-

tantly dark matter. Such low velocity components mean that the pressure exerted can be treated as negligible and we can consider only the evolution of the density of particles. The evolution of the density of this component can be shown to be

$$\frac{\mathrm{d}}{\mathrm{d}t}(\rho_m a^3) = 0 \tag{1.11}$$

and the matter density decreases with the increasing volume due to the expansion of the Universe.

Radiation

Highly relativistic particles have a different behaviour, as these move with a sufficient velocity to exert a pressure. As such, the equation of state of this content of the Universe is $p_r = \frac{1}{3}\rho_r$ and corresponding relationship to expansion goes as

$$\rho_r = \rho_{r0} a^{-4} \tag{1.12}$$

which has the interesting consequence that the expansion of the Universe causes a reduction in the temperature of the photons, as energy density is proportional to T^4. This manifests as the redshifting of the frequency of light discussed in 1.4.3.

Vacuum energy

The final contribution to the energy in the Universe that we will consider is that of the vacuum energy, which enters via the stress-energy side of the Einstein equation. The important property of this form of energy is that it has an energy density that is constant with expansion. To derive the dynamics that this energy density produces, equation 1.9 can be considered in the Λ dominated case to give

$$\left(\frac{\dot{a}}{a}\right)^2 = \frac{\Lambda}{3} \tag{1.13}$$

and it can be seen that $\dot{a}/a$ is a constant. This can be satisfied if the scale factor takes an exponential form $e^{\sqrt{\Lambda/3}t}$. Therefore, observing an expansion

rate of the Universe that is accelerating will be a clear indicator of the existence of an energy component with a similar behaviour to a cosmological constant.

The fact that each of these components depends differently upon the expansion of the Universe means that each could come to dominate at different times. An early radiation dominated phase would decay more rapidly than the energy density of the matter content, until the Universe entered a matter dominated phase. Subsequently, this matter density content would decrease with the expansion until it fell below the energy density contributed by the vacuum energy, and the Universe enters a final phase dominated by the cosmological constant. These relationships will be important for interpreting observations of the Universe discussed later in the chapter, and the relevant energy contents of the components will be a key observable.

1.3 Growth of structure

The Universe that we see today has a significant amount of structure present in it, from massive over-densities in the form of galaxy clusters, and large areas of under-density caused by cosmic voids. These changes in the density of matter in the Universe can be characterised as fluctuations around a typical mean density, where we can define over- and under-densities according to

$$\delta(\vec{x}, a) = \frac{\rho(\vec{x}, a) - \bar{\rho}(a)}{\bar{\rho}(a)} \tag{1.14}$$

with $\bar{\rho}(a)$ denoting the mean cosmic density at a given point in the expansion history. Understanding the origins and growth of these structures is vital to have a full understanding of the evolution of the Universe.

The standard explanation for the growth of structure begins with small density fluctuations originating in the early Universe (Peacock, 1998; Dodelson, 2003). Quantum fluctuations in the early Universe create areas of under and over density, maintaining an average density of zero, whilst the exponential expansion results in regions of the Universe becoming causally

disconnected. This expansion causes the scale of these perturbations to become larger than the causally connected region at the time, producing large scale modes that become constant (Dodelson, 2003) and persist until later times. Peacock (1998) highlights the similarity with Hawking radiation from black holes, where quantum fluctuations at the edge of a black hole result in an emitted radiation from the body. After the exponential expansion, these modes re-enter the horizon as causally connected regions grow and provide the seeds required for the growth of structure.

1.3.1 Radiation dominated phase

Following inflation, the Universe is in a state where it is dominated by the radiation energy content of the Universe. At this time, baryons and photons are coupled such that they form a plasma and atoms do not form. The expansion of this plasma prevents the baryons collapsing to form structure at this point, and expansion is driven according to a fluid with the equation of state of radiation. Eventually, as energy density decays more quickly for radiation than for matter during expansion, the Universe will reach a phase of matter-radiation equality, when the expansion factor is a_{eq} . In the Einstein-de Sitter limit, the growth of these perturbations grow in these two regimes according to

$$\delta(a) \propto \begin{cases} a^2 & \text{before } a_{eq} \\ a & \text{after } a_{eq} \end{cases} \tag{1.15}$$

This first phase of radiation dominated expansion has some important effects for the growth of structure in the Universe. Whilst the exponential growth of inflation has finished, the Universe is still expanding and the causally connected regions are growing. The size of this causally connected region is called the horizon size, and is given by $cH^{-1}(a)$, being the distance that light has had the time to travel. This horizon size corresponds to a perturbation wavelength in Fourier space, which can be said to "enter the horizon" as the Universe expands and the horizon grows. The size of the

horizon at the point of matter-radiation equality will be $cH^{-1}(a_{eq})$, and all scales smaller than this will be causally related.

As modes enter the horizon, their growth is suppressed. This is due to the rapid expansion driven by the radiation overcoming the collapse driven by the over-densities, so their amplitudes become frozen. A mode that was originally outside of the horizon would have grown according to a^2 initially, until it re-entered the horizon and its growth becomes halted. After a_{eq} when matter dominates the expansion, these modes can then continue to grow but at the slower linear rate (Bartelmann & Schneider, 2001). All modes below the scale of the horizon at the matter-radiation equality will therefore have some suppression in their power, whilst modes larger than the horizon will have grown according to a^2 for the duration of the epoch. This would be visible in the power spectrum of the density fluctuations.

Matter dominated phase

As the expansion of the Universe becomes governed by the matter content in the Universe, dark matter over-densities are forming on all scales. Baryons are still highly energetic and interact electromagnetically, so these do not initially follow the path as the dark matter. The temperature of the Universe is sufficient to keep electrons and protons from bonding into atoms, and the Universe consists of a plasma.

As the Universe cools and expands, the energy density of the radiation falls. This drop in temperature corresponds to a decreased amount of energy that the photons can transfer to the baryonic matter, until the photons become insufficiently energetic to consistently disassociate electrons and protons as they form atoms. For a hydrogen atom, the dominant form of matter produced, the energy required to break apart this bond is 13.6 eV (Peacock, 1998). As the energy of the photons follow a black body spectrum, the temperature at which the photons become free streaming is lower than this energy due to the significant number of photons in the higher energy tail of the photon energies (Serjeant, 2010). This high energy tail of the distribution

of photon energies carry enough energy to keep the plasma ionised until the photons cool to a temperature of $\approx$ 3000K, after which they decouple and atoms form at a point called recombination (Moore, 2012; Peacock, 1998). When this pressure from the photons is removed from the baryons, they are free to collapse under the influence of gravity and contribute to the growth of structure.

This formation of structure is one of the key motivations behind including dark matter as a constituent part of the Universe. Without these potentials formed by the dark matter, structure would be seeded by the baryonic fluctuations left at the end of the radiation dominated phase, which the CMB has shown to be on the order of 10^{-5}. Combined with our estimate of the current age of the Universe, these are insufficiently large to explain the size of the density contrasts that we see in the present day. For example, consider density contrasts growing linearly after recombination, where recombination occurs at a redshift of ≈ 1000, or a scale factor of $a \approx 10^{-3}$. If the seeds of structure were the fluctuations seen in the CMB, this linear growth would mean that the largest over-densities that we would observe today would be on the order of 10^{-2}, whereas galaxy clusters observed in the Universe constitute over-densities $1 \ll \delta$.

Dark matter candidates

The introduction of dark matter has led to the suggestion of many candidates to fulfil its role. These are often weakly interacting massive particles (WIMPs) or massive compact halo objects (MaCHOs). The former introduces candidates from particle physics which were in contact with the rest of the Universe at early times, before freezing out as the temperature dropped below the mass of the particle (Dodelson, 2003) . The latter term suggests an origin from astrophysics, such as brown dwarfs which are objects with insufficient mass to start stellar fusion (Serjeant, 2010; Peacock, 1998). These could be detected by microlensing experiments such as Alcock et al. (2000a), which found they could constitute up to 20% of the missing material.

Peacock (1998) states that "the balance of cosmological evidence favours dark matter that consists of weakly interacting relic particles", citing the necessity of a small baryon fraction at primordial nucleosynthesis, but later time observations preferring a Universe with a total matter fraction that is much larger. Many candidates for dark matter therefore come in a nonbaryonic form, potentially as massive neutrinos or as a new particle, and dark matter can come in three broadly defined formed. "Hot" dark matter decouples very early in the Universe when the particles are relativistic, and have a number density similar to photons. "Cold" dark matter particles have a thermal velocity of approximately 0 as they decouple whilst they are nonrelativistic, and "warm" dark matter particles decouple when relativistic but reach a lower temperature at present times than hot dark matter. Cold dark matter is the preferred form at present times, where hierarchical structure growth occurs through merging of smaller halos (Peacock, 1998). Hot dark matter models result in less clustering than cold dark matter models, but different models will have different scale dependence for the structure growth which provides an interesting test (Wright et al., 2019) . One particle candidate is the axion, a particle from quantum chromodynamics with an extremely low mass and very weak coupling to the electromagnetic force, or from new supersymmetric partners to the Higgs or photon (Serjeant, 2010; Dodelson, 2003). Massive neutrinos are also a candidate, which appeal as neutrino oscillation experiments have shown that they do indeed have mass (Ahmad et al., 2001), but many options currently exist.

1.3.2 Late time evolution

The model of ΛCDM allows for a component other than light and matter, in the form of a cosmological constant. At later times in the evolution of the Universe, this cosmological constant can come to dominate the growth of the Universe, and this is what we believe we are seeing at the current time. This dark energy component is the largest fraction of the Universe by energy density, as we only observe enough matter to give $\Omega_M \approx 0.3$, yet observe a

Universe with a total $\Omega \approx 1$ (Planck Collaboration et al., 2018). This dark energy component has a negative pressure, and the ratio of pressure/density is denoted as w, which is exactly -1 for a cosmological constant and is required to be $< 1/3$ to provide acceleration (Dodelson, 2003).

Particle physics predicts the presence of a vacuum energy, but this is many orders of magnitude away from the finely tuned scale at which it is seen to act on cosmological scales today (Koyama, 2016). The presence of the accelerating Universe has prompted further consideration about the validity of our theory of gravity, which much work proposing that this observation indicates the need to change our theory, leading to a growth in the field of modified gravity. The simplest models, of scalar-tensor theories, introduce new fields to the dynamics of the Universe which cause late time acceleration. The field will couple to matter, introducing a "fifth force" which requires screening for consistency with tests of gravity at small scales, but is free to act at large scales (Wright et al., 2019; Koyama, 2016). Many alternative models exist that produce an accelerating Universe, such as allowing the value of w to vary with the scale factor or including a massive gravity particle (De Rham et al., 2011; Kenna-Allison et al., 2019), or even invoking braneworld models with a Universe with extra dimensions(Koyama, 2008). Many modified gravity theories struggle from the introduction of "ghosts", which are instabilities in the equations of motion due to higher order derivatives in the theories and models can require extensive work to remove these, such as the Horndeski class of models (Horndeski, 1974; Hull et al., 2016). Zhao et al. (2017) found that current disagreements between late and early time observations of the Universe mean that there is a preference for a dynamical dark energy model that allows w to vary. Some models even include interactions between dark energy and dark matter (Linton et al., 2018), and it is a particularly exciting aspect of modern cosmology that we know so little about so much of the Universe.

1.3.3 Non-linear growth

As the growth of structure becomes dominated more by local potentials than large scale expansion of the Universe, it becomes necessary to go from linear to non-linear modelling. In the non-linear regime, structure growth becomes governed by a complex combination of galaxy evolution and and the underlying dark matter halos (Howlett et al., 2015), so deriving predictions for the late time structure of the Universe typically requires solving numerically or with simulations. These simulations can take the form of N-body codes, which seed particles at very early times and follow the motion until late times, allowing resolution of clustering down to very small scales. These usually require extensive computational effort and comprehensive knowledge of a wide range of astrophysical and cosmological physics. Examples of prominent simulation approaches include the N-body code `Gadget` (Springel, 2005a) and the hydrodynamical EAGLE simulations (Schaye et al., 2015), and many such codes are an integral part of modern cosmological surveys. In Chapter 4, I will demonstrate the use of one such simulation package `L-PICOLA` in forecasting observed maps of the Universe at late times.

Galaxy bias

An interesting aspect of this model of structure growth is the concept of galaxy bias. As dark matter haloes form first in this model, and baryons later fall into the potential caused by the dark matter to form galaxies, it is the baryons that trace the dark matter web. However, they are not perfect tracers of the underlying dark matter structure, and the exact mechanics that decide where galaxies form is complicated. This means that observing galaxy positions is not necessarily the same as observing the distribution of all of the matter in the Universe, and the level to which galaxies trace the true matter distribution is described by galaxy bias, $b = \delta_g/\delta$. We will discuss in Section 2 that gravitational lensing has the key advantage that it can circumvent this issue by being able to measure the distribution of all forms of gravitating matter.

1.4 Observable effects

Having described the evolution of the Universe leading to the vast cosmic web structure that we observe today, I will move onto considering the Universe that we observe today. It has been shown how fundamental quantities such as the amount of matter in the Universe have strong effects upon the resulting evolution, and we will now turn to the observations that can shed light on these parameters.

1.4.1 Hubble parameter

The Hubble parameter H is a significant parameter that arises from the Friedmann equation shown earlier (1.8). The Hubble parameter is defined as

$$H = \frac{\dot{a}}{a} \tag{1.16}$$

and its value at the present day is known as the Hubble constant, H_0, although the function itself varies through cosmic time. Defined as ratio of the velocity of the expansion and the size of the expansion, the parameter gives a direct relationship between the rate of expansion and the distance. This leads to it being displayed graphically with distance on the x axis and velocity on the y axis, such as in Figure 1.1.

The units of the Hubble parameter, being velocity divided by distance, are inverse time, although it is typically expressed in km s^{-1} Mpc^{-1}. Expressing it in this form more explicitly highlights how the velocity is changing as a function of distance. The Hubble time, $1/H_0$, gives an estimate for the age of the Universe.

The value of the H_0 is one of the current controversies in observational cosmology. First measured by Lemaître (Lemaître, 1927), who assumed all galaxies share a common luminosity and extracted a value of 625 km/s/Mpc, and shortly after by Hubble (Hubble, 1929) (shown in Figure 1.1), the measured value has significantly lowered as observations have improved.

Today, the controversy is due to the disagreement in the value for H_0 that is suggested by near Universe probes compared to those based upon

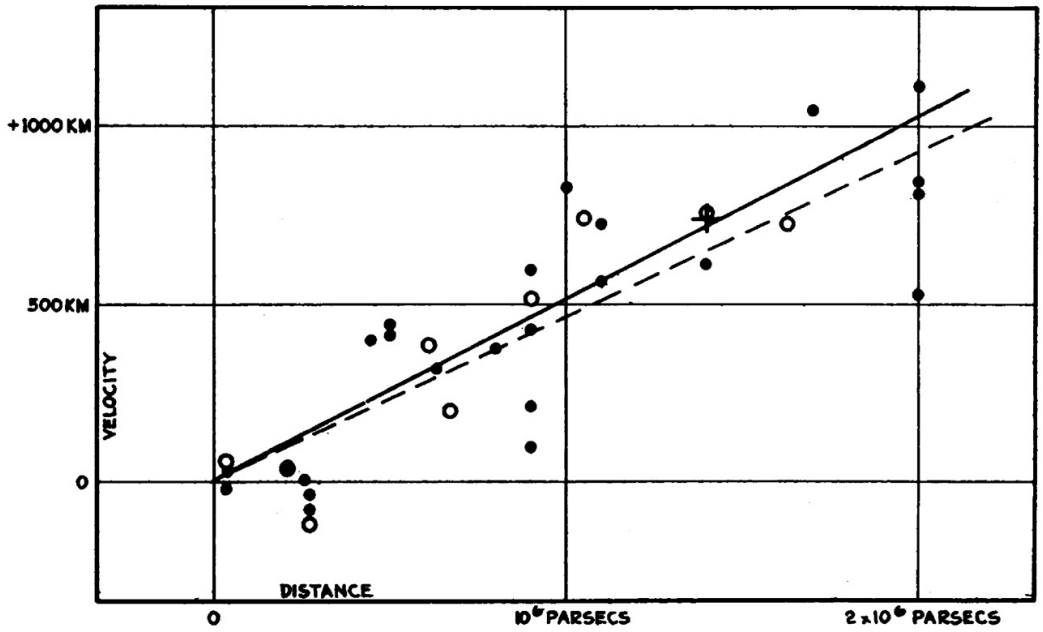

Figure 1.1: The measurement of recession velocities as a function of distance from Earth, from Hubble (1929).

measurements of the early Universe. It was initially expected that CMB experiments would support and refine the value for the acceleration found by supernovae, with Martin Rees stating in 1999 that "we will not only agree that the value of H is known to 10 percent - we'll agree what that value is" (Crittenden & Turok, 2001). This has not been the case as subsequent early and late time probes of the Universe have found an increasing disagreement between the two methods of measurement.

The CMB experiment Planck infers a value of 67.4 ± 0.5 km/s/Mpc (Planck Collaboration et al., 2018), by extrapolating its best fit cosmological parameters in a ΛCDM cosmology through to modern day. Conversely, the first measurement of an expanding Universe was made using supernovae and these infer a higher value, which are discussed further in Section 1.5.4. This disagreement is an ongoing question in cosmology, with pressing importance due the relationship between the Hubble parameter and the equations describing the expansion of the Universe. Accurate measurement of H_0 is

important for our understanding of the Universe.

The clustering amplitude σ_8

Another observation parameter that is prevalent in modern cosmology is σ_8, which describes the amount of clustering present in the Universe at a scale of 8 Mpc. This measurement is important for calibration of the linear power spectrum, which dictates the amount of clustering present at earlier times in the evolution of the Universe. The amount of structure present in the Universe is dependent upon the law of gravitation and the parameters describing the Universe. As many surveys use the power spectrum as a primary observable, σ_8 is a key consideration for cosmological constraints.

1.4.2 Measuring distance

Distance is a difficult thing to measure. Our earlier discussion considering the metric has shown how there can be a variety of ways of defining distance, which depend on the geometry of the coordinate system. The curvature introduced by the presence of matter and the fact that there is expansion of the Universe means that the background against which we attempt to define these distances is complicated. Due to this, there are several ways of defining distance in the Universe, all of which are important for building a coherent view of the Universe.

Proper distance

Proper distance refers to the distance inferred considering the time taken for a photon to travel along the path. By defining distance as a relationship between speed (c) and time, it is perhaps the distance measurement most familiar to us. A proper distance can therefore be defined as

$$\mathrm{d}D_{pr} = -c\mathrm{d}t = -c\mathrm{d}a\frac{1}{\dot{a}H} \tag{1.17}$$

integrating this quantity between two points in the expansion history of the Universe will give the proper distance. This function has an explicit

dependence upon the expansion factor at the two times it is evaluated.

Comoving distance

A related but alternative distance measure is that of comoving distance. This is a distance measure which considers the bulk expansion of the Universe and removes the dependence upon the expansion factor from the distance measure. This means that these distances will remain constant through the expansion history of the Universe, but may change due to local motion. The comoving distance can be found (Bartelmann & Schneider, 2001) by

$$D_{com} = \frac{-c}{a}\mathrm{d}t = -c\mathrm{d}a\frac{1}{\dot{a}a} \tag{1.18}$$

which can also be written as

$$D_{com}(z_1, z_2) = \frac{c}{H_0}\int_{a(z_2)}^{a(z_1)} [a\Omega_m + a^2(1-\Omega_m-\Omega_\Lambda) + a^4\Omega_\Lambda]^{-\frac{1}{2}}\mathrm{d}a. \tag{1.19}$$

Luminosity distance

The luminosity of an object can be considered as a fixed number of photons being emitted per unit time, and spreading outwards from the source spherically. Photons will be spread equally across the surface of this sphere, such that the total number of photons observed at any distance should be constant, i.e

$$L \equiv 4\pi r^2 f \tag{1.20}$$

where f is the flux per unit area at distance r from the source. This relationship can be reversed if the brightness of a source is known exactly, so that a luminosity distance can be found from the ratio of the observed and known brightness.

Whilst this arrangement may be true in the lab, when extrapolated to the scales considered in cosmology the expansion of the Universe needs to be accounted for. Bartelmann & Schneider (2001) states that as the Universe expands, photons becomes redshifted the distance between successive photons also increases, and the total area of the sphere over which the photons

are distribute also grows, meaning that the corrected luminosity distance is given as

$$D_{lum} = \frac{a(z_1)^2}{a(z_2)} f_K \left[D_{com}(z_1, z_2) \right] \tag{1.21}$$

Angular diameter distance

A final distance measure that we shall consider is that derived from looking at the apparent size of objects. In much the same way that luminosity distance compares the apparent and absolute brightness of an object to infer a distance, angular diameter distance uses the apparent and absolute size of an object to calculate a distance.

Using Euclidean geometry, an object perpendicular to an observer at distance R with length l will occupy an angular diameter defined by

$$\sin\theta = \frac{l}{R} \tag{1.22}$$

In astronomy, almost all angles are very small, meaning that we can use the approximation $\sin\theta \approx \theta$. Considering that the comoving size of an object is given as l/a, the angle subtended will be $l/(aD_{com})$ and comoving distance therefore relates to comoving distance, under the assumption of flat geometry according to

$$D_{ang} = aD_{com}. \tag{1.23}$$

1.4.3 Redshift

Allowing expansion in the metric of the Universe has further effects for observing the light emitted by luminous sources, as the propagation of photons is now affected by the space it travels through. The relative motion of an observer to the emitter will manifest as an alteration to the observed frequency of light. Sources moving towards an observer appear shifted towards the bluer end of the spectrum, and those moving away appear redshifted. As

the Universe is expanding, distant objects appear redshifted to an observer on Earth.

Redshift can be considered as a change in the time period observed between successive peaks in the intensity of light (corresponding to the frequency of the photon). This effect can be quantified by reconsidering the metric defined in equation 1.3 and remembering that a photon has a space-time interval of 0 at all times, implying

$$|c\mathrm{d}t| = a\mathrm{d}w \tag{1.24}$$

for a spatial interval of $\mathrm{d}w$. Following Bartelmann & Schneider (2001), as comoving distance is constant by definition, we can use this distance between observer and emitter and find similarly conserved quantities

$$w_{eo} = \int_o^e \mathrm{d}w = \int_{t(o)}^{t(e)} \frac{c}{a}\mathrm{d}t \tag{1.25}$$

It then follows that for the observer ($\mathrm{d}t_o$) and the emitter ($\mathrm{d}t_e$), this can be related to the frequency and wavelength observed in these two frames according to ;

$$\frac{\mathrm{d}t_o}{\mathrm{d}t_e} = \frac{\lambda_o}{\lambda_e} = \frac{v_e}{v_o} \tag{1.26}$$

Defining redshift (z) as a proportional change in wavelength leads to the observed redshifting effect being directly relatable to a measurement of the size of the Universe at the time of emission and observation, in the form of the scale factor $a(t)$.

$$1 + z = \frac{a(t_o)}{a(t_e)}. \tag{1.27}$$

1.4.4 Cosmological statistics

Observational cosmology requires the use of statistics that can summarise our data, as the density field that we observe is just one outcome from an ensemble of possibilities. We extract summary statistics so that we can compare

the observed, real Universe results with theorised results from either calculations or simulations, without needing to know the exact initial conditions of our Universe and propagating them to the modern day.

Surveys observe a field across the sky, be they fluctuations in the CMB or over-densities in galaxy counts, and the probability distribution functions of these fields carry information regarding the underlying cosmology of the Universe. Through utilising the right statistics to describe these fields, we can maximise the information gained from cosmological surveys.

Gaussian random fields

If all moments of the distribution were known, then any PDF could be reconstructed perfectly. In the case of Gaussian fields, only information up to the second moment, the variance, is required, and all odd number moments vanish (Isserlis, 1918). Many fields in cosmology are Gaussian random fields, as it is believed that the initial fluctuations seeding structure were Gaussian. Later time effects, such as gravitational structure formation, will introduce non-Gaussian elements into this distribution, although some models also introduce this earlier in the Universe's evolution. The degree with which the field can be described by Gaussian statistics is therefore an incredibly useful tool and will become increasingly more useful in future surveys, and new techniques to access information outside of Gaussian approximations will be required.

Two-point correlation function

The two-point correlation function is a powerful tool in cosmology, describing the strength of the correlation between the values of a field at different distances apart. It is also possible to cross correlate between different fields, but we shall usually consider the correlation of a field with itself, or auto-correlation, in this thesis. For a field $\phi(\mathbf{x})$, the correlation function $\xi(\mathbf{r})$ is defined

$$\xi(r) \equiv \langle \phi(\mathbf{x})\phi(\mathbf{x}+\mathbf{r}) \rangle \tag{1.28}$$

where isotropy and homogeneity imply that the correlation function is not sensitive to the direction of the distance between two points.

Power spectrum

The power spectrum is closely related to the two point correlation function, as it is the Fourier transform of it;

$$P_{\phi\phi}(\mathbf{k}) \equiv (2\pi)^{\frac{3}{2}} \int \mathrm{d}^3 r \xi(r) e^{-i\mathbf{k}\cdot\mathbf{r}} \tag{1.29}$$

Alternatively it can be calculated from the field represented in Fourier space according to

$$\langle \phi(\mathrm{k}) \phi * (\mathrm{k}) \rangle = \delta_D(\mathbf{k}_1 - \mathbf{k}_2) P_{\phi\phi}(\mathbf{k}_1) \tag{1.30}$$

For a Gaussian random field, knowledge of the power spectrum would be sufficient to produce realisations of the field. Power at a given mode can be interpreted as the variance of the fluctuations at the mode, and randomly sampling coefficients from this distribution would produce a Gaussian random field. The shape of the power spectrum will be influenced by the duration of the period of radiation dominance, as discussed in 1.3.1. Similarly, this analysis can be extended to spherical harmonics for analogous results.

1.5 Observational Cosmological probes

1.5.1 Cosmic Microwave Background

One of the most successful probes of cosmology in recent years has been the cosmic microwave background (CMB). Originally detected by Penzias and Wilson in 1964 (Penzias & Wilson, 1965), the CMB has become a leading probe in modern cosmology through the satellites COBE, WMAP and then through Planck (Planck Collaboration et al., 2018). All CMB probes have sought to detect the scale of fluctuations present in the radiation density.

Planck observes light at frequencies in the microwave spectrum, in order to observe temperature fluctuations around 2.7K. As described in Section

1.3.1, this light originates from the early Universe. The early Universe was hot and dense, and as it expanded it cooled. Eventually, the Universe reached a temperature where an insufficient amount of highly energetic photons existed to keep this plasma ionised, and electrons and protons recombined into atoms. The Universe became transparent to light at this time, and it is this light which we can observe in the CMB. As the Universe expanded, this light was red-shifted into the microwave regime of the electromagnetic spectrum.

Planck measures the two point correlation function between temperature fluctuations in this microwave background, known as the TT power spectrum, to constrain cosmology, as well as further polarised spectra in E and B. Comparing this correlation to computed results for different cosmological parameters gives constraints on key quantities. These template spectra can be calculated using codes such as `camb` (Lewis & Bridle, 2002a) and `CLASS` (Lesgourgues, 2011). These codes accurately model the physics at early times to forecast the power spectrum expected in different cosmological models. An example of a measured spectrum compared to a predicted one can be seen in figure 1.2, with the dots representing data points and the solid line representing the best fit model, of a ΛCDM model. The shape of the spectrum is well explained by the current understanding of the early Universe. The flat, scale invariant section of the spectrum at low ℓ are the largest modes which had not had chance to enter the horizon and were therefore unaffected by the expansion of the Universe at the time of the emission of the CMB, and their form was preserved from the primordial origins. The first peak is formed due to the size of the horizon at the time of recombination and subsequent oscillations at higher ℓ modes are due to the behaviour of the photon-baryon plasma interacting with gravitational potentials. At higher ℓ modes, the fluctuations are washed out at recombination.

1.5.2 Baryon Acoustic Oscillations

Another observational signature that originates from the early plasma state of the Universe is the Baryon Acoustic Oscillation peaks. As discussed in

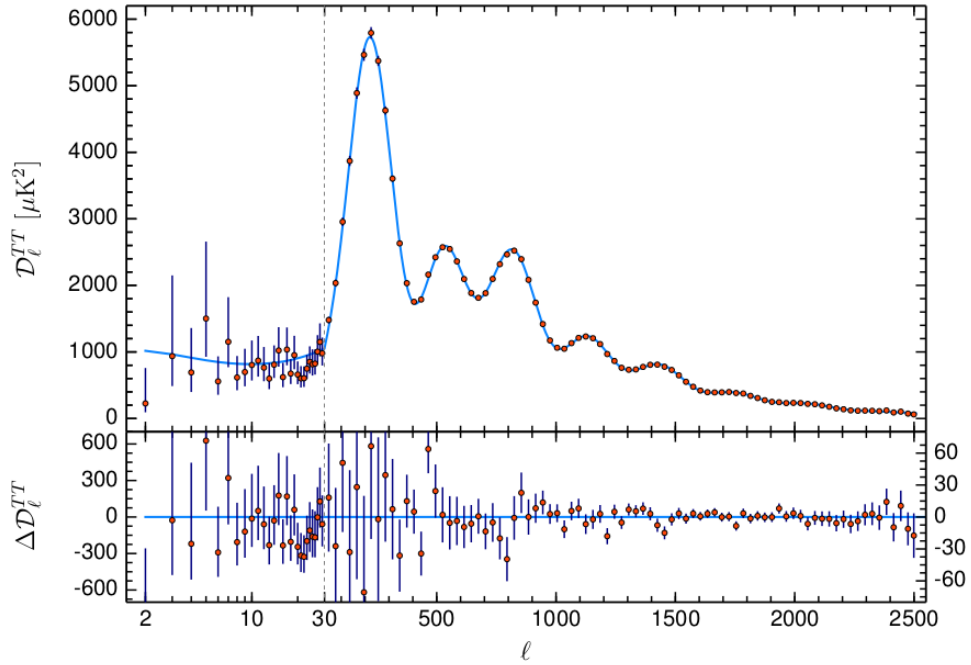

Figure 1.2: Planck Collaboration et al. (2018) power spectrum measurements using TT correlations. The best fit model is shown. The exact shape of the oscillations in the power spectrum are related to the perturbations in the early Universe plasma.

Section 1.3.1, dark matter, which does not interact electromagnetically, can form over-densities which then undergo collapse and grow to higher peaks. Baryons do interact electromagnetically, so feel a resistance to this collapse, but they also feel the potential caused by the dark matter. Waves are created in this plasma due to the interaction between the over-density of dark matter and the plasma, which oscillate outwards radially from the over-densities. This results in a scenario where a peak in dark matter density will have a spherical shell of baryon density associated with it at a characteristic distance defined by the sound horizon. As initial over-densities later go on to form the seeds for galaxies, observing the characteristic separation scale of galaxies at later redshift should give a method of detecting this characteristic scale (Carter et al., 2018).

This scale is defined by plasma physics in the early Universe, and later time evolution affects the currently observed separation. Measurement of the power spectrum of galaxies should give a characteristic "BAO peak" at the scale associated with this shell, and as such, observation of the BAO peak gives information about the later time evolution and geometry of the Universe. Later in the Universe, as structure begins to form, gravitational potentials in the large scale structure of the Universe cause galaxies to undergo local peculiar motions. These motions are separate from the bulk flow of the Universe, and when unaccounted for can alter the positions inferred for galaxies, by the effect of this motion on the redshift of the light. This is corrected for in BAO measurements through a process called "reconstruction" (Eisenstein et al., 2007), where the potential is approximated and galaxies positions are altered to correct for the expected motion inferred by the local potentials (Carter et al., 2018; Alam et al., 2017). Through removing these local motions, the galaxies should be closer to the relative positions of the initial perturbations that seeded them.

Figure 1.3 shows the BAO peak found by BOSS (Beutler et al., 2016). The characteristic oscillations in the spectrum are clearly visible, with the solid line showing the model and the dots representing the data. Reconstruction

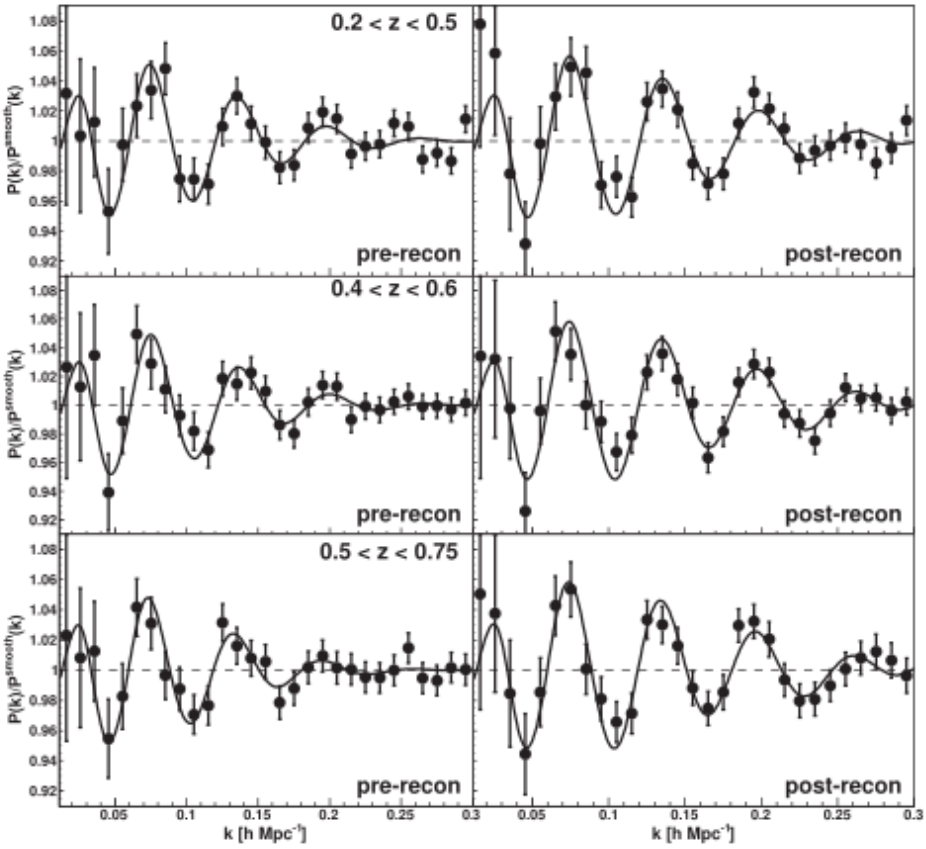

Figure 1.3: The effect of reconstruction on recovering the BAO peak, from Beutler et al. (2016). Galaxy positions are moved so that local velocities are removed from the measurement.

amplifies the signal, but the positions of galaxies can be seen to be mirroring the behaviour expected due to waves caused in the photon-baryon plasma at early times. As the BAO measures a characteristic distance scale at different points in the expansion history of the Universe, it is a strong geometrical probe and can provide tight constraints on cosmological parameters. This is shown in figure 1.4, where a combination with Planck allows for a strong degeneracy reduction.

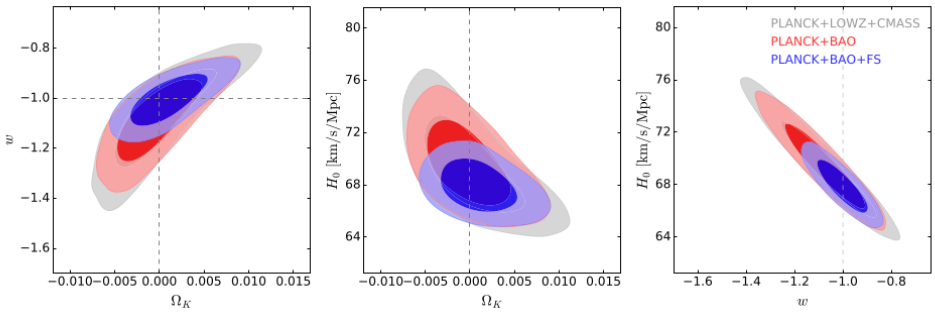

Figure 1.4: Cosmological constraints found using BAO measurements in Alam et al. (2017).

1.5.3 Redshift space distortions

As the Universe ages, structure forms and density contrasts become greater. These structures form stable, gravitationally bound systems, and galaxies will fall into larger potential wells. Each object will have a velocity component according to the potential within which it moves, and this will have a tangential and radial component relative to an observer. Velocity components in the line of sight of an observer will cause the redshift to change, and galaxies with a velocity heading away from us will result in us inferring a higher redshift for that galaxy than other members of the cluster,with lower redshifts for galaxies moving towards us, and the shape of the cluster will appear distorted in redshift space. Another component is due to the random motion of galaxies within clusters, which produces an apparent elongation when viewed in redshift space, in an effect called the fingers of god (Percival, 2013)

The motion of galaxies due to large scale gravitaitonal potentials distort the power measured in an easily modelled way by considering linear effects (Kaiser, 1987; Percival, 2013) and observations of the linear growth rate, f, give a measure of how over-densities grow with the evolution of the Universe. The linear growth rate is defined

$$f \equiv \frac{\mathrm{dln}D}{\mathrm{dln}a} \tag{1.31}$$

where D describes the scale of over densities in the Universe. It is also possible to construct correlation functions using redshift space coordinates, with the result having a dependence on the redshift distance between pairs, and such observations give direct detection of the strength of structure growth in the Universe (Hamilton, 1998).

1.5.4 Supernovae

Significant evidence for the accelerating expansion of the Universe came from studies of supernovae (Perlmutter et al., 1999; Riess et al., 1998). The Phillips relation (Phillips, 1993), relating the width of a type 1a supernova light curve to its peak magnitude, was motivated by earlier work suggesting that there was a relationship between the rate of change in B band magnitude of supernovae and the peak luminosity. (Pskovskii, 1977, 1984). Subsequent work has supported this empirical relationship, and studying the relationship in optical magnitudes has led to tighter constraints on the peak magnitudes (Riess et al., 1996; Conley et al., 2007; Guy et al., 2007). As the peak magnitudes can be tightly constrained using these relationships, it becomes possible to calculate the relative distance to these supernovae, and this is the foundation of their use for cosmology.

For cosmology, it is necessary to know the luminosity distances to these supernovae. As we only know the relative distances to supernovae from empirically observed laws about their intrinsic brightness, it is necessary to anchor the supernovae to another distance scale. Previously, this has been done through the use of the distance ladder in the nearby Universe (Serjeant, 2010). Parallax measurements of nearby stars gives a precise, nearby measurement of the distance to these stars, but this is limited to the nearby Universe, due to the diminishing size of the parallax effect with distance. To measure further distances, it is necessary to use cepheids- variable stars with a relationship between their oscillatory period and their luminosity. Cepheids are observable at distances comparable to those of observed type 1a supernovae, and as such they can be used to tune the brightness of the supernovae.

Work using cepheids have led to claims of a 3.7σ tension (Riess et al., 2018) between the expansion rate of the Universe measured with supernovae and the H_0 measurements extrapolated from Planck (Planck Collaboration et al., 2018). Other works tying the supernovae to other local Universe measures have found that the disagreement with Planck persists (Humphreys et al., 2013; Pietrzyński et al., 2013; Bonvin et al., 2016), but work tying supernovae at higher redshift using Baryon Acoustic Oscillations has found an expansion rate consistent with Planck (Macaulay et al., 2019). This is an active area of research, and could be interpreted as either a new component to the physics governing the Universe after the CMB, or that there are systematic errors in the analyses of these probes.

1.5.5 Weak lensing

As a probe of the matter distribution, independent of any other properties than the gravitational potential, weak lensing provides a powerful tool to observe the distribution of dark matter. This has been used most famously with the Bullet cluster (1E 0657-558) where the map of baryonic matter, traced by X-ray emissions, and the map of the matter inferred by gravitational potentials has been observed to be starkly different. The Bullet cluster is an example of two clusters colliding (Clowe et al., 2004). Galaxy clusters are areas of high over-density in the Universe, so have deep potential wells relative to their environment. This results in a lot of highly energetic baryonic particles at the bottom of this well, which emit light in the x-ray regime. When these two clusters passed through each other, the x-ray emitting baryonic particles interacted with each other, causing a shock, and the disrupted shape can be seen. When the mass is mapped using lensing, shown in blue in the figure, it is seen to be ahead of the baryonic matter. The two clusters are travelling horizontally on the figure, and the hot baryonic matter shown in pink has undergone significant interactions with the material from the opposing cluster during the collision, causing it to slow down and experience a drag. In contrast, the dark matter only feels the gravitational pull and not

Figure 1.5: Observations of the Bullet cluster (NASA/Chandra, 2006), with X-ray light plotted in pink and the inferred mass distribution from lensing is plotted in blue.

this extra drag so travels more freely. Observations like this indicate that a significant proportion of the matter in these clusters is not visible through electromagnetic radiation and interacts with both itself and baryonic matter with a significantly lower cross section than the x-ray emitting baryons. This is taken as strong evidence for a dark matter component in the Universe.

Weak gravitational lensing, the cosmological probe which this thesis focuses on, will be more thoroughly discussed in the following chapter.

Chapter 2

Weak gravitational lensing

One hundred years ago, gravitational lensing was being discussed as an interesting but undetectable effect of general relativity. Today, gravitational lensing has not only been detected but is now one of the leading probes for understanding the fundamental properties of the Universe. The main strength of lensing lies in the fact that it is agnostic as to whether the gravitational potential is caused by dark or luminous matter, meaning it is a probe of the overall matter density in the Universe.

This contribution to cosmology has come from lensing effects across a range of scales. The most extreme lensing effects caused by strong gravitational lensing give rise to the spectacular arcing shapes seen around galaxy clusters, and accurate modelling of these systems has led to the strength of the lensing effect being used to infer the density profile of clusters. In its most famous example in the Bullet cluster, strong lensing has explicitly shown the difference between luminous and dark matter and contributing to one of the most intriguing debates left in cosmology. The Bullet cluster consists of two clusters that have recently collided, resulting in the constituent matter being significantly disturbed. When the mass distribution is inferred by gravitational lensing, the majority of the material appears to be in a significantly different location to that visible through electromagnetic radiation. At the other end of the scale, microlensing has contributed to the same discussion

regarding the matter content of the Universe by providing constraints on the amount of black holes present in our galaxy (Alcock et al., 2000b; Niikura et al., 2019). By detecting short peaks in brightness caused by a black hole passing between us and a source, it is possible to estimate the number of black holes above a certain mass and extrapolate to provide estimates for the fraction of the total mass they contribute. Lensing has therefore given us a powerful tool to test the matter distribution across a range of scales.

A final lensing regime that we shall consider is that of weak gravitational lensing, the main focus of this thesis. This is a regime where gravitational potentials induce minor changes, of the order of 1%, in the observed ellipticity of galaxies. Although the distortions caused are of such small scale, weak lensing gains its potency for cosmology due to the fact that it is by far the most prevalent form of lensing, meaning that there is significant information present if we can extract it. As most galaxies at a distant redshift will have undergone some amount of small lensing effect, we show how it is possible to use the large numbers of galaxies observed by current surveys to statistically extract the lensing signals and measure the density of the Universe across significant fractions of he Universe.

This work will focus on using weak gravitational lensing to map the Universe. This section will first introduce gravitational lensing mathematically, and then consider several difficulties inherent in measuring it observationally. Despite these difficulties, weak lensing is one of the main analyses performed by the current generation of cosmological surveys and there are now many constraints provided by such surveys, and these will also be reviewed. Finally, we will introduce and discuss the production of maps of the matter distribution that can be made using the measurement of weak lensing.

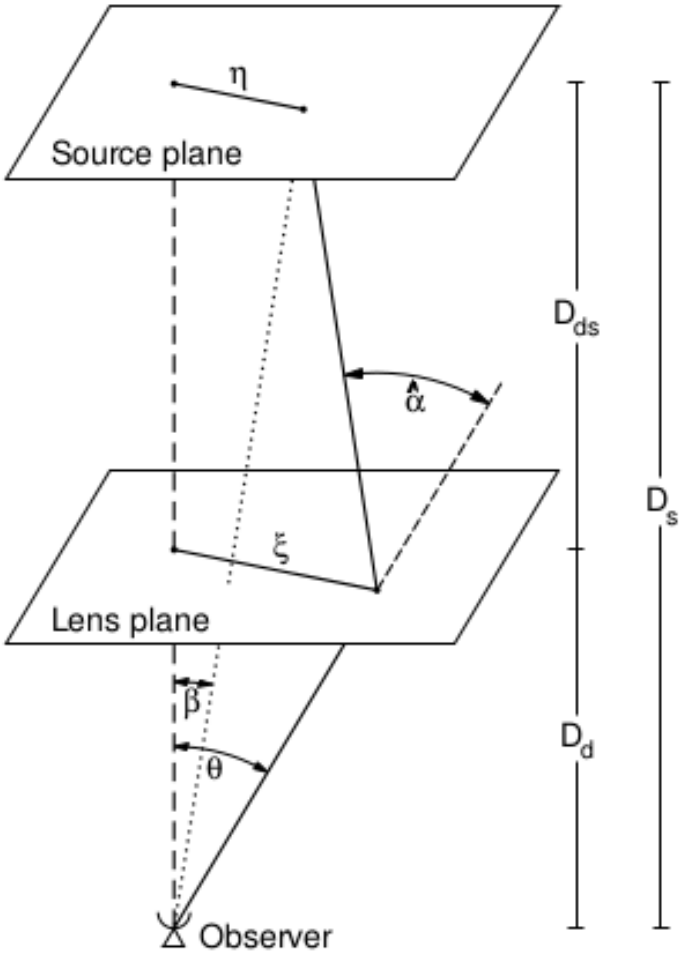

Figure 2.1: An illustration of a simple lensing configuration, from Bartelmann & Schneider (2001).

2.1 The theory of gravitational lensing

2.1.1 A typical lensing configuration

A typical scenario for cosmological lensing can be imagined as an arrangement of an observer, a massive lens object, and a more distant source object. This source object is luminous, such that its light can be observed, and photons emitted from it will pass the lens on their way to the observer. This arrangement is illustrated in Figure 2.1, with deflection angles also illustrated. In the following section, we will discuss the derivation of the magnitude of this deflection as a function of the parameters describing the relative positions of the objects, and the masses involved.

2.1.2 Deflection

General relativity gives a relation for the strength of the lensing effect relative to the mass of the lens object and the geometry of the lensing system. This is called the deflection angle $\hat{\alpha}$ and Bartelmann & Schneider (2001) show that it can be determined for a point source as -

$$\hat{\alpha} = \frac{4GM}{c^2\xi} \tag{2.1}$$

where ξ is the impact parameter, describing the minimum distance between the path of the photon and the lensing object. This condition holds providing that this impact parameter is significantly larger than the Schwarzschild radius of the lens, which is well satisfied for many of the lensing configurations that we will consider in cosmology. This can be generalised to an extended mass lens with a density as a function of radius to give the result

$$\vec{\alpha}(\vec{\xi}) = \frac{4G}{c^2}\int \mathrm{d}^2\xi'\Sigma(\vec{\xi'})\frac{\xi - \xi'}{|\xi - \xi'|^2} \tag{2.2}$$

where Σ is defined as an integrated mass profile, called the surface mass density. This is an important quantity in lensing cosmology, moving the consideration from a hypothetical mass at a point to the more physically realistic integrated potential felt by a photon along the entirety of its path.

2.1.3 Lens equation

Using Figure 2.1, we can construct an equation relating the apparent and true positions of an object that has been gravitationally lensed. Defining $\vec{\eta}$ as the location of the source on the source plane,

$$\vec{\eta} = \frac{D_s}{D_d}\vec{\xi} - D_{ds}\hat{\vec{\alpha}}(\vec{\xi}) \tag{2.3}$$

where D_s is the distance from the observer to the photon source, D_d is the distance from the observer to the massive lens and D_ds is the distance between the lens and the source, and these distances are labelled in Figure 2.1. Due to the small angles involved in the system, we can define $\vec{\eta} = D_s\vec{\beta}$ and $\vec{\xi} = D_d\vec{\theta}$ such that

$$\vec{\beta} = \vec{\theta} - \vec{\alpha}(\vec{\theta}) \tag{2.4}$$

An object at a position in the source plane of β will appear at position θ to an observer, moved due to a scaled deflection angle of $\vec{\alpha}(\vec{\theta})$. It is possible that there exist multiple β values that are solutions for the source image, which would result in multiple images appearing for a single source - the strong lensing case. This is given when the surface mass density reaches a critical value:

$$\Sigma_{cr} = \frac{c^2}{4\pi G}\frac{D_s}{D_d D_{ds}} \tag{2.5}$$

with

$$\kappa = \frac{\Sigma(D_d\vec{\theta})}{\Sigma_{cr}} \tag{2.6}$$

being the dimensionless surface mass density. We will not consider the case where multiple images are formed, and only consider the scenario when the lensing effect is weak. The surface mass density can be related to the lensing angle in equation (Bartelmann & Schneider, 2001) 2.4 :

$$\vec{\alpha}(\vec{\theta}) = \frac{1}{\pi}\int_{\mathbb{R}^2} \mathrm{d}^2\theta' \kappa(\vec{\theta'})\frac{\vec{\theta} - \vec{\theta'}}{|\vec{\theta} - \vec{\theta'}|^2} \tag{2.7}$$

The form of this equation means that α can be equated to the derivative of some field ψ, which we call the deflection potential.

$$\vec{\alpha} = \nabla\psi \tag{2.8}$$

$$\psi(\vec{\theta}) = \frac{1}{\pi}\int_{\mathbb{R}^2} \mathrm{d}^2\theta' \kappa(\vec{\theta'})\ln(|\vec{\theta} - \vec{\theta'}|) \tag{2.9}$$

The deflection potential is analogous to the Newtonian potential, but is a two dimensional quantity instead of 3 dimensional. This potential can be related to a mass distribution through the Poisson equation, $\nabla^2\psi(\vec{\theta}) = 2\kappa(\vec{\theta})$. We now have a relationship between the mass of an object, and the effect that it has on light that travels past it at a given distance, which is a powerful result. The projected density of the object is the only relevant parameter for this effect, and whether the material is dark or luminous matter is unimportant. The lens will cause lensing only dependent upon its total mass, and it is this property that will make gravitational lensing a powerful probe of the matter in the Universe.

2.1.4 Image distortion

We have described the deviations in the light path induced by a potential, and found it to be dependent upon the gradient of the potential at the point of closest approach. For extended objects, where photons are emitted from multiple points and each photon path is slightly different, this will result in different lensing angles for different photons, dependent on where in the source object they were emitted from and the exact path travelled. Lensing therefore introduces distortions in the shape of objects, and we will quantify this here.

If the angular size of the source is much less than that at which the lensing potential changes significantly, the rate of change of the distortions can be approximated as linear. This means it can be described using a Jacobian, considering how true position β varies with respect to the apparent position

θ, which is defined by Bartelmann & Schneider (2001) as

$$\mathcal{A} = \frac{\partial \vec{\beta}}{\partial \vec{\theta}} = \left(\delta_{ij} - \frac{\partial^2 \psi(\vec{\theta})}{\partial \theta_i \partial \theta_j} \right) = \begin{pmatrix} 1 - \kappa - \gamma_1 & -\gamma_2 \\ -\gamma_2 & 1 - \kappa + \gamma_1 \end{pmatrix} \tag{2.10}$$

This equation introduces the shear parameter $\gamma \equiv \gamma_1 + i\gamma_2$,

$$\gamma_1 = \frac{1}{2} \left(\psi_{,11} + \psi_{,22} \right), \quad \gamma_2 = \psi_{,12} \tag{2.11}$$

where a comma in the subscript denotes partial derivatives in the indicated coordinate direction. The two components γ and κ have different effects upon the shape of the observed image, with κ causing a magnification to either dilate or contract the size of the image, and γ introducing shape changes through an additional ellipticity. In weak lensing studies, γ and κ are small so the linear approximation is valid.

Consider the effect of lensing upon the brightness of the object. The fact that no absorption or emission of photons occurs means that the total number of photons must remain the same, i.e we can relate the source and image surface brightnesses through the knowledge of only the displacement of the photon paths. (Bartelmann & Schneider, 2001) define this relationship as

$$I(\vec{\theta}) = I^{(s)} \vec{\beta}(\vec{\theta}) \tag{2.12}$$

Using equation 2.10 we can rewrite this expression to relate the brightness at a position $\vec{\theta_0}$ in the image plane to a position $\vec{\beta_0} = \vec{\beta}(\vec{\theta_0})$ on the source plane.

$$I(\vec{\theta}) = I^{(s)} \left(\beta_0 + \mathcal{A}(\vec{\theta_0}) \cdot (\vec{\theta} - \vec{\theta_0}) \right) \tag{2.13}$$

This equation explicitly shows how the presence of gravitational lensing changes the shape of objects on the image plane. The Jacobian $\mathcal{A}$ causes the brightness at a position $\vec{\theta}$ to be different to the brightness at the similar location $\vec{\beta_0}$ in the source plane. The eigenvalues of the Jacobian can be used to calculate the distortion of the shape of the object. The eigenvalues of the Jacobian are $1 - \kappa \pm |\gamma|$ and the two related eigenvectors describe the

changes in ellipticity along two axes. The scale of the object is changed in these two directions, meaning that a circular object will appear elliptical in the presence of gravitational lensing. The determinant of the Jacobian gives the magnifying effect (μ) of the lensing - the ratio of the sizes of the image in the source and image planes, such that (Bartelmann & Schneider, 2001)

$$\mu = \frac{1}{\det \mathcal{A}} = \frac{1}{(1-\kappa)^2 - |\gamma|^2} \tag{2.14}$$

We have now introduced two significant effects of gravitational lensing; lensing causes changes in both the shape and size of an object for an observer. The next challenge is to detect this distortion in observed data.

2.2 Observational weak lensing

Cosmic shear provides an opportunity to measure gravitational potentials across a range of cosmological scales, and through the evolution of the Universe. Over the past few decades, the field has rapidly evolved from the first detections of large scale coherent weak gravitational lensing, known as cosmic shear, through to becoming a probe at the heart of upcoming cosmological experiments. In these modern surveys, the lensing effect is measured by observing the shape of galaxies and correlating it across a range of angular distances. Under the assumption that the galaxy shapes share no intrinsic correlation, any correlation of shape can be assumed to be sourced by the gravitational lensing effect.

Initial detections of cosmic shear were made in the early 2000s (Bacon et al., 2000; Van Waerbeke et al., 2000; Wittman et al., 2000), and the field has grown since then into a leading method of observing the Universe. Many modern day cosmological surveys have a significant element devoted to observing weak lensing, and this is typically done through two point statistics, which were introduced in section 1.4.4. By predicting the shape of the correlation function across different scales of the sky in universes consisting of different combinations of cosmological parameters, a likelihood can

be calculated when compared to the data set and confidence regions built. Current leading examples of these include KiDS (Hildebrandt et al., 2018), CFHTLenS (Heymans et al., 2012) and HSC (Hikage et al., 2019). The Dark Energy Survey, discussed in section 3.1.1, has already produced cosmological constraints from its Year 1 data release. These contours are shown in Figure 2.2, where they are compared against the results found from another lensing experiment, KiDS and for the CMB experiment Planck. Lensing in experiments such as these provide information from the Universe at much later times than the CMB, providing a useful opportunity to compare the results from the two different approaches, and testing our understanding of the physics across cosmic time. The KiDS-450 results (Hildebrandt et al., 2017) have been the cause of some discussion recently, with some suggestion the cosmological parameters they prefer are in disagreement with those from Planck. This has led some to suggest that ΛCDM is an insufficient model to describe the Universe, and with others suggesting that the disagreement is merely due to statistical fluctuations, or observational errors in the survey (Troxel et al., 2018b). This discussion makes results from surveys such as DES more important, as the source of the disagreement can be more tightly constrained. The DES results, shown as the black contour, overlap with both the Planck and KiDS results, and with the 1σ contour having some overlap with both surveys. Later data releases will be vital for answering the question of whether ΛCDM can explain both the early and late Universe.

2.2.1 Shape measurement

Detection of the shear caused by weak gravitational lensing requires accurate shape measurements to infer the strength of the shearing effect. Whilst we do not know the original shape of a galaxy before it was lensed, using large numbers of galaxies allows us to statistically infer the presence or absence of a lensing effect. In a given angular area of sky, if we treat all galaxy shapes as uncorrelated, we can detect the presence of lensing by looking for a residual shear when the shapes of the galaxies are averaged together. If these shapes

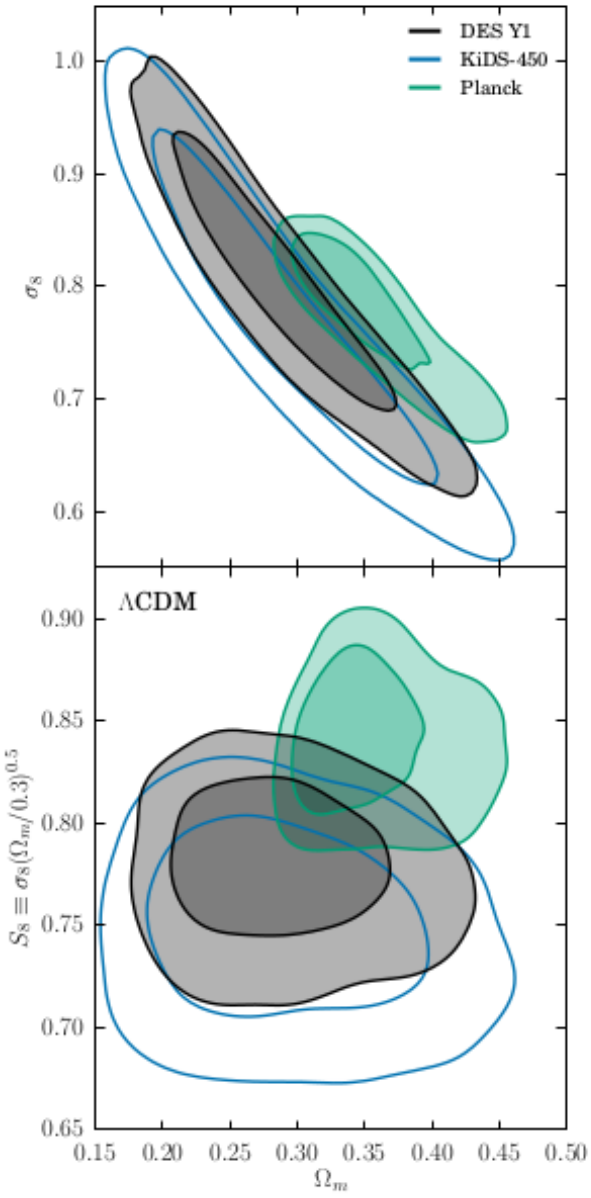

Figure 2.2: Cosmological constraints found using weak lensing data (Troxel et al., 2018a). Contour regions correspond to 68% and 95% confidence regions.

were purely uncorrelated, then this averaging would be consistent with 0, but the correlated shape distortion caused by lensing means that there will be a non-zero result. This section considers the challenges present in trying to detect and quantify the strength of gravitational lensing.

Moments

A first approach to detecting shear caused by gravitational lensing is to measure the second moment of the distribution of the light detected when observing a given galaxy, such as in Blandford et al. (1991). This moment, considering two directions in the plane, gives a measure of the spread of the galaxy. Using the surface brightness of an object $I(\vec{\theta})$ and a weight function $q_I(I)$ we can define

$$\bar{\theta} \equiv \frac{\int \mathrm{d}^2\theta q_I(I(\vec{\theta}))\vec{\theta}}{\int \mathrm{d}^2\theta q_I(I(\vec{\theta}))} \tag{2.15}$$

Following from this, a tensor of second order moments of this quantity can be built such that

$$Q_{ij} = \frac{\int \mathrm{d}^2\theta q_I(I(\vec{\theta}))(\theta_i - \bar{\theta}_i)(\theta_i - \bar{\theta}_i)}{\int \mathrm{d}^2\theta q_I(I(\vec{\theta}))} \tag{2.16}$$

where i, j are equal to 1 or 2 depending on the direction in which they correspond. The shape of the image is now defined as

$$\chi \equiv \frac{Q_{11} - Q_{22} + 2iQ_{12}}{Q_{11} + Q_{22}} \tag{2.17}$$

Under the influence of lensing, this can be shown to transform the ellipticity of a source (Schneider & Seitz, 1995) $\chi^{(s)}$according to

$$\chi^{(s)} = \frac{\chi - 2g + g^2\chi*}{1 + |g|^2 - 2\Re(g\chi*)} \tag{2.18}$$

where we have introduced reduced shear g

$$g(\vec{\theta}) \equiv \frac{\gamma(\vec{\theta})}{1 - \kappa(\vec{\theta})} \tag{2.19}$$

Equation 2.18 shows that the shape distortion relies on a combination of shear and magnification, in the form of the reduced shear component. Reduced shear is therefore an important quantity because it is the effect of lensing which it is possible to observe using shape measurement.

Model fitting

Alternatively to measuring the moments of an image, it is also possible to try and disentangle to true galaxy shape and the lensing shear. Model fitting algorithms rely on having a successful model of the true galaxy shapes and the point spread function of the observations. This model will aim to encapsulate the true shape of the galaxy through other observable properties, and will then also parameterise an additional lensing induced shear. The observed surface brightness profile of the galaxy is compared to those generated by varying the parameters in the model to find a best fit (Zuntz et al., 2013, 2018).

An example of this class of shape measurement algorithm used in the Dark Energy Survey is `im3shape` (Zuntz et al., 2013). This routine simulates galaxy images through modelling their shape as two components- the bulge following a de Vaucouleurs profile and an exponential disc. Parameters describing the exact distribution of light in the galaxy, as well as other values such as the centroid of the image and the gravitational shear, are also explored and a goodness of fit is measured in the form of a χ^2 measurement. A minimum is found through iterating through many possible combinations of parameters and these are output by the routine on a galaxy by galaxy basis. The accuracy of the method is evaluated through examining both multiplicative (m) and additive(c) biases;

$$\hat{\gamma_i} = (1 + m_i)\gamma_i^t + c_i \tag{2.20}$$

such that $\hat{\gamma}$ is the measured shear and γ^t is the true shear, in the two components. These biases can arise from a variety of sources, but the major contributors are model bias, noise bias and selection bias. Model bias, the

difference between an assumed shape and the true galaxy shape, has been shown to be a significant source of error in shear measurement (Mandelbaum et al., 2015) and is necessary to adequately control for the desired accuracy of current generation surveys. Noise bias is usually the dominant source of error (Zuntz et al., 2018) and arises from incorrectly assuming that the likelihood surface is symmetric, where using maximum likelihood estimators unavoidable introduce error (Hirata & Seljak, 2003). A selection bias can enter if objects are added to catalogue in a way that is affected by the shape of the galaxy. DES SV results found that this selection bias was more significant than expected, contributing a bias of up to 5% (Jarvis et al., 2016). Image simulations are used to calibrate the bias and form the basis of comparison between different approaches. In the DES Year 1 weak lensing catalogues (Zuntz et al., 2018), these biases were found to be sufficiently small for the level of cosmological constraints desired, with the dominant multiplicative bias being 2%. Objects are allocated estimated bias values based on observed properties of the galaxy, and the measurements are corrected to give a final shear estimate that is suitable for binning into pixel maps.

PSF

Shape measurement depends upon the accurate measurement of the distribution of light received from a distant galaxy. These galaxies are observed using telescopes on Earth, and the light from the source has to travel through several different media before it is recorded on an image. For example, the photons have to traverse the Earth's atmosphere, undergo reflection and refraction at the telescope as light is focused, and then interact with a CCD in order to record the image. Further to this, the effect of all of these processes can vary across the CCD and differ from one exposure to the next. It is conceivable that all of these processes may influence the shape of the image observed, and this requires accounting for in the observation in case it is misinterpreted as a lensing signal.

The way that this non-cosmological ellipticity contribution is accounted

for is through measurement of the point spread function (PSF). This function describes how the whole imaging arrangement responds to a point like source, and the most point-like object in astronomy is usually a star. The difficulty lies in measuring it across the whole surface, and this is typically done by observing the shape of stars at different locations in the image. Modelling the PSF across the image in this way is a suitable but not ideal solution as stars are located at discrete points in the plane, giving a sampling of the PSF across the imaging surface (Zuntz et al., 2017), but the galaxies that we intend to measure are in different positions to the stars. This means that it is necessary to interpolate the PSF between known positions such that it can be modelled at the location of the galaxies. By modelling the extended distribution of light caused by a sampling of point sources across the CCD, it is possible to build a model describing how this changes across the surface of the imaging surface such that it can be removed from shear measurements.

MetaCalibration

I will focus on explaining the `MetaCalibration` method (Huff & Mandelbaum, 2017) for galaxy shear measurement here, as it is the preferred technique used for the DES data(Zuntz et al., 2017).

`MetaCalibration` is a method for estimating the gravitational shear effect without requiring extensive knowledge of the intrinsic shape of the galaxy. Removing the requirement of knowing the true shape of a galaxy dramatically simplifies the modeling of the effect and is shown to produce measurements with significantly reduced systematics when compared to other methods.

The approach uses real images of galaxies, and applies a known shearing effect, working under the model that an observed galaxy image $I(x)$ consists of a true galaxy image $G(x)$ convolved with a point spread function $P(x)$, which describes all of the optical effects from the atmosphere through to the CCD. The response of the shape measurement algorithm is measured and compared to the exactly known applied shear, and this gives information on how the measurement algorithm responds to the application of a known shear.

This approach therefore does not require any specific shape measurement routine, as long as it behaves in a well understood way in the presence of shear, and due to the weak nature of the lensing effect, only first order derivatives of the response need to be calculated.

`MetaCalibration` produces "counterfactual images" using real data, in a process defined in (Huff & Mandelbaum, 2017) as

$$I'(\mathbf{x} \mid \mathbf{g}) = \Gamma * \left[\hat{\mathbf{s}_\mathbf{g}} \left(P^{-1} * I\right)\right]. \tag{2.21}$$

In this notation, $\hat{\mathbf{s}_\mathbf{g}}$ refers to a shear operator, $\mathbf{g}$ is the strength of the shear, Γ is another PSF function that accounts for noise introduced in the Fourier modes where P is small, and I' is the counterfactual image. This equation highlights the importance of correctly modelling the PDF for the observational apparatus, but that is vital for all weak lensing studies. This counterfactual images can be then be fed into a shape measurement pipeline such as `im3shape` (Zuntz et al., 2013) or `ngmix` (Sheldon, 2015) and resulting shear calculated, to measure the sensitivity of the pipeline to an applied shear in the presence of the PSF Γ.

Redshifts

Lensing is sensitive to the geometrical arrangement of the source, lens and observer, being sensitive to the distances between each. Additionally, on a cosmological level, the amount of structure that has formed is dependent upon the redshift at which it is observed for that cosmology. As observational weak lensing studies attempt to predict a lensing signal for a given set of cosmological parameters, it is important that this signal is calculated using distances that are representative of those in the real Universe, and similarly that uncertainties in this measurement are accounted for. These distances are measured through redshift observations, which would ideally be inferred through spectroscopic observations. Through spectroscopy, intensity can be measured for many different wavelengths and the position of distinctive features can be used to calculate redshift. Spectroscopic observations require

longer exposures than photometric observations to acquire a given signal to noise, as each spectroscopic bin receives less light than the larger photometric one, but the accuracy of the redshift measurement is much improved.

In weak lensing studies, which require the observation of a large number of galaxies to make the lensing effect detectable, it is usually too expensive to perform spectroscopic measurements, particularly for the larger field surveys. Due to this, the majority of DES and many other large survey footprints do not have spectroscopic information and redshifts are photometric, through observing the intensity of light in broad wavelength bins. Redshifts are typically related to these bin intensities through fitting a galaxy model to the profile and applying redshift corrections, but due to the range of functions which could fit the data, this can frequently lead to "catastrophic errors" where a significantly wrong redshift is assigned (Ma et al., 2006; Bernstein & Huterer, 2010).

There are frequently galaxies that are observed photometrically which also have spectroscopic information, and these can be used to quantify the errors of the photometrically inferred distribution. This relies on the spectroscopic population being representitive of the wider population of observed galaxies, which is frequently not true for the fainter end of the galaxy population (Bonnett et al., 2016). Instead, DESY1 (Hoyle et al., 2018) uses the COSMOS field (Laigle et al., 2016) which measured photometry over 30 bands, which is many more than those used typically, and is believed to be complete for the population observed in DESY1. Through this approach, the source galaxy redshifts could be validated.

The DES Y1 data catalogue estimated these redshifts by implementing a Bayesian Photometric Redshift (BPZ) algorithm, such as that used in Benítez (2000) and Coe et al. (2006). This approach uses galaxy templates from Bruzual & Charlot (2003); Kinney et al. (1996); Coleman et al. (1980) to return a likelihood distribution for the redshift of the observed galaxy. This redshift is used to identify those galaxies which can be used as sources, using the mean result. The redshifts are calculated using the `MetaCalibration`

photometry, as the `MetaCalibration` process of adding noise and shear to the images can alter the redshift probability distribution calculated for each object. Therefore, it is necessary to calculate redshifts accounting for these effects, and using the same photometry to ensure consistency with the model fitting. The full routine is described in Hoyle et al. (2018), and the use of cross correlation redshifts was tested in Gatti et al. (2017); Davis et al. (2017). Cross correlations between a photometric population and some overlapping sample of spectroscopically observed galaxies has been shown to be a powerful way of constraining the distribution of redshifts, in a way that removes the requirement that the validation galaxies need to have a similar distribution to the photometric population, once a cosmological model has been assumed (Newman, 2008). `RedMAGiC` (Rozo et al., 2016) galaxies were used as a reference sample for the redshifts, which were in turn calibrated through comparison with BOSS galaxies (Cawthon et al., 2017).

Mapping

Shear is estimated using galaxy ellipticities ϵ; by averaging over a significant number of galaxies and in the absence of intrinsic alignments, ellipticities not due to lensing should average to give a (noisy) mean ellipticity of zero; any remaining signal is due to the lensing shear γ, i.e

$$\epsilon = \gamma + \epsilon_{int} + \epsilon_s, \tag{2.22}$$

where ϵ_s is the noise associated with estimating a galaxy shape, ϵ_{int} is the intrinsic shape of the galaxy and ϵ is the observed distortion. Averaging this estimator for a large number of galaxies will reduce the noise, so it is desirable to have the densest possible background field of lensed galaxies. For producing mass maps, this is achieved by having deep redshift bins to give the necessary angular resolution. The greater the number density that a survey achieves, the more tomographic mapping bins they will be able to map. Binning galaxies in this way allows for the noise on the shear measurement to be reduced, at the expense of angular resolution being reduced to the scale

of the pixels being used.

Intrinsic alignments

Another barrier to accurate shape measurement is the assumption that the galaxy shapes are uncorrelated. In practice, this is not strictly true. The galaxies themselves feel large scale gravitational potentials, and this may cause their orientations to change. It has been shown that galaxies preferentially align themselves with the filamentary structure of the Universe (Catelan et al., 2001a; Mackey et al., 2002), and this effect can cause a biasing in the shape measurements. Samuroff et al. (2019) describes two different sources of alignment being the main concerns for modern lensing surveys; one form of alignment is caused by the physical proximity of galaxies as described above (so called II alignments), and another form of alignment introduced by the potential in which galaxies form, and the lensing distortions of that same potential on more distant galaxies (Hirata & Seljak, 2004) (GI alignments).

There are several approaches suggested for dealing with intrinsic alignments that depend upon reliable redshift information, such as discarding galaxies which are physically close to each other (Catelan et al., 2001b; Kirk et al., 2015) or down-weighting galaxy contributions to correlation functions (Heymans & Heavens, 2003; King, L. J. & Schneider, P., 2003). These do not correct for the GI alignments which can be the dominant effect in cosmic shear analyses (Samuroff et al., 2019). Samuroff et al. (2019) defines two main approaches to constraining intrinsic alignments with galaxies. The first method is called a direct constraint, where a galaxy sample is chosen at low redshift with some colour cuts to identify well measured red galaxies with spectroscopic information, to maximise the intrinsic alignment signal. The second method is known as simultaneous constraints, where the intrinsic alignment model is considered alongside the shear signal and is marginalised out in cosmological analysis. Such models typically assume that the IA power spectrum is of the same shape as the matter power spectrum, with a redshift dependent rescaling (Bridle & King, 2007). Accurate modelling of intrinsic

alignments requires extensive knowledge of galaxy evolution through cosmic time and is requires consideration of a wide range of effects, including the colour and mass of the galaxy (Joachimi et al., 2013; Hilbert et al., 2017). If uncorrected for, these intrinsic alignments could be inferred as a lensing effect, and biasing the amount of matter inferred in the Universe (Joachimi et al., 2015). As these effects are cosmological in origin, it has also been suggested that they may be used as an interesting probe (Chisari & Dvorkin, 2013; Troxel & Ishak, 2015).

As the number density of galaxies observed will increase with future surveys, modelling intrinsic alignments will become increasingly important for precision cosmology.

2.3 Mass mapping

Having introduced the relationship between a lensing potential and shape distortion, we will now consider how measurements of shear can be used to produce maps of the mass distribution. This typically takes the form of κ maps, the projected over-density field introduced in 2.1.

2.3.1 Direct inversion

The first approach we will consider is that of the Kaiser-Squires reconstruction (Kaiser & Squires, 1993), or direct inversion. As the relationship between shear and the mass distribution causing the lensing is dependent on differential equations, this approach uses Fourier space, where these derivatives become multiplications.

The approach assumes the presence of a shear field that is continuously sampled in such a way that the distortion of background galaxies is described across the whole of the footprint. This scenario is that in which there is a large number of background galaxies with which to estimate the shear, and that they are uniformly spread across the footprint. This means that there is also a uniform noise field.

The relationship between the shear estimators $e_{1,2}$ and the surface mass distribution in real space can be described as

$$e_i = -D_i \nabla^{-2} \Sigma(\theta) \tag{2.23}$$

where ∇^{-2} is the inverse of the Laplacian operator and D_i is an operator mapping between the gravitational potential and the shear. This operator can be reversed in Fourier space in a relatively simple way. Defining our Fourier transform as

$$\tilde{e_i}(\mathbf{k}) = \int \mathrm{d}^2\theta e_i(\theta) \mathrm{e}^{i\mathbf{k}\cdot\theta} \tag{2.24}$$

then using equation 2.23 leads to

$$\tilde{e_i}(\mathbf{k}) = \chi_i \tilde{\Sigma}(\mathbf{k}) \tag{2.25}$$

where our previous operator $D_i \nabla^{-2}$ has now been replaced by the new function χ ;

$$\chi = \begin{bmatrix} (k_1^2 - k_2^2)/k^2 \\ 2k_1 k_2 / k^2 \end{bmatrix} \tag{2.26}$$

which makes uses of the relation that the Fourier transform of a derivative of a function is the Fourier transform of the original function, multiplied by the $\mathbf{k}$ modes and a unit imaginary factor. This means that solving equation 2.23 is now much simpler, and the Fourier modes of the mass distribution can be simply found by transforming the shear modes and applying these multiplicative factors. The mass map can then be found by the reverse Fourier transform, to return to real space coordinates and the final mass map. The intrinsic ellipticity of the source galaxies adds a white noise component to the mass maps which are produced, which means that high frequency modes need to be filtered out before producing the final map.

Maps using observational data

The direct inversion method has been successfully used with weak lensing data to produce mass maps for a variety of surveys, and it is now a widely used technique. Using Fourier transforms means that the surface is assumed

to be flat, but many previous surveys have used a footprint that can be approximated as flat, meaning it is a valid approximation. These surveys include CFHTLens (Van Waerbeke et al., 2013), which covered 154 deg^2 over 4 distinct regions, and the COSMOS survey (Massey et al., 2007).

The Dark Energy Survey produced maps of the 139 deg^2 area of the Science Verification area (Chang et al., 2015; Vikram et al., 2015) using the Kaiser-Squires approach. This method used a Fourier transform of the complex shear field and rearranged equation 2.25 to explicitly define the transformation to a mass map as

$$\tilde{\kappa}(\mathbf{k}) = D^*_{\mathbf{k}}\tilde{\gamma}(\mathbf{k}) \tag{2.27}$$

$$D_{\mathbf{k}} = \frac{\mathbf{k}_1^2 - \mathbf{k}_2^2 + 2i\mathbf{k}_1\mathbf{k}_2}{|\mathbf{k}|^2} \tag{2.28}$$

where $\mathbf{k}$ denotes the Fourier modes of the coefficients, and the subscript (1,2) denotes the two angular directions present in the 2D map. The approach is insensitive to a constant offset, so the $\mathbf{k} = 0$ mode is set to 0. Figure 2.3 shows the DES SV mass maps produced through using this reconstruction approach. The central panel shows the real component of the result when the Fourier modes of the mass map are transformed into real space, and the right hand panel shows the imaginary component. Ideally, the field should consist of purely real values as the mass map is a purely real field, but this is not true for maps made from the data. This imaginary component can be seen as a map of the contribution from systematics and noise. The left hand plot shows the overdensity of foreground galaxies, which should serve as a tracer of the mass distribution. The galaxy map on the left can be seen to share some common features with the weak lensing mass map, but they do not ideally match up. This is partly due to galaxies not being perfect tracers of the mass distribution and partly due to errors introduced in the reconstruction.

Furthermore, the Hyper-Suprime Cam produced a map of the 167deg^2 footprint of their science verification area, managing to produce a three di-

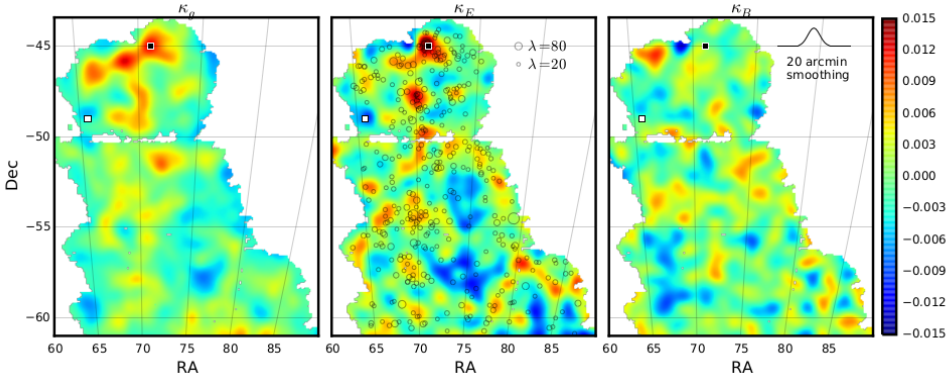

Figure 2.3: Three mass maps made by the Dark Energy Survey using their Science Verification data (Chang et al., 2015). The left panel shows the mass map produced weighted according the number of foreground galaxies, the central panel shows the real part of the mass field reconstructed, and the right panel shows the imaginary part. Ideally, this imaginary component should be zero but noise in the reconstruction means that this is not the case. All maps are smoothed with a Gaussian RMS of 20 arcmin. The circles overlaid on the central panel indicate the location of clusters, with the size of the circle proportional to the estimate mass of that cluster. Red indicates areas of higher density, and blue shows areas of underdensity.

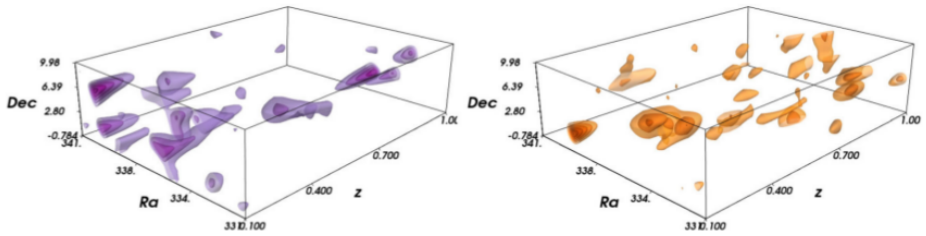

Figure 2.4: 3D mass maps produced by the HSC survey (Oguri et al., 2017). The left hand side shows the mass distribution inferred from gravitational lensing, and the right hand side shows the distribution of the overdensity of galaxies.

mensional output by dividing their source galaxies into different bins (Oguri et al., 2017). Exploring how the integrated mass distribution changes depending upon the redshift of the sources means that the mass can be divided into tomographic bins and mapped through space. Despite the high source galaxy count, the resulting maps were still noisy so a further Wiener filtering was applied to reduce the noise. The final map is shown in Figure 2.4, comparing the distribution of foreground galaxies and the inferred lensing distribution, where there can be seen to be some similarity between the location of visible galaxies and the mass found by lensing.

Maps in cosmology

Producing mass maps using weak lensing measurements can have a variety of different motivations, besides the goal of making the map for its own sake. The successful reconstruction of mass maps can have impact for cosmological constraints. The field of using these maps for cosmological constraints is growing as the reliability of the wide field mass maps improves, and they will become important contributors to accessing information beyond two - point correlations in the next generation of surveys. One such approach is called peak statistics, using identified peaks in the convergence map (Dietrich & Hartlap, 2010; Kratochvil et al., 2010; Yang et al., 2011; Kacprzak

et al., 2016). The frequency of peaks in the convergence field have been shown to vary with cosmological parameters, and through comparison with simulations it is possible to make cosmological constraints. This has been done successfully using CFHTLens data (Liu et al., 2015) and with the Dark Energy Survey (Kacprzak et al., 2016), where the extra information present in the maps can improve on the constraints found from two point analyses alone. Other potential probes include 3 point statistics (Dodelson & Zhang, 2005) and examination of the full probability distribution function of the convergence map (Clerkin et al., 2015; Patton et al., 2017).

Further statistical measures that are present in the mass maps that can be useful for cosmology are the Minkowski functionals. Minkowski Functionals (Petri et al., 2013, 2015; Munshi et al., 2012) are topological descriptors that are used in an attempt to extract information from beyond two point correlation statistics. These functionals describe the topology of a surface as a function of excursion sets; the descriptors are calculated for all areas of a map above a certain threshold value, for a range of thresholds. For example, the surface area of the map above a certain number of standard deviations from the mean is one such measure. Through adding more of these descriptors, it is possible to completely describe the topology of the 2D surface of the mass map. As changing cosmological parameters causes changes in the rate of growth of structure, they can change the appearance of the mass maps. The exact shape of these functionals also change depending upon the cosmological parameters that describe the Universe, and we will discuss our work examining this in further detail in Chapter 4.

2.3.2 Further mass mapping methods

The Kaiser Squires approach is the exact solution for a shear field that is defined at all points and has a uniform noise field. These assumptions are incorrect for modern surveys and can introduce errors in the final map reconstructions (Seitz & Schneider, 1995, 1998), so alternative techniques for producing mass maps have been proposed.

Pires et al. (2009) present another approach that attempts to remove the errors introduced by the limited size of the field in weak lensing masks. They remove errors caused by having holes in the mask by in-painting these regions with values other than zero. Jeffrey et al. (2018) produced mass maps using several different approaches. One map was made using Wiener filtering, where a prior is applied for the convergence field of a Gaussian random field, and this was found to produce improved mass maps. This prior works particularly well on the larger scales, where the distribution is more Gaussian, but at smaller scales where maps hope to reconstruct the non-Gaussian parts of the field it is less well suited. Böhm et al. (2017) has explored a similiar approach using a lognormal prior which is more similar to the mass distribution found in simulations. Another method, `GLIMPSE` (Lanusse et al., 2016) was also applied, which uses a sparsity (Starck et al., 2015) approach. The mass field is assumed to be able to be described by a small number of coefficients, provided that the field is expressed in a suitable domain. This routine seeks to minimise the number of such coefficients used to produce the mass map, whilst still being in agreement with observational data. The coefficient basis that the routine seeks to minimise is called the dictionary, and the choice of basis is very important for sparsity based approaches. The `GLIMPSE` approach uses the starlet (Starck et al., 2007) and seeks to describe the mass distribution using the minimum number of spherically symmetrical, dark matter haloes. Whilst this may not be strictly true for the Universe, the method was shown to produce maps that correlated more strongly with a known matter field than the Kaiser Squires approach. Currently, this approach is only applied on flat surfaces.

2.4 Mass mapping on the sphere

Here we briefly describe the relevant weak lensing formalism in relation to mass mapping on the sphere. The previous sections all considered map reconstruction on a surface that can be approximated as flat, and the following

section discusses moving into a regime more appropriate for the upcoming generation of surveys, which will map significant fractions of the sky.

In the following section we shall follow the spherical harmonics approach described in Castro et al. (2005). The large observational area of modern surveys mean that a full sky treatment is required, which is achieved by utilizing techniques commonly used in CMB analyses (Leistedt et al., 2017; Heavens, 2003; Kitching et al., 2014).

E and B mode decomposition

It is necessary to introduce the concept of E-mode and B-mode decomposition when considering transforming shear data into harmonic space. The shear field on the sky can be considered as composed of one real and one imaginary component, which are orthogonal to each other. The shear field can be viewed as a field that, for a rotation of ϕ, undergoes a rotation of $e^{-2i\phi}$, in a similarly way as the Stokes polarisation parameters behave. These combine to form a field which transforms with the properties of a spin-weight 2 object, and can be decomposed into odd (B) and even (E) scalars, ϕ_B and ϕ_E respectively.

2.4.1 Direct inversion on the sphere

Castro et al. (2005) defines a *lensing potential* ϕ at a given spatial coordinate $\mathbf{r} = (r, \theta, \psi)$ by

$$\phi(r, \theta, \psi) = \frac{2}{c^2} \int_0^r dr' \frac{f_K(r - r')}{f_K(r) f_K(r')} \Phi(r', \theta, \psi), \tag{2.29}$$

where Φ is the Newtonian potential and f_k is a comoving angular diameter distance, taking values of $(\sin r, r,$ or $\sinh r)$ for a Universe with curvature described by $k = 1$ (closed), 0 (flat) or -1 (open) Castro et al. (2005). The coordinate r is a radial distance and (θ, ϕ) refer to angular positions on the sky. This potential can be related to the matter density through Poisson's equation

$$\nabla_r^2 \Phi(\mathbf{r}) = \frac{3\Omega_m H_0^2}{2a(t)} \delta(\mathbf{r}), \tag{2.30}$$

where Ω_m is the present day total matter density parameter, H_0 is the Hubble constant at the present time, $a(t)$ is the scale factor, and $\delta(\mathbf{r})$ is the density contrast at position $\mathbf{r}$.

Following the example of Castro et al. (2005), I will now consider the case of a scalar field $\phi(\mathbf{r})$ in a flat background geometry, which can be transformed into the basis of spherical harmonics and spherical Bessel functions via

$$\phi_{\ell m}(k) = \sqrt{\frac{2}{\pi}} \int \mathrm{d}^3 r \phi(\mathbf{r}) k j_\ell(kr) Y^*_{\ell m}(\theta, \varphi) \tag{2.31}$$

Through the introduction of a geometrical differential operator $\eth(\bar{\eth})$, which raises (lowers) the spin of the field, ψ can be related to the shear γ and convergence κ through the following relations:

$$\kappa(\mathbf{r}) = \frac{1}{4}(\eth\eth + \bar{\eth}\bar{\eth})\phi(\mathbf{r}), \tag{2.32}$$

$$\gamma(\mathbf{r}) = \frac{1}{2}\eth\eth\phi(\mathbf{r}), \tag{2.33}$$

where $\gamma(\mathbf{r})$ is composed of two orthogonal components

$$\begin{aligned} \gamma_1(\mathbf{r}) &= \frac{1}{4}(\eth\eth + \bar{\eth}\bar{\eth})\phi(\mathbf{r}) \\ \gamma_2(\mathbf{r}) &= -\frac{i}{4}(\eth\eth + \bar{\eth}\bar{\eth})\phi(\mathbf{r}) \end{aligned} \tag{2.34}$$

Furthermore, as shear is a spin-2 field, it will decompose into spin-2 weight spherical harmonics (${}_2\gamma_{\ell m}$), known as E and B modes, that are free of curl and divergence respectively. In the single thin lens plane case, it can be shown that the lensing information is contained within the E mode coefficients (Castro et al., 2005), and that the B mode coefficients should only be non-zero in the presence of noise. Multiple lenses can give rise to a small B mode, but these will be negligible given our signal-to-noise. Because of the $\eth$ operator rules for spherical harmonics, the equations relating coefficients for ϕ, κ, γ and lensing deflection α are:

$${}_2\gamma_{\ell m}(k) = -A_{E,\ell m} = \frac{1}{2}\sqrt{\frac{(\ell+2)!}{(\ell-2)!}}\phi_{\ell m}(k), \tag{2.35}$$

$$\kappa_{\ell m}(k) = -\frac{\ell(\ell+1)}{2}\phi_{\ell m}(k), \tag{2.36}$$

$$\alpha_{\ell m} = \sqrt{\ell(\ell+1)}\phi_{\ell m}(k), \tag{2.37}$$

where $\phi_{\ell m}(k)$ and $A_{E,\ell m}$ are the coefficients of the lensing potential and E modes respectively, in spherical harmonics. Using these quantities in harmonic space, we can transform an observed sky shear signal to maps of the quantities κ, α and ϕ, in a similar way to previously done in Fourier space.

It is also worth briefly considering the implications of these relations for the prospect of producing good quality final maps; the factor relating $\kappa_{\ell m}$ to $\gamma_{\ell m}$ is approximately 1 for large ℓ meaning that shape noise will affect both in a similar fashion. On the other hand, α (ϕ) scales with ℓ^{-2} (ℓ^{-4}) so the effect of the survey mask dominates. This is due to γ being a second order derivative of the lensing potential, and α is a first order differential, resulting in ϕ and α applying a greater relative weight to the lower ℓ modes than κ. The lower ℓ modes correspond to larger scales on the sky, which become less constrained in the presence of a mask and hence degrade the reconstruction of these fields.

Observational mass maps on the sphere

Using the formalism described in the previous section, I have worked with colleagues in the Dark Energy Survey to map the Year 1 data, producing the largest map of the matter distribution made using measurements of the weak lensing of galaxies (Chang et al., 2018). This map applied the direct inversion on the shear measurements of galaxies, pixelised into HEALPix coordinates and transformed into spherical harmonics, to produce a contiguous map of $\approx$ 1500deg^2, which is shown in Figure 2.5 with massive clusters overlaid. Source galaxies were selected from a distant redshift bin spanning $0.63 < z < 0.9$ and clusters were selected at lower redshift. This bin was found to have the highest signal to noise, due to a combination of having a sufficiently large number of source galaxies and higher redshift bins have a stronger lensing signal. In Chang et al. (2018), we tested the maps using a variety of statistical

metrics and examined for systematic effects, finding that we could produce reliable mass maps on this scale using this method. The largest area of under density on the Y1 data mass map supported a model of two large supervoids present along the line of sight at a position of (RA, Dec)=(62 deg , -43 deg), and that areas of under density in the mass maps could typically be related to similar voids in the large scale structure of the Universe. Several interpolation methods were attempted to try and reduce errors introduced by missing pixels in the maps, but none of these produced maps that were more accurate that the direct inversion approach on the masked sky.

Figure 2.7 shows a different map that I produced using the direct inversion pipeline, displaying the potential and lensing angle as described in equation 2.37. These measures are more vulnerable to the mask effects than the convergence maps, but can be shown to be reconstructed reasonably well in the larger survey areas mapped by DES. I analyse the accuracy of the maps in Figure 2.6 through the use of simulated γ maps, quantifying accuracy using the F statistics that will be more thoroughly defined in the next chapter. Briefly, F_1 describes the accuracy with which the amplitude of the field is reconstructed and F_2 describes the accuracy of the phase information. In both cases, a value of 1 indicates a perfect reconstruction. All maps were made at an `nside` =1024 and to a maximum $\ell = 2047$, and the outer 10 arcminutes of the mask were excluded from the analysis to remove edge effects from the κ map. For κ, both F statistics are very close to 1, as edge effects have been largely removed as we consider the central areas of the survey footprint where both the phase and amplitude information is well reconstructed. For the two lensing angles $\eta^{1,2}$, which apply a great weight to lower ℓ modes than the κ inversion, the limited survey mask means that the reconstruction is significantly worse across all statistics. There is a difference for the two lensing angles because they refer to different directions on the sky, and the mask covers different fractions of the sky in different directions. In the case of ϕ, the degradation from the imposition of a mask is significantly worse, than for η as it is even more heavily weighted to the poorly constrained, low

ℓ modes. Both η and ϕ are less adversely affected by the introduction of shape noise than the κ map, as this predominantly affects the lower ℓ modes.

Maps of the lensing angle could have future potential applications in CMB delensing (Marian & Bernstein, 2007; Manzotti et al., 2017), or to correct a field of galaxy positions to remove the lensing contribution to their apparent location (Chang & Jain, 2014). Due to the survey size of previous studies, maps of the deflection angle and gravitational potential are rarely published, but they will become increasingly feasible over the coming years and will open up new applications for weak lensing mass maps, and Figure 2.7 is an exciting first exploration of their potential future production using a data set on the sphere.

The results from the Dark Energy Survey Year 1 data show the promising future of mass mapping using weak lensing, where increasingly large maps will be produced. However, these maps were all made using the direct inversion approach, which will introduce errors into the final map in the presence of a mask. Chang et al. (2018) showed that simple interpolation techniques could not mitigate these edge effects, and a more sophisticated approach is required. This will be even more important for maps made of η and ϕ, which are more mask dominated. In the next chapter, I will introduce my work on developing a pipeline which improves the accuracy of weak lensing mass maps.

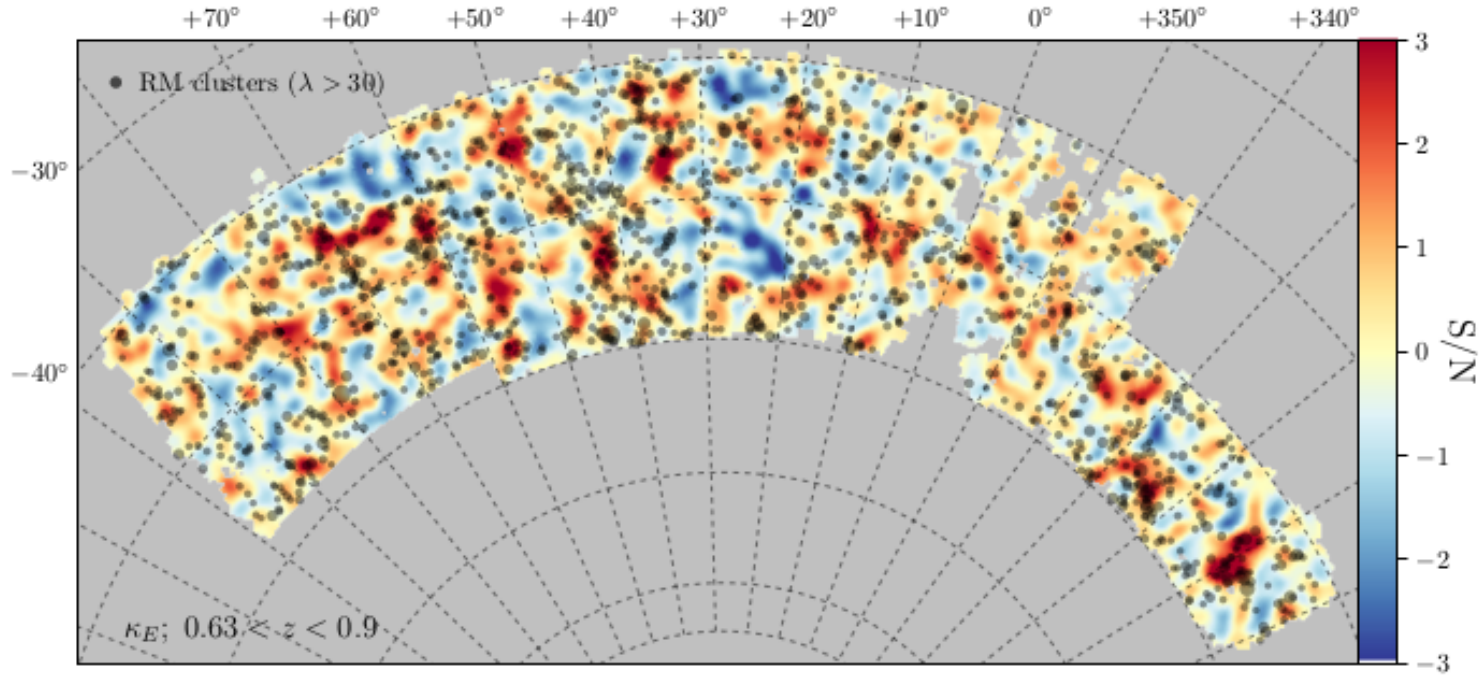

Figure 2.5: Mass map produced in the DESY1 analysis (Chang et al., 2018) using the direct inversion method, with clusters overlaid. The size of the black circle is linearly proportional to the estimated mass of that cluster, from the RedMaPPer catalogue.

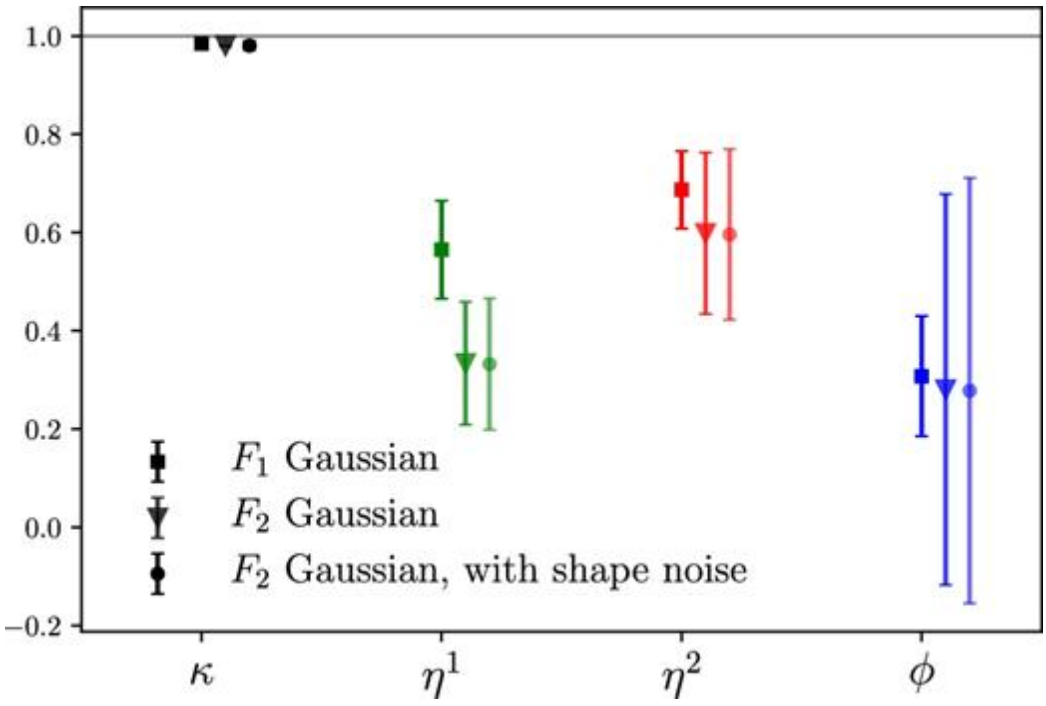

Figure 2.6: Evaluating the fidelity of the lensing maps made from masked skies for the DESY1 footprint. These were measured using Gaussian simulations of true κ skies described in Section 3.2.1, and metrics described in 3.1.4. A value of 1 for all measures shown in this plot indicates an accurate reconstruction, and deviations from 1 show errors in the map. F_1 shows how well the amplitude is reconstructed, and F_2 measures the accuracy of the phase information. The maps of the lensing angle (η) and gravitational potential (ϕ) rely on larger contributions from low ℓ modes than the κ map, so are more severely degraded by the imposition of a survey mask but are not as affected by the introduction of shape noise.

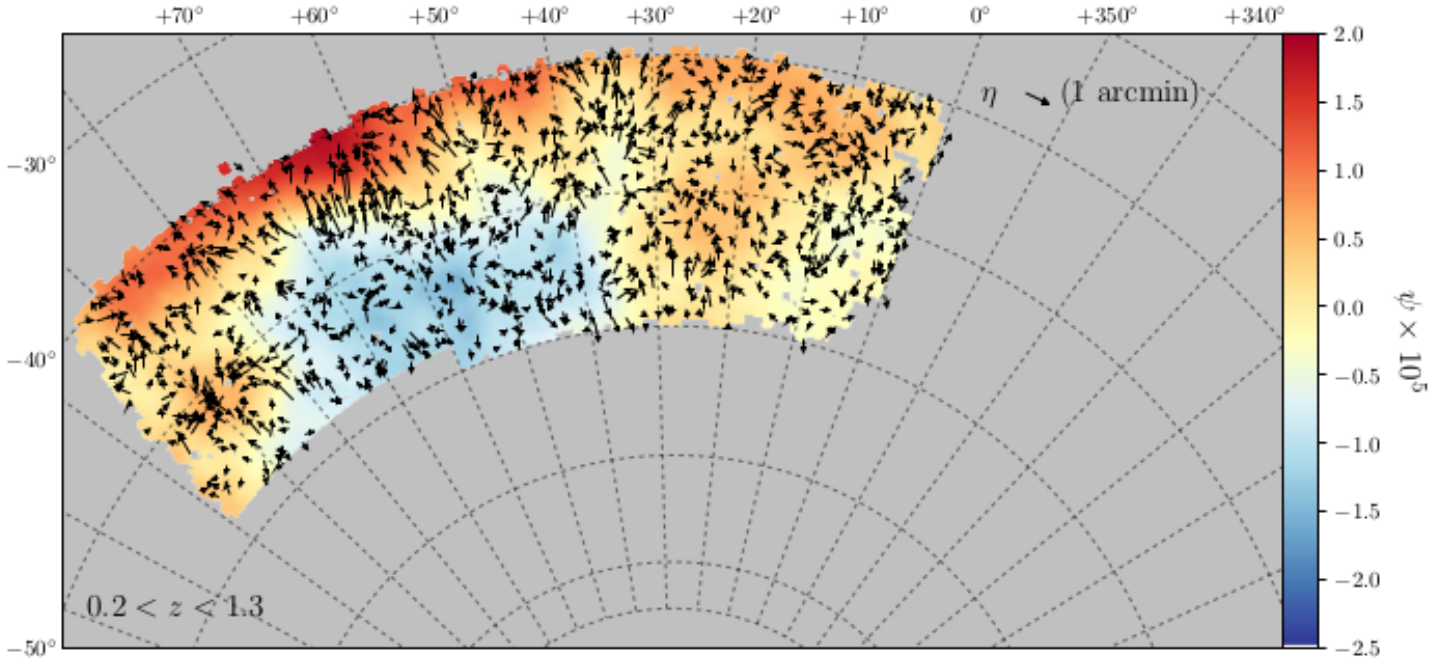

Figure 2.7: A map of the lensing potential reconstructed from DESY1 data, with the lensing displacement overlaid as a vector quantity (Chang et al., 2018). This map made use of the `MetaCalibration` catalogue.

Chapter 3

Improving mass maps through forward fitting in harmonic space

This thesis will consider two different approaches to producing mass maps with weak lensing measurements - the Kaiser-Squires reconstruction introduced in Chapter 2 and applied directly to the data, and a forward-fitting method utilising hypothesised full-sky shear fields. Both are expressed in spherical harmonics, the relationship between a γ field and the resulting κ field uses the same pipeline, i.e the Kaiser-Squires inversion. However, they do differ through the shear fields used, as the forward fitting model uses hypothesis full-sky shear fields, and the direct inversion uses shear for the limited region where we have data on the sphere. In this chapter, this pipeline will be introduced, extensively tested on simulations and then applied to data from the Dark Energy Survey.

3.1 Methodology

We intend to produce maps using weak lensing information from a modern cosmological survey, and to do so in such a way that we can reduce the errors

introduced by using the direct inversion. In order to produce maps on the scales covered by DES Y1, a package that utilises the spherical approach is needed. This is because DES covers such a fraction of the sky that a flat approximation is no longer valid, meaning that either a series of flat maps need stitching together or a full spherical approach is needed. We use the `healpy` suite which is a python wrapper for `HEALPix`[1], software which is designed to handle data on the sphere and initially developed for use with the cosmic microwave background. The spin-2 γ observations are analogous to the polarization Stokes parameters Q and U used in CMB studies (Castro et al., 2005), so there is a useful parallel between the two studies. Galaxy shapes are measured for an entire catalogue of observed objects, and these are then placed into pixels on the sky depending upon their angular coordinates. Each shape measurement contributes to calculating the average shear in that pixel, with an associated shot noise. Estimated maps of γ_1 and γ_2 can be used in the function `map2alm` to produce their spherical harmonics coefficients in the form of the divergence free $B_{\ell m}$ and the curl free $E_{\ell m}$, using the equations described in Section 2.4.1.

3.1.1 The Dark Energy Survey

The Dark Energy Survey is a photometric survey using the Dark Energy Camera (Flaugher et al., 2015) on the Blanco telescope, a 4m telescope at the Cerro Tololo Inter-American Observatory in Chile. Observations are taken in five bands ($grizY$). This thesis will make use of the data from the first full year of observations, also known as the DES Y1 cosmology data set, or Y1A1 GOLD (Drlica-Wagner et al., 2018). This footprint is the one best suited to the application of the mass mapping techniques to date, as it spans a substantial survey area of 1800 deg^2 and contains sources up to a redshift of $\simeq 1.3$.

[1] http://healpix.sf.net/

3.1.2 Direct inversion

The Kaiser-Squires approach on the sphere uses the E modes found from a spherical transform of a shear field to produce convergence coefficients; the B mode coefficients $B_{\ell m}$ are representative of noise and serve as a useful null test for possible systematics and noise. The resulting κ map is made by transforming from harmonic to pixel space, using the reverse transform `alm2map`, with κ and ϕ using the spin-0 case of the transform and α the spin-1 case (equations 2.36 and 2.37). The output is a `healpy` map, pixelised to a chosen resolution, and then smoothed using the `pixelfunc.smoothing` function. Producing maps at a higher resolution reduces the magnitude of the edge effects, and smoothing improves the signal to noise. This is because having a higher *nside* means that there are more pixels in the map, increasing resolution by decreasing the size of a pixel. The increased number of pixels mean that the edge effects penetrate a smaller angular distance into the mask despite influencing a similar number of pixels. The smaller size of the pixels means that they will typically contain fewer galaxies than the pixels at a coarser resolution would, with the result that shape noise also becomes larger. This can be mitigated by smoothing the map to a resolution of a lower *nside*, as this means that the signal can be increased relative to the noise. For example, in Chang et al. (2018) we produced mass maps at an `nside` =1024, and then smoothed these maps with a Gaussian of $\sigma = 20$ arcmins, which is close to the pixel size at an $nside = 256$. Despite these attempts at mitigating the errors inherent in the direct inversion method, it is not possible to completely remove the edge effects and artefacts in the final map will still be present. When discussing the mass mapping pipeline, will refer to making maps this way, from a finite survey area, as the *direct inversion* method. All of the following maps in this chapter are displayed using the Albers Equal Area projection and using `SKYMAPPER` [2].

Figure 3.1 shows simulated skies fromSection 3.2.1 reconstructed with the direct inversion. For the first approach, on the top row, full skies of shear

[2]https://github.com/pmelchior/skymapper

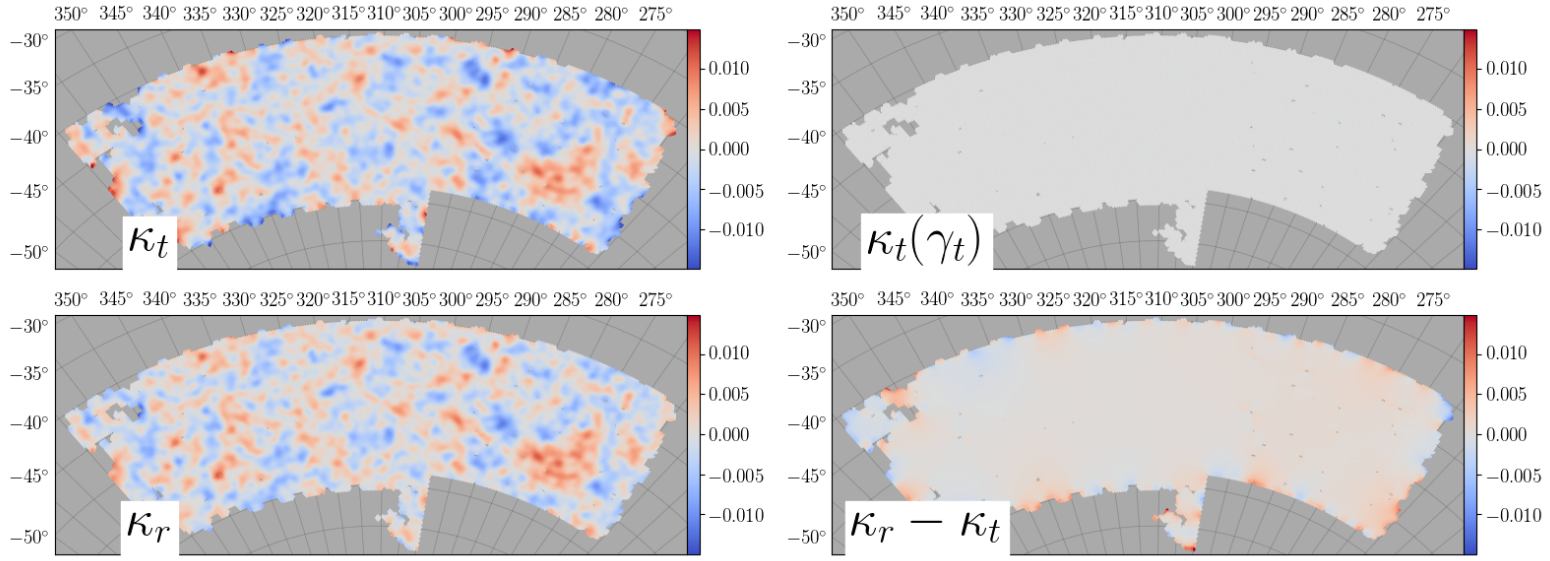

Figure 3.1: Comparison of reconstructions performed using κ_t, γ_1 and γ_2 on maps of `nside`=256, corresponding to a pixel width of $\sim$ 0.23 deg and smoothed with a Gaussian kernel with $\sigma = 20$ deg. Upper left shows a true κ distribution from a Gaussian simulation described in 3.2.1, and the upper right shows the residuals for a reconstruction of this field when using the full sky of γ_1 and γ_2 values, without shape noise added. Lower left shows the reconstruction of the map using shear values from only the survey region, and the lower right the residuals for this approach. Comparing the two right hand plots shows clearly that considerable residuals can arise in the edge pixels of the survey footprint, even before the addition of shape noise, and the scale of this noise contribution can be of a similar size to the κ field that we are attempting to reconstruct.

data are produced and the associated κ field is defined. Using a full sky of known γ (top row), the reconstruction from γ to κ works in such a way that residuals (top right) are negligible. We apply a mask after the reconstruction for visualisation purposes. The reconstruction works perfectly here because all of the assumptions present in the Kaiser-Squires formalism are satisfied - the full field is sampled, with a uniform (0) noise field. Therefore, the κ field can be exactly defined because we have complete information, with the only errors potentially being introduced from computational error. It is therefore still important to check this reconstruction pipeline works, and to ensure that the errors are only coming from the edge effects in the κ reconstruction. The negligible residuals shown in the top right plot mean that we can be confident in the γ to κ pipeline working as expected, and begin analysis of the direct inversion in more restrictive conditions.

Considering the bottom row of figure 3.1, we now examine the effect of the direct inversion method when we introduce a mask, covering an area of 1000 deg^2. When a limited area of shear information is used, the reconstruction introduces significant errors along the edges of the data footprint (right bottom). This arises due to the assumption that the complete field is sampled, when in reality it is not; unobserved regions of the sky are treated as having zero shear and some bias in the true harmonic coefficients is introduced. These errors are significant fractions of the typical κ values, as apparent when comparing the size of residuals in Figure 3.1 to the true κ field. For example, many regions pixels are deviate from the true value by 0.005 to 0.01, which corresponds to sizeable fluctuations in the true field and could easily be misinterpreted as cosmological structure. This can result in significant contamination of the recovered map. It is worth noting that this is the scenario when all of the shear in the masked region is exactly known, and we have not yet introduced shape noise into the reconstruction. Adding shape noise to this map would further degrade the reconstruction, especially if it is an inhomogenous noise field such as one derived from galaxy shape estimates, where the number of galaxies will vary from pixel to pixel. This

reconstruction using perfect shear is still a useful case to highlight the signal introduced solely due attempting to produce mass maps using the direct inversion on a masked field, meaning that this method will never be able to reproduce the exact κ field in the case of masked data, even in the case of a perfectly known shear measurement.

3.1.3 Forward fitting approach

We have developed a forward fitting approach with the aim of mitigating some of the limitations of the direct inversion. The latter was initially developed with two assumptions - that the field is uniform in its noise, and that the shear field is completely observed. Creating mass maps with a field that has been observed over a fraction of the sky and with a non-uniform noise distribution will violate these assumptions and therefore introduce errors in the reconstructed map, as demonstrated in the previous section and in literature (Seitz & Schneider, 1995, 1998). The motivation for the forward-fitting technique is therefore to produce maps using the usual relationship between γ and κ fields, but to do so in such a way that they are made without transforming the limited shear measurements directly into spherical harmonics.

Our technique instead hypothesises a full sky of shear values, and then compares this hypothesis to the observations. Thus, the masked data does not directly enter the transform and the edge effects introduced by the direct inversion are removed. Instead, the full sky hypothesis of shear measurements can be used to produce a mass map. Comparing a region of the hypothesised sky γ values to the observed γ, with well estimated errors for the shear in each pixel, allows for these realisations to become constrained by the data.

Our technique produces spherical harmonics characterising a full sky of shear observations, which can then be converted back into observable maps of γ_1 and γ_2. A forwards fitting routine was written in `python` and made use of the packages `healpy` and `numpy`[3]. The whole procedure is shown graphically in Figure 3.2, and described below:

[3]https://docs.scipy.org/doc/

- An initial shear hypothesis, $A^{hyp}_{\ell m}$, is made in harmonic space (up to an ℓ of $2nside - 1$), and transformed to give its corresponding full sky shear fields γ through use of the `healpy` function `alm2map`. We choose to make our initial hypothesis through generating an E mode harmonic corresponding to a Gaussian random sky with σ typical of the observed galaxy overdensity field. We do not use the actual overdensity field to inform this initial hypothesis, beyond using it as an estimate of the size of fluctuations in the field. This initial guess is far from the minimum, but early hypotheses make large steps down the likelihood surface.

- The hypothesised shear field is compared to limited observed data on the sphere γ_{obs} with known errors σ_γ by calculating its likelihood. Assuming Gaussian errors and independent measurements, the log-likelihood is given by

$$\chi^2 = \sum_{i \in \mathrm{footprint_{pix}}} \frac{(\gamma_{\mathrm{hyp},i} - \gamma_{\mathrm{obs},i})^2}{\sigma^2_{\gamma,i}}, \tag{3.1}$$

  where $\mathrm{footprint}_{pix}$ is the set of pixels contained in the survey footprint. We use this as we find that the diagonal term to the covariance is dominant, and a full pixel by pixel covariance matrix is prohibitively computationally expensive for the level of reolution that we aim to achieve. To test this assumption, we investigated the covariance of a pixel with its neighbour across simulated maps: we find that the covariance with respect to the immediately neighbouring pixel is at a value approximately 4.5% of the variance within the pixel, and the corresponding inverse covariance matrix is well approximated as diagonal with elements equal to the reciprocal of the variance. For calculating the reduced χ^2, our number of degrees of freedom is equal to the number of pixels in the survey area.

- $A^{hyp}_{\ell m}$ serves as the basis for a series of similar sets of harmonics, A^j_{lm}, produced through randomly perturbing the coefficients of the m modes of a randomly chosen ℓ mode, by adding a contribution to each m drawn

independently from identical Gaussian distributions with standard deviation σ determined by the power in the current best hypothesis at that ℓ mode. We choose to produce 10 perturbed hypotheses, each differing from each other by altering the coefficients at a single ℓ mode.

- Each of these altered hypotheses A^j_{lm} are transformed to produce shear maps γ^j which are then compared to the data and the corresponding likelihood calculated.

- The hypothesis with the greatest likelihood is adopted as the new A^{hyp}_{lm} for the next iteration of the routine.

- The cycle repeats until consistency with the data is found (reduced $\chi^2 < 1$) or a plateau reached, from which insufficient improvements to the fit are made above a threshold number of attempts. For the results in this thesis, we chose this number to be 500 generations without improvement as the exit condition. In practice, in the DESY1 footprints that we will consider later, no fits failed to reach a reduced $\chi^2 = 1$.

The final A_{lm} can be used directly as E_{lm} in equations 2.36 and 2.37 to produce a convergence map. Repeated runs of the fitting algorithm produce a sampling of consistent maps (reduced $\chi^2 < 1$). The varying noise across the field is accounted for by comparing our noiseless hypotheses to pixelised data in observed space, and non-stationary noise never enters the transform from shear to mass map. We produce a final map from the average of the many fitted maps; we will show in later tests that this map provides an unbiased reconstruction of the mass distribution, and assess the errors associated with it in Appendix A.

The runtime of the routine is predominantly affected by two variables - the momentum of the gradient descent and the `nside` resolution of the field being fitted. The size of the perturbation changes how significantly the parameters change at each iteration, so impacts upon the rate at which the likelihood changes, and higher resolution maps have more spherical harmonics to fit as well as more pixels to fit to, although this is mitigated slightly by the fact

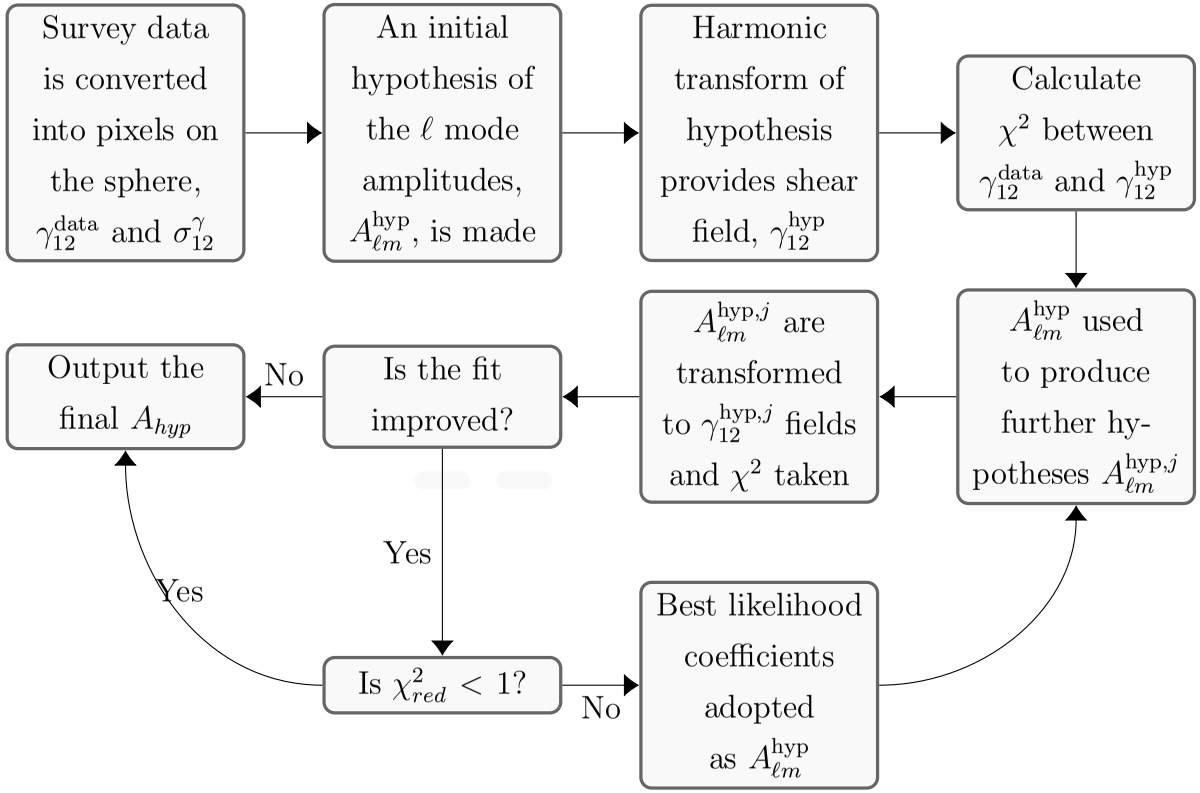

Figure 3.2: Graphical representation of the forward fitting routine, describing the iterative nature of the process. Hypotheses are produced in the harmonic space and compared to the data in real space, gradually increasing the likelihood through subsequent selection of improved hypotheses.

that the error in each pixel will be larger. To optimise the fitting time, we need to minimise the number of steps taken to reduce the likelihood. We find that our routine can perform 20,000 generations of 10 hypothesis fields at an `nside` = 256 and return an output map in $\simeq$24 hours. Each fitted field was produced on the SCIAMA supercomputer, using 8 cores. The direct inversion is significantly quicker, taking a maximum of one minute for a field of the same resolution. Due to the nature of the fitting routine, the direct inversion will always be significantly quicker than the forward fit, as the forward fitting pipeline is essentially many thousands of direct inversion mass maps using hypothetical shear fields.

This method is optimised for producing maps on the sphere, as opposed to the techniques which assume a flat field introduced in Sections 2.3.1 and 2.3.2, which makes a direct comparison difficult. Tiling many small areas which can be approximated as flat can be used to produce these large maps, but the resulting map will not be as accurate as one made directly on the sphere. Wallis et al. (2017) explored the impact of projecting flat mass maps onto the sphere, and found that it was not possible to remove errors introduced through approximating the surface as flat, and stated that these errors could account for up to 50% of the total error budget in future mass maps, meaning that making maps directly on the sphere is of great importance for future data. Although we do not compare maps made from our method to those made using flat approximations, this could be done either by producing maps of sufficiently high resolution as to be comparable to those made on the flat, or by implementing a tiled version of the algorithms introduced in Section 2.3.2, which we leave for future work.

Presence of priors

Many alternatives to the direct inversion approach achieve their improved mass map reconstructions through the introduction of a prior assumption on the form of the resulting mass map. Wiener filtering, for example, assumes a Gaussian signal is being constructed in the final mass map, as shown in

(Jeffrey et al., 2018). Other methods in Section 2.3.2 similarly tend to introduce a prior, reducing the error by including a bias in the final map. In the forward fitting method, there are no hard priors on the statistics of the resulting mass map. Whilst perturbations to the spherical harmonics coefficients are drawn from a Gaussian distribution, this does not necessarily introduce a Gaussian prior into out mass maps. At a first perturbation, each coefficient of a given ℓ mode is perturbed by an amount drawn from a Gaussian. If lower χ^2 measurements are found by minimising a coefficient m_1 and by maximising another m_2 for a particular ℓ, the perturbations that produce this will be selected. On the following step, each coefficient is then perturbed again and those which produce the desired behaviour in m_1 and m_2 will be preferentially selected, meaning that the resultant distribution of the ℓ mode coefficients will not be constrained to producing Gaussian fields. A similarly argument holds for isotropy, where whilst there is no preference for which m are perturbed in our method, the calculation of a likelihood using the data allows for this to be introduced. This means that the only prior which is introduced in the forward fitting model is that the entirety of the signal in the shear field arises from E modes, as we set our B modes to the idealised case of zero. Future work will allow both contributions to vary.

3.1.4 Examining the reconstructions

Accurately describing how well one method is reconstructing the κ field requires careful quantification, through a variety of metrics that consider both the spatial distribution of the map and the distribution of convergence values present within it. In order to compare the maps, we will define several statistics which will be used.

F Statistics

The first of these statistics will be the F statistics, which are defined as:

$$F_1 = \sqrt{\frac{\langle \kappa_{rec}^2 \rangle}{\langle \kappa_t^2 \rangle}};\ F_2 = \frac{\langle \kappa_t \kappa_{rec} \rangle}{\langle \kappa_t^2 \rangle}. \tag{3.2}$$

F_1 measures the consistency with which the amplitude information of the maps is preserved, whereas F_2 is sensitive to how well phase information is recovered. This can be seen by the fact that F_1 is only concerned with a statistic that is defined across the whole map, the variance, whereas F_2 directly compares the pixel value in one map to that in another map before aggregating the statistic. A result of unity for both statistics would mean that the reconstruction is managing to perfectly capture both the phase and amplitude information in the map. Both statistics are needed because one could conceivably produce a map that gives a perfect result for either single F metric, but both taken together can give useful information on the maps. Once the behaviour of our fields' F_1 is understood, we may be able to account for any changes in amplitude by applying a corrective multiplicative factor across the map, but if F_2 is significantly degraded then this indicates that phase information is lost in the final result. Therefore, we want F_2 to be as high quality as possible, and F_1 to be well understood. For example, a reconstruction method could reconstruct the exact phase but with an amplitude related to the true field by a constant factor, which would be easily corrected by examining F_1, but it is not so easy to correct for the lost phase information.

Furthermore, when we measure these statistics in maps including shape noise, it becomes important to correct for the effect of this noise contribution, which we call "denoising" of the statistics. To highlight this issue, consider a reconstructed map κ_{rec} which we can model as being composed of two parts:

$$\kappa_{rec} = \alpha \kappa_{sig} + \kappa_n, \tag{3.3}$$

where κ_{sig} is the reconstruction of the true convergence from the true shear, and the κ_n term encapsulates all other noise effects that alter the convergence

from its true value, such as edge effects and noise in the measurement of the shear in pixels. When considering the variance of κ_{rec} when expressed in this form, it now becomes apparent that the result will consist of a negligible noise-signal correlation (as they are not expected to correlate), and signal and noise autocorrelations which will be non zero. Comparing the measure for κ_{rec} to that for κ_{sig} therefore is difficult to interpret until the noise contribution is subtracted, and the true amount of signal that is recovered can be measured. If we can successfully model the noise on the κ maps, then we can correct for this noise in F_1; our denoised F_1 therefore becomes

$$F_1 = \sqrt{F_{1,N}^2 - F_{1,n}^2}, \tag{3.4}$$

where $F_{1,n}$ is the statistic found when producing a map that consists solely of noise, and $F_{1,N}$ is the statistic found from the initial noisy data. We assume that there is no correlation between the convergence κ and the noise in that pixel. The denoising procedure serves as an important test of how well we can model the noise across the map, which is of particular importance when we later attempt to reconstruct moments of the true κ distribution, a useful cosmological probe. A denoising procedure that recovers F_1 statistics close to unity indicates that both the reconstruction and the noise are behaving as expected. The F_2 statistic does not require any denoising, under the assumption of no correlation between κ_{true} and the noise contribution. This can be seen by substituting equation 3.3 into equation 3.2. Introducing systematics into the maps would change the F_2 statistic, through adding a correlation between the reconstructed map, and another quantity unrelated to the true κ field.

F statistics are measured using the pixels of the whole map, so information on intermediate scales is lost. These statistics could be measured across a range of smoothing scales to examine the how well the methods work as a function of scale, but this work leaves analysis of the reconstruction across scales to other metrics. The moments of the field, as a function of smoothing scale, shown in Figure 3.6, is one such test of the reconstruction as a function of scale. The de-noised second moment is the same statistic as the de-noised

F_1 measure. Alternatively, comparing power spectra would give an indication of the performance of the maps at different scales.

Minkowski Functionals

Another set of statistics of interest are the Minkowski Functionals, which encode the topological information of a map (Mecke et al., 1994a) and are therefore useful to constrain cosmological models (Kerscher et al., 1996; Schmalzing et al., 1996; Petri et al., 2015), and particularly well suited for the analysis of maps.

Following the notation of Hikage et al. (2006) and Munshi et al. (2012), the three Minkowski Functionals (V_0, V_1, V_2) for a 2D surface are defined as

$$V_0 = \int_\Sigma \mathrm{d}a,$$
$$V_1 = \frac{1}{4}\int_{\partial\Sigma} \mathrm{d}l,$$
$$V_2 = \frac{1}{2\pi}\int_{\partial\Sigma} K\mathrm{d}l,$$

They can be interpreted as representing integrals across the total area, length and curvature characteristic of a given excursion set of the map respectively, where an excursion set is defined as all parts of a surface that exceed a given value. A useful analogy is to consider areas a familiar mapped surface of the Earth, with areas of large hills and low troughs below sea level. If we wanted to entirely characterise this surface, we would measure the functionals at different heights relative to sea level. Once we know the area, perimeter and gradients describing the topology of the areas of the terrain above certain heights, we would be able to fully characterise it. The peaks and troughs present in the mass maps can be imagined as a similar scenario.

We calculate the functionals through the use of angular derivatives on the sky (Schmalzing & Górski, 1997), using the formulae listed in Appendix A of Hikage et al. (2006). Each are normalised by the area of the complete map. We estimate derivatives through finite differences between neighbouring pixels in a similar way to Petri et al. (2015) but implemented on the

spherical pixel scheme used in these maps. The exact formulae that were coded in order to calculate the functionals from a given `HEALPix` map are shown below, considering the curvature of the sky and a pixelised surface. The three functionals for an excursion set of size ν in a field u that has been normalised by its standard deviation, are described by

$$V_0 = \mathcal{H}(u - \nu), \tag{3.5}$$

$$V_1 = \frac{1}{4} F(u - \nu) \sqrt{u_{;\theta}^2 + u_{;\phi}^2}, \tag{3.6}$$

$$V_2 = \frac{1}{2\pi} F(u - \nu) \frac{2u_{;\theta} u_{;\phi} u_{;\theta\phi} - u_{;\theta}^2 u_{;\phi\phi} - u_{;\phi}^2 u_{;\theta\theta}}{u_{;\theta}^2 + u_{;\phi}^2}. \tag{3.7}$$

$\mathcal{H}$ denotes the Heaviside function, which is equal to 1 when evaluated for a value above 0 and equal to 0 otherwise. F denotes $1/\Delta\nu$, the size of the interval between excursion thresholds. The coordinates θ, ϕ refer to angular positions on the sky and a semicolon denotes a partial derivative. We use this formalism in a `python` code to calculate the functionals from `HEALPix` maps, making use of the function `get_all_neighbours` to select pixels north, south, east and west of the pixel for calculating gradients. Through this code, we can measure the topology of any map as a function of the excursion parameter, and compare the resulting curves.

Pearson Correlation

Finally, we will also use the Pearson Correlation coefficient, defined as

$$\rho_{X,Y} = \frac{(X - \hat{X})(Y - \hat{Y})}{\sigma_x \sigma_y} \tag{3.8}$$

For a perfect correlation of X and Y fields, this will be exactly unity, and deviations from this value provide a measure of the level to which noise can dominate the signal.This statistic does not need a de-noising approach, as the amplitudes of each map are normalised out by the denominator. In our analysis, we will be using a reconstructed field and a true κ field as X and Y.

3.2 Simulations and initial tests

In this Section we will use simulations of observed γ fields with known κ fields to compare the two reconstruction methods, using the metrics introduced in Section 3.1.4. In all further maps in this chapter, results are for final fitted maps of `nside`= 256, with a pixel separation of 0.22 deg unless otherwise stated.The motivations for this are two fold - the noise present in the shear maps means that many structures at scales below this will not be due to cosmological lensing, and that the time taken to fit a map depends upon the number of spherical harmonic coefficients being fitted. Fewer coefficients means a faster exploration of the likelihood space. We use a maximum ℓ mode of 2 `nside` - 1 = 511, for sufficient resolution and speed, as including higher ℓ modes introduces further errors from the spherical transform. Maps are then smoothed with a Gaussian with standard deviation $\sigma = 20$ arcmins, slightly larger than the pixel size but comparable to the maps produced in Chang et al. (2018). We will show that the forward fitting routine consistently performs better than the direct inversion, across a variety of metrics. In Chang et al. (2018), we produced maps to a resolution of `nside`= 1024, and results found here are not necessarily directly comparable due to the different resolutions. We choose to make the maps through the direct inversion at a resolution of `nside` =256, instead of using the smoothing approach as in Chang et al. (2018), so that the results are more directly comparable. In practice, this produces direct inversion maps that are less accurate than those we present in Chang et al. (2018).

3.2.1 Gaussian map tests

The precision and accuracy of each reconstruction technique needs to be carefully assessed, for both the forward fitting approach and for the direct inversion. There are several different effects that will immediately degrade the reconstruction: the limited survey footprint, and the fact that we observe a shear estimate using a varying number of galaxy ellipticities, which

introduces a pixel by pixel variation in the noise properties. We will model both of these contributions through the use of simulations, before applying the approach to real data.

To examine these effects, we first produced a series of full sky shear and convergence maps using the `healpy` routine `synfast`. This routine produces Gaussian random fields from an input power spectrum, which for these tests was that of a flat ΛCDM Universe characterised by the parameters $\Omega_m = 0.3, \Omega_b = 0.047, h = 0.7, \sigma_8 = 0.82, w = -1$. This power spectrum was found using `COSMOSIS` (Zuntz et al., 2015) which utilises the `CAMB` code (Lewis & Bridle, 2002b). A 'true' sky convergence distribution is given by the output of this routine, with matching true shears. We fit to 25 different true skies with different noise fields, drawn from the same map of pixel uncertainties matching the Buzzard footprint, another simulation effort introduced later. We use this footprint so that results from this initial, simple simulation set up can be compared with more realistic cosmological simulations. These uncertainties are calculated for a shear field with an error on γ components of ≈ 0.27 and galaxy number in each pixel obtained from the Buzzard catalogue (mean pixel galaxy count of ≈ 600). Noise in this case means a realisation drawn according to an error field, and each is independently drawn from the distribution. Therefore, each of the 25 maps is of both a different true convergence field and with a different noise contribution in each pixel.

The forward fitting approach was applied to these simulated maps and produced converged fits. Maps were also made by the direct inversion, in order to compare the two approaches.

Fidelity metrics

Figure 3.3 shows how well the F statistics behave for these simulations, with the filled region showing the Gaussian field 1-σ spread of results when these are evaluated across the 25 maps. The F_1 statistic has been de-noised in this plot and is found to be consistent with 1; this implies that our method of modelling noise is consistent with the true noise within that pixel. For the

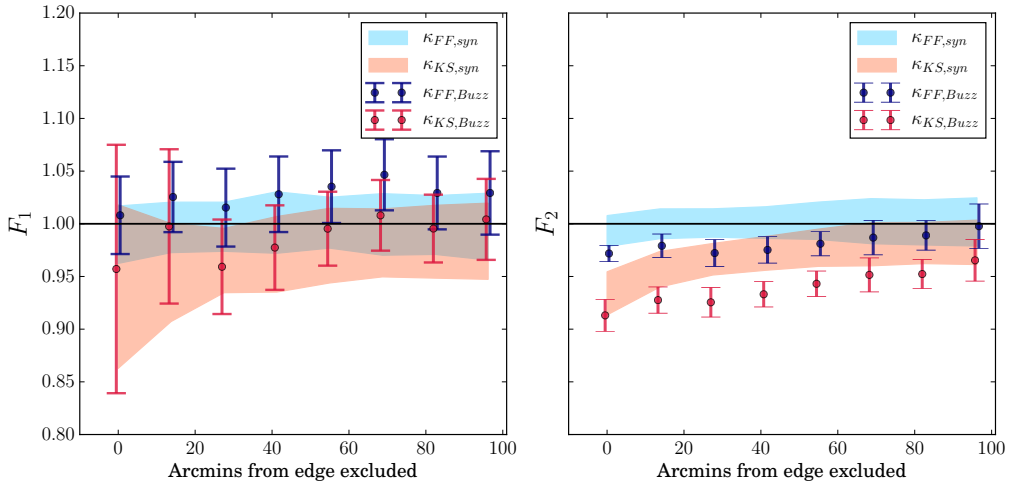

Figure 3.3: The F statistics for the two reconstruction methods in multiple simulation tests. The solid filled regions are for the Gaussian simulations with known noise properties, and the scatter points are for the Buzzard simulations. The horizontal axis represents the width of the pixel range around the edge of the surveyed area which is removed before calculating F for the remaining areas of the footprint. Noise estimates for the Buzzard simulations were found by using the residuals from a fitted sky and a known, Gaussian simulated truth using `synfast`. The F_1 statistic has been de-noised, but the F_2 statistic does not require this procedure.

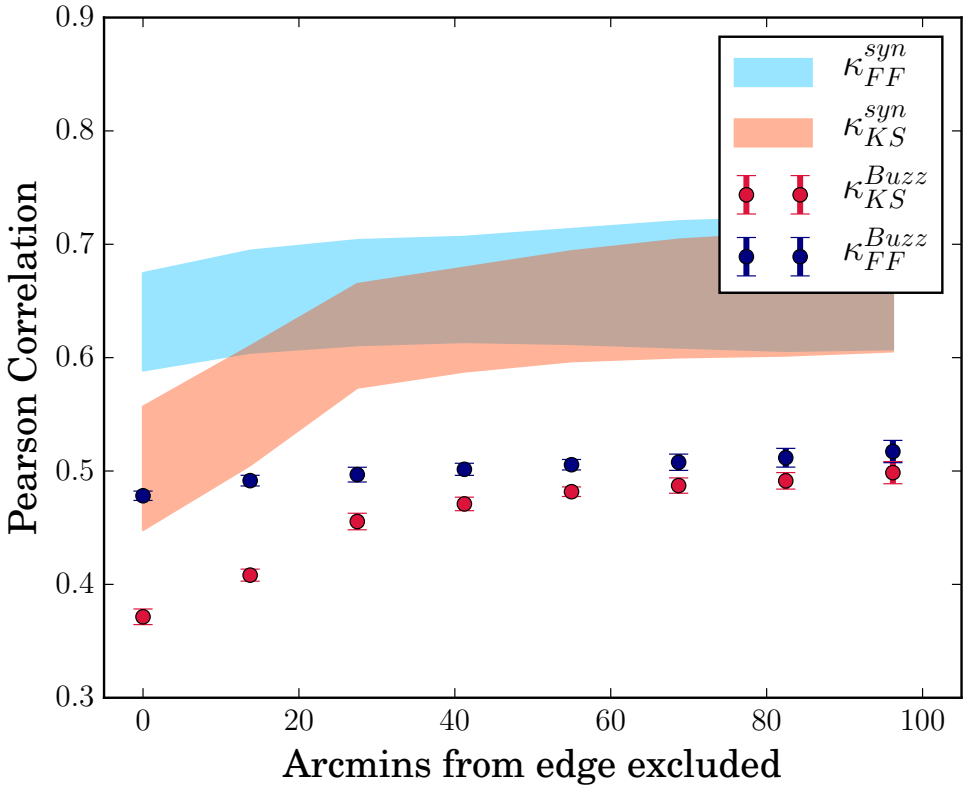

Figure 3.4: The Pearson correlation coefficient between the different reconstruction techniques and the true convergence κ_t, excluding pixels that fall within a given distance of the edge of the survey. The results for both the simulations using `synfast` (filled region) and those using the Buzzard simulation are shown. The deterioration of the reconstructions as the edge pixels are included in the measurement of the statistic can be interpreted as the contribution from these more noisy pixels reducing the correlation. Significant improvement in correlation can be seen as the noisier exterior pixels for κ_{KS} are excluded, but for κ_{FF} the variation due to excluding these pixels is much less pronounced.

Kaiser-Squires technique applied to the data, the large errors in these outer pixels cause more scatter in the denoised statistic.

Considering the F_2 statistic, we see the direct inversion clearly differs from unity, with the reconstruction becoming worse nearer to the edges. By contrast, the forward fitted map consistently preserves the phase information significantly better across the survey area. This can also be seen in the Pearson correlation coefficient in Figure 3.4, where the edge effects mean that the coefficient for the direct inversion is ≈ 0.1 lower when evaluated over the 22830 pixels in the footprint.

3.2.2 Quantifying noise

The Gaussian maps described in Section 3.2.1 were also used to estimate the uncertainties on each pixel of the final convergence maps for simulated and real data. This is because measuring the variance within a pixel serves as an unreliable estimate of the true noise field, and we instead choose to calibrate with simulations of known convergence. The calibration of noise fields for the forward fitting mass maps is discussed further in Appendix A.

We estimate the error in a pixel by simulating many Gaussian maps and measuring the difference between the fitted maps and a known truth. Many such difference maps give a sampling of the error distribution in each pixel, with the standard deviation of residuals in a pixel across these mock maps used as the pixel uncertainty estimate. These simulations use the appropriate shear errors in each pixel for the data we are attempting to simulate, i.e the shape noise field. We use 25 simulations of noisy skies to produce our errors, and errors for the direct inversion were found using the same maps. This approach was used to calculate errors for all simulation tests and on the Y1 data. When referring to the forward fitted results, 'error' refers to the standard deviation of the residuals found in this way, and 'noise' refers to a single map realisation with values drawn from this distribution for each pixel.

3.2.3 Galaxy survey simulations

Further to the Gaussian simulations, we also test the reconstructions using the Buzzard simulations (DeRose et al., 2019), specifically the "Buzzard v1.3" mock galaxy catalogues. These catalogues are for 6 simulations resembling the DES Y1 data set, with accompanying galaxy shears, ellipticities and κ.

These were produced through N-body simulations consisting of only dark matter, in a flat ΛCDM Universe, through the use of `LGadget-2` (Springel, 2005b) with initial conditions from `2LPTIC` (Crocce et al., 2006) and CAMB (Lewis & Bridle, 2002b). Three boxes sized 1050^3 , 2600^3 and 4000^3 Mpc^3h^{-3} were run using 1400^3, 2048^3 and 2048^3 particles respectively, assuming a background cosmology of $\Omega_m = 0.286$, $\Omega_b = 0.047$, $\sigma_8 = 0.82$, $h = 0.7$, $n_s = 0.96$ and $w = -1$. The coarser simulations were used to produce sufficient volume for DES, and the higher resolution output was used to tune smaller scale modelling. It is worth noting that all of these parameters are consistent with the results found in the DES Y1 3x2-pt results (Abbott et al., 2018) even though perfect modelling of cosmological parameters is not necessary to test the mass reconstruction; the previous Gaussian simulations were sufficient for testing the reconstruction pipeline only, but using the Buzzard simulation allows us to investigate how further observational effects will influence the performance.

Using the outputs of the dark matter simulations, the empirical `ADDGALS` algorithm (DeRose et al., 2019) populated the haloes with galaxies, replicating results found with subhalo abundance matching (SHAM) (Conroy et al., 2006; Reddick et al., 2013) by fitting a model to a smaller, higher resolution simulation and applying this model to the larger simulation. `ADDGALS` simultaneously fits both the distribution of galaxy over-densities and the distribution of r-band absolute magnitudes of galaxies, through matching a luminosity function to observed galaxy counts. These galaxies are further provided with full SEDs from SDSS DR6 (Adelman-McCarthy et al., 2008) to produce the $grizY$ magnitudes.

Lensing parameters are also computed for the catalogues, in the form of γ

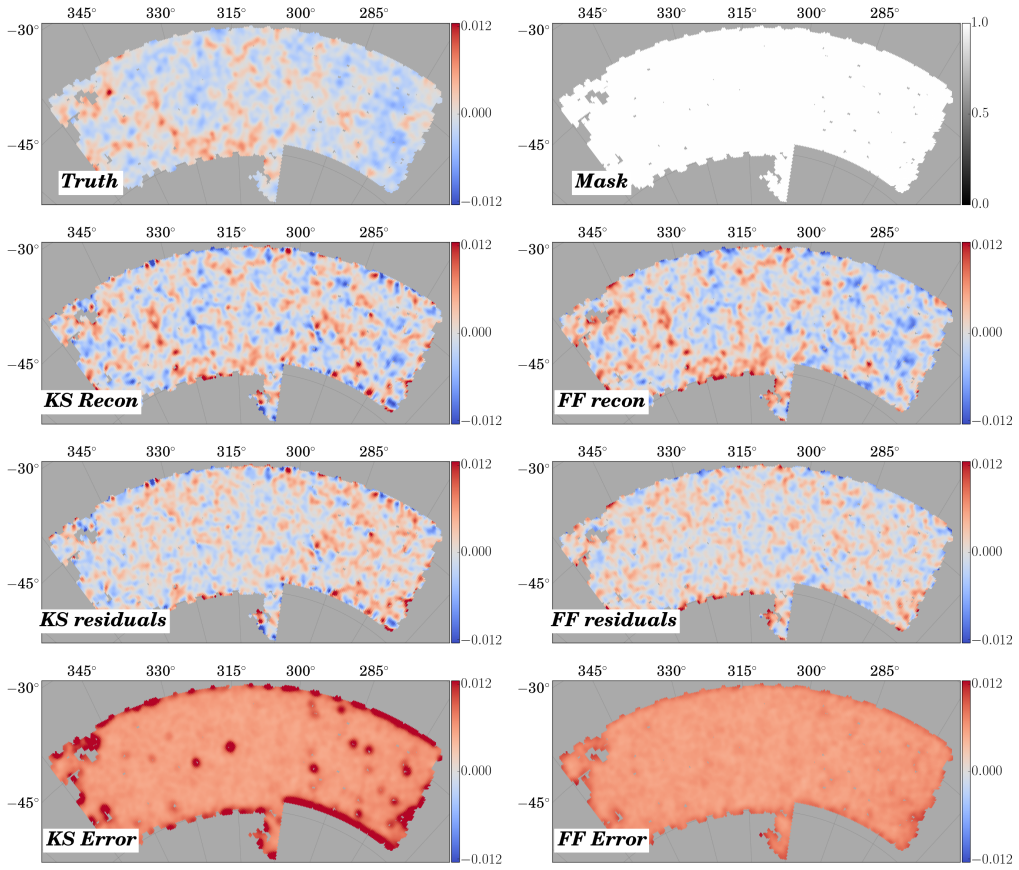

Figure 3.5: Reconstructions of the convergence field for the Buzzard simulation for both the direct inversion (left column) and the fitting method (right column). Smaller errors are present in the edge pixels of the fitted map. The fitting method also has a much more uniform residual map inside the footprint, whereas the direct inversion has a large portion of the survey with slightly larger residuals. Furthermore, when measuring the χ^2 between each field and the truth, we find that the direct inversion has a result of 26697, whereas the forward fitted map has a χ^2 of 25795, when both are evaluated over 22830 pixels.

and κ for each galaxy. This is done through the use of the multiple plane ray tracing algorithm Curved-sky-grAvitational Lensing for Cosmological Light conE simulatioNS (CALCLENS; (Becker, 2013)). The routine uses projected density fields to produce weak lensing maps, with a resolution of 6.4 arcsec. The effects of adding photometric noise, adding shape noise, and imposing cuts similar to those in the data catalogue, as described in Section 3.1.1, are also accounted for to produce an output similar to that of DESY1. The simulated region is smaller than the full DES Y1 observed region by ≈ 600 degrees, and its galaxy density count is lower by $\simeq$20%.

We apply the forward fitting method to the Buzzard data and output a final map, which is an average of many fitted maps consistent with the data. We estimate the pixel error distributions through further simulated `synfast`(Górski et al., 2005) skies using the same footprint as the Buzzard map, and examine the residuals across an ensemble of final fitted maps and the true κ map in each case. These simulations serve as a simple model of the lensed Universe that we are observing: a uniform source plane of galaxies which undergo a lensing effect, onto which a shape noise component is added. In reality, the broad redshift bins that we use to produce sufficiently large galaxy counts on the source plane mean that this model is a simplification, but we will see that it provides a sufficient estimate of errors for our purposes.

The maps produced for the Buzzard simulation are shown in Figure 3.5 and the residuals for the forward fitting method can be seen to be much lower in the outer edge regions, similarly to that found for the Gaussian simulations, although the errors are now slightly larger. This may be due to non-Gaussianities in κ_t, or due to the extra noise inherent in all of the Buzzard simulated maps, where we do not have an exact value for the true κ and shear in a pixel but instead estimate it from the measured quantities for galaxies within that pixel.

F statistics

The F statistics for Buzzard can be seen plotted as the scatter points on Figure 3.3. In the case of F_1, the de-noised statistic can be seen to be consistent with that found for the Gaussian maps, meaning that our estimate of the noise for these Buzzard simulations is reliable. For F_2 both techniques appear to behave slightly worse than in the previous simulations, due to additional noise in Buzzard. The slightly lower F_2 and slightly high F_1 indicate that this map is one with greater residuals than the typical map found for the Gaussian maps, but still consistent with our expectations.

Pearson correlation

The Pearson correlation coefficient measurements can be seen in Figure 3.4 for both reconstructions and for both methods of simulating the data. The `synfast` simulations have a higher coefficient for both techniques, and each simulation shows a similar shape when comparing the same reconstruction methods. It is apparent that the statistics found for the fitted maps are significantly less affected by removing outer pixels than the direct inversion, suggesting the presence of excess noise in the edge pixels of the direct inversion.

3.2.4 Moments

Summary statistics such as moments can be very useful probes to test the accuracy of our final maps. Beyond characterising the distribution, the moments as a function of the smoothing scale have also been shown to be useful for constraining the underlying cosmology(Gatti et al., 2019).

When measuring these moments, we are measuring a combination of the true convergence moment and a noise term. We correct for the noise following the technique used in Van Waerbeke et al. (2013), and the methodology introduced in equation 3.4 such that for the second moment the de-noising

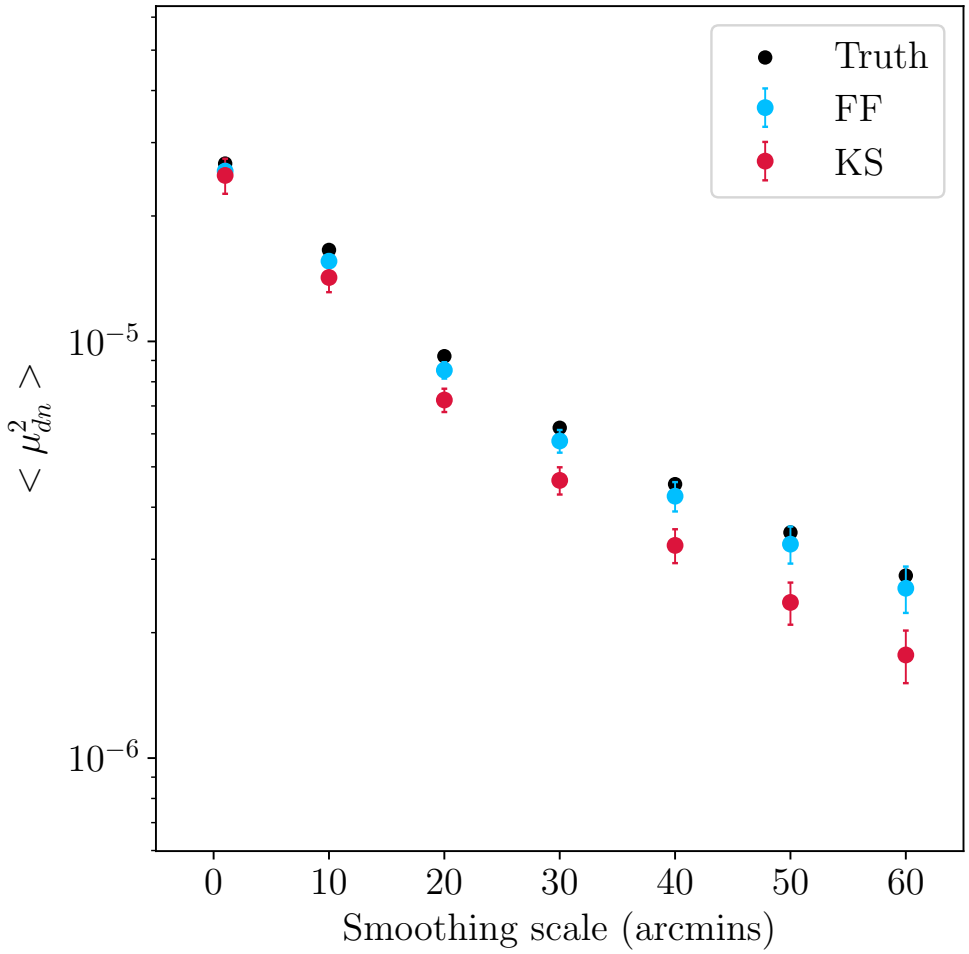

Figure 3.6: Reconstruction of the second moment of the κ field from Equation 3.9 for the forward fitting method and the truth for a Buzzard simulation.

procedure is:

$$\langle(\mu_{dn})^2\rangle = \langle(\mu_N)^2\rangle - \langle(\mu_n)^2\rangle, \tag{3.9}$$

where μ_n is the κ field found for the noise exclusively, μ_{dn} is the denoised κ, and μ_N is the moment found from the noisy field.

Figure 3.6 shows the reconstruction of these de-noised moments for both methodologies on one of the Buzzard simulations. At large smoothing scales, the edge effects from the direct inversion become more and more significant such that the moments become increasingly biased away from the truth. The forward fitting approach does not have this level of significant error localised around the edge of the map, so it can reconstruct the moment more reliably to higher smoothing scales. At higher pixel resolution, these edge effects will become less significant as edge pixels account for a smaller fraction of the total pixel count.

3.2.5 PDF

The PDFs of the convergence distributions serve as a further probe of the reconstruction, and these are shown in Figure 3.7. The large contribution of the noise added to the data can be seen to cause the final PDF to differ significantly from the underlying, non-Gaussian true κ PDF. The PDF of our estimated noise distribution is also shown, as well as the PDF of the exact differences between the reconstructions and the truth. These estimates of the noise and the true residuals can be seen to be in good agreement, indicating a good understanding of the noise properties of both methods. Further, the PDF of the κ distribution in the forward fitting method manages to retain more of the non-Gaussian shape and does not find an excess of high κ values in edge pixels. The forward fitting method finds fewer of the large, negative convergence values which are induced by the noise but reconstructs a similar number of higher positive κ peaks to the direct inversion. Some over-dense regions will be real density contrasts, for which both techniques should agree, and some will be the large edge effects that are only present in the direct inversion.

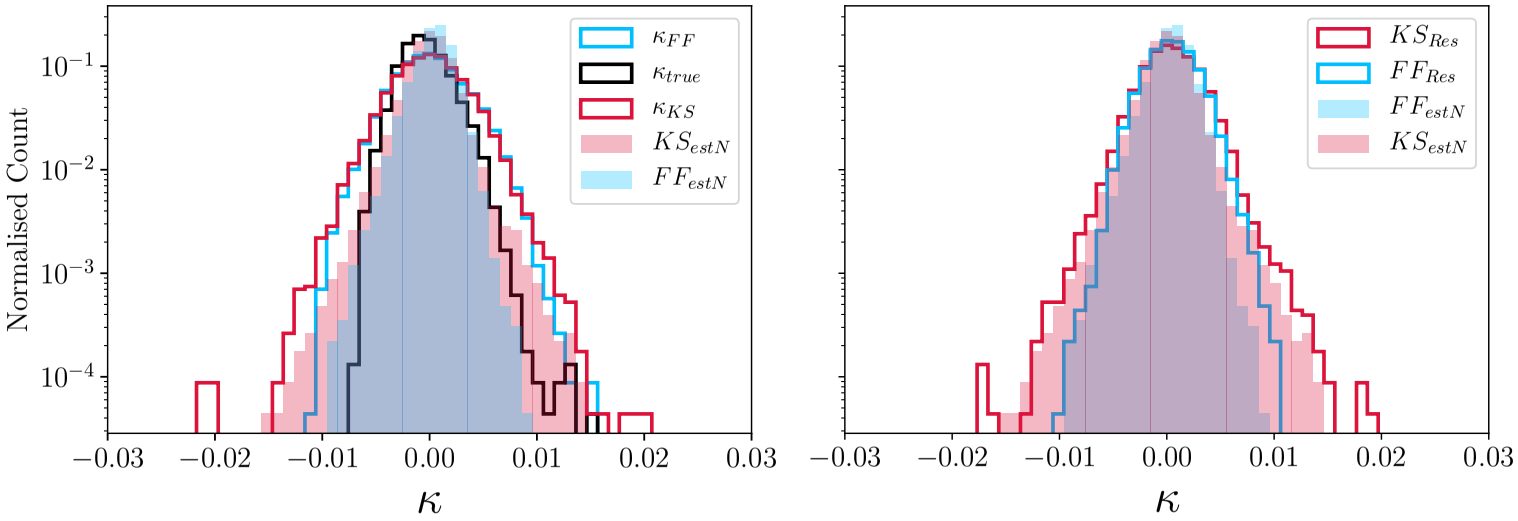

Figure 3.7: PDFs of the reconstruction techniques' convergence fields compared to the true distribution for the smoothed Buzzard simulation shown in Figure 3.5. The left panel shows the distribution of the κ in pixels (solid lines), together with the estimated noise distribution (filled region). The solid black line is the true PDF that both reconstructions are attempting to recover. The right panel examines the reliability of the estimates used for the noise distribution, with solid fill areas denoting the true residuals and the solid lines denoting the noise estimates used in the left panel.

We also examine the agreement of these two distributions using the Jensen-Shannon divergence D_{JS} (Shannon, 1948), a quantity designed for such a comparison in an information theory context. This is defined, for two distributions A(x) and B(x) as

$$D_{JS}(A, B) = \frac{1}{2}(D_{KL}(A||M) + D_{KL}(B||M)), \tag{3.10}$$

where

$$M = \frac{1}{2}(A + B), \tag{3.11}$$

and D_{KL} is the Kullback Leibler divergence (Kullback & Leibler, 1951), defined for discrete bins as

$$D_{KL}(A||B) = \sum_x A(x) \log \frac{A(x)}{B(x)} \tag{3.12}$$

We work in logarithms of base 2, which means that the Jensen-Shannon divergence can be in the range $0 - 1$, with 0 indicating identical distributions and 1 meaning completely different distributions. This provides a way to quantify the similarity between the PDFs of each reconstruction and the known, true κ PDF. In the unsmoothed κ fields, we find that for the direct inversion $D_{JS} = 0.349$, whereas for the forward fitted map $D_{JS} = 0.308$. In the smoothed maps shown in Figure 3.5, the result for the direct inversion is $D_{JS} = 0.115$, compared to $D_{JS} = 0.103$ for the forward fitted maps. These values show that whilst both methods are finding somewhat similar distributions to the desired, true PDF, the forward fitted maps are performing slightly better. We can interpret this result as showing that the forward fitted map having a reduced noise component. From inspection of the PDFs, it can be seen that this is indeed the case in the tails of the distribution, where the difference between the desired true distribution and the reconstructed one are markedly different.

3.2.6 Minkowski functionals

Figure 3.8 shows the functionals reconstructed for the Buzzard simulation. The solid black line shows the functionals for the κ_t field, and the yellow

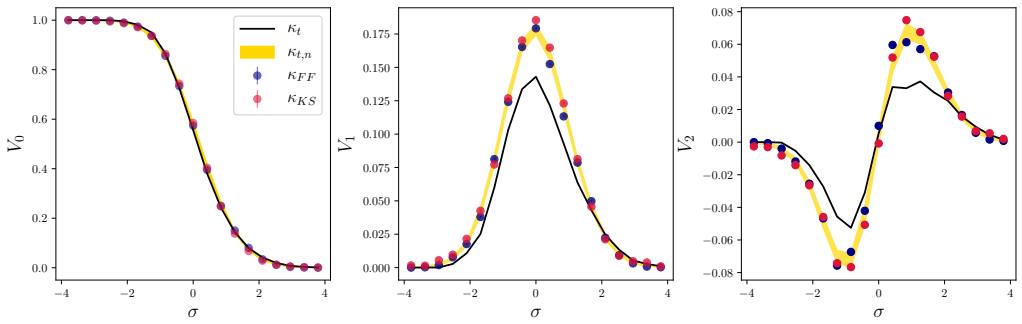

Figure 3.8: The Minkowski functionals for a Buzzard simulation used to test the κ map reconstructions, as a function of excursion. In this case, σ indicates the number of standard deviations of the final κ map and not the error in a pixel. The black line shows the functionals for the true κ field and the yellow field region shows the 68% confidence region for functionals expected when a simple noise field is added to this. The Minkowski functionals measure the topology of the maps and perfect agreement between truth and reconstruction across all 3 statistics would mean that all topological information is being retained by the reconstruction.

region shows those that we would expect to construct for this field in the presence of noise. The deviations between the functionals for κ_t and those in the presence of noise are greatest within 1 standard deviation of the mean, which coincides with the noise level of these maps. This is expected, as the noise adds artificial peaks at this scale which will change the functionals. The Gaussian noise means that these maps have a similar shape, but reducing the noise level in these maps would make it easier to distinguish between cosmologies as less information would be lost to the noise. Particularly in the direct inversion, the edge effects will introduce some large κ values into the distribution and this will alter the standard deviation of the map and consequentially bias the functional measurement. These results also show that when we attempt to constrain cosmology with these measurements, the reconstruction technique used needs to be taken into account and adequately modelled.

The significance of this agreement was calculated through the use of χ^2, in the form:

$$\chi^2 = (d-t)\mathrm{Cov}^{-1}(d-t)^T, \tag{3.13}$$

where d is the vector of functionals calculated for a reconstruction, t is the vector of functionals for the true κ field and Cov is the covariance matrix calculated by examining the covariance between these functional bins when noise is added to the true κ. This noise is created by generating maps of ellipticity noise, i.e for a pixel i, noise is found by randomly sampling from a Gaussian with width according to the error on shear in that pixel, σ_i. For empty regions of the sky, we fill these areas with noise with the average shear standard deviation of the observed region. These shear maps are then used to produce full sky κ maps through the direct inversion. Edge effects are absent from these maps, as the γ noise fields are on the full sky, and as such provide a best case scenario for the noise on our final κ maps. We are only considering shape noise in our covariance, although we expect other contributions to be sub-dominant. A complete approach would model the whole mass mapping pipeline and account for the contribution to the covariance from cosmological

structure. In chapter 4, we develop more accurate covariance matrices. Initial tests using Gaussian simulated fields supported the assumption of a shape noise dominated covariance matrix, and they are sufficient for this initial exploratory analysis.

For binning functionals into n bins, we produce $4n$ of these noise maps. Each noise is then added to the true κ_t field and the functionals for each bin are calculated. We use this ensemble of functionals to measure covariances between bins for our χ^2 calculation, through repeatedly producing new noisy versions of κ_t fields.

This approach gives us a way to compare both techniques' abilities to reconstruct the functionals, relative to the best that can be done with the level of noise in the data. It is therefore important to understand the behaviour of the reconstruction method used, for the prospect of measuring cosmological parameters with functionals. For the Buzzard simulation results shown in Figure 3.8, the reduced χ^2 results for (v_0, v_1, v_2) give $(93/25, 99/25, 54/25)$ for the direct inversion and $(40/25, 38/25, 38/25)$ for the forward fitting routine. This stark contrast shows the significant effect that edge effects can have on final results and that accommodating for this in cosmological analyses of the functionals is important, as it can bias the final result. The edge effects in the direct inversion add an additional noise component which is not accounted for in the covariance matrix, which is an idealised noise scenario. In Chapter 4, I will expand on this work to produce sufficiently accurate covariance matrices for cosmological inference.

3.2.7 Comparing residuals

The two reconstruction techniques produce different κ maps for the same data, so an interesting comparison is to examine the regions in which they disagree and see what can be learned in these areas. We examine the differences between two maps in ratio to the error in each map in Figure 3.9. Firstly, by visual inspection, the κ_{KS} map can be seen to be in much more significant disagreement with the κ_{FF} map when differences are taken in

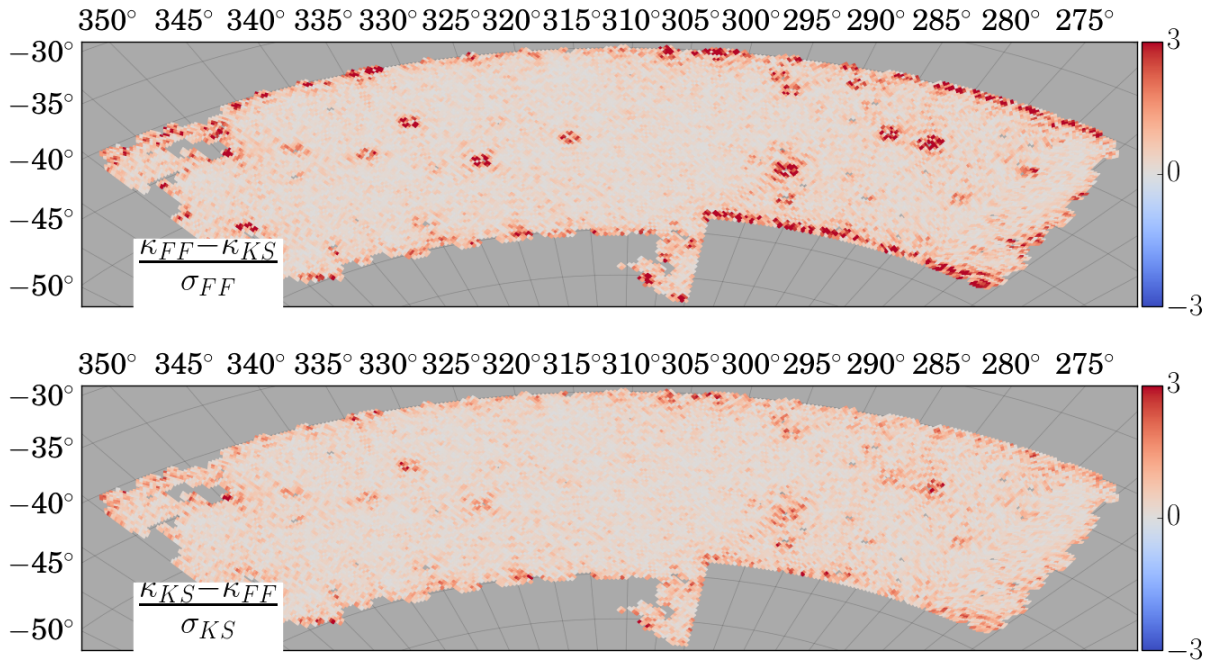

Figure 3.9: The difference between κ maps found for both reconstruction techniques applied to one of the Buzzard simulations. As each map technique has different errors in each pixel, the level of tension in terms of standard deviations in a pixel depends upon which map is used as a reference. Disagreements between the direct inversion and the forward fit around the survey edge are of larger significance in terms of σ_{FF}, indicating that the forward fit is highlighting these particular pixels in the Kaiser-Squires map as being due to edge effects and not caused by the shear signal in the observed region.

terms of σ_{FF} than σ_{KS}. This inconsistency is another illustration of the noise introduced by the Kaiser Squires technique when directly applied to the data. Further to this, considering the signal to noise of these differences in each pixel can highlight tensions between the maps. The two methods are in agreement across large areas of the centre of the footprint, but the edge effects present in the direct inversion κ_{KS} map mean that there is a tension with the forward fitted map. In the 750 pixels where there is a disagreement of $2\sigma_{FF}$ or more, the forwards fitting method has a smaller residual with κ_t than the direct inversion in 81% of pixels.

Power spectra of residuals

The power spectrum of the residuals for each method give an interesting insight to how the approaches perform across a range of scales. Figures 3.10 and 3.11 show the power spectra for the residuals for both mass mapping methods, on the unsmoothed and smoothed Buzzard maps respectively. The smoothing is of the same scale as that used in the rest of this chapter, using a Gaussian with a standard deviation of 20 arcmin. In the unsmoothed case, the residuals for the forward fitting approach can be seen to be significantly smaller than those for the direct inversion across a range of small scales, above $\ell \approx 100$. At intermediate scales, the approaches are quite similar, but at the lower ℓ modes the forward fitting appears to be performing better, where the modes are less well constrained by the data and the mask will cause a significant signal. When the maps are smoothed, the difference between the two are reduced but the forward fitting map still has lower power in the residuals spectrum from $\ell \approx 100$. The smoothing is of too small a scale to change the power of the residuals at intermediate and large scales, but acts to reduce them at small scales.

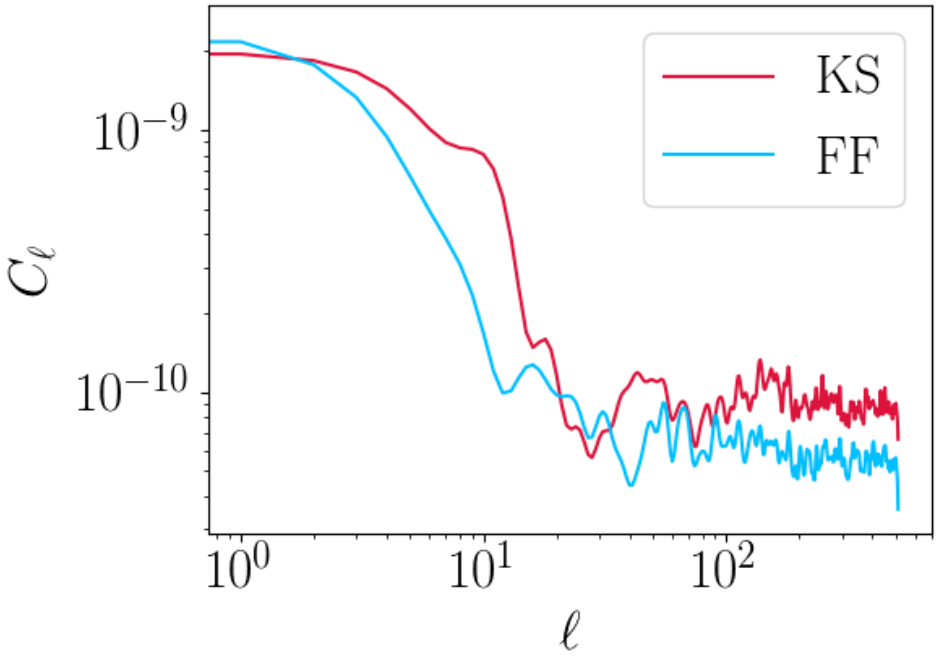

Figure 3.10: The power spectrum of the residuals for each mass reconstruction methods, without smoothing the maps.

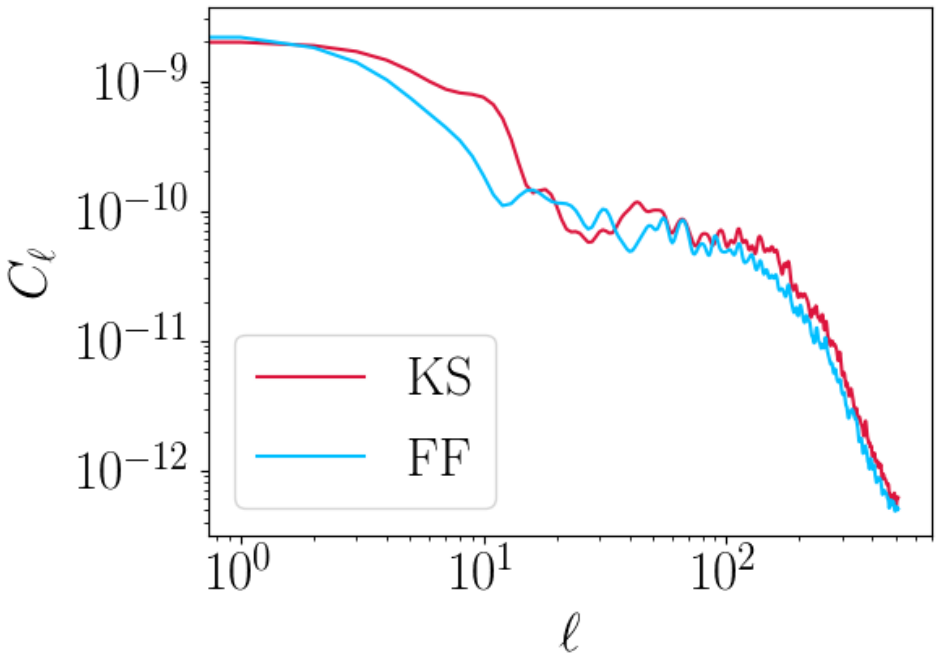

Figure 3.11: The power spectrum for the residuals found for the smoothed maps for both methods on the Buzzard simulation.

3.3 DES Y1 data

3.3.1 The DES Y1 fitted maps

The fitted maps for the DES Y1 data are shown in Figure 3.12 for the forwards fitting and the Kaiser Squires methods, applied to the full area of the `MetaCalibration` catalogue. The maps presented here are for the redshift range $0.2 < z < 1.3$, which gives the least noisy shear measurements (Chang et al., 2018). These maps are visually very similar in the inner regions of the map, where peaks in one map frequently coincide with peaks in the other map. The edge effects are apparent in the reconstruction of the direct inversion in the area of complicated masking (below 5 deg in right ascension) whereas such high κ pixels are not produced in the fitted version of the map. This behaviour is similar to that seen in the previous simulation tests.

Figure 3.13 shows residuals between the reconstructions, which is a particularly interesting comparison to perform on the data as it will indicate regions where we think the forward fitting routine will be able to improve on our knowledge of the mass distribution in the Universe. The direct inversion performs well for κ reconstructions well inside the survey footprint, and we see that both methods are working in a similar way in this area as they were in the simulations. In the outer pixels, the differences are typical of those that we would expect from the edge effects, where large κ noises and biases are introduced. The smaller errors of the fitting routine in these edge pixels means that these noisy pixels in the direct inversion are in tension with the fitted results. In more complicated regions of the mask, there are more frequent disagreements between the two methods, and our simulation tests implying that the forwards fitting method is more suited to these areas. Even in the centre of the mask, a small defect or hole can introduce large errors in the direct inversion map, which the forward fitting map does not suffer from. In areas of highly complex masking, such as around 0 to -15deg, both routines struggle but the forward fitting routine appears to introduce much less noise than the direct inversion.

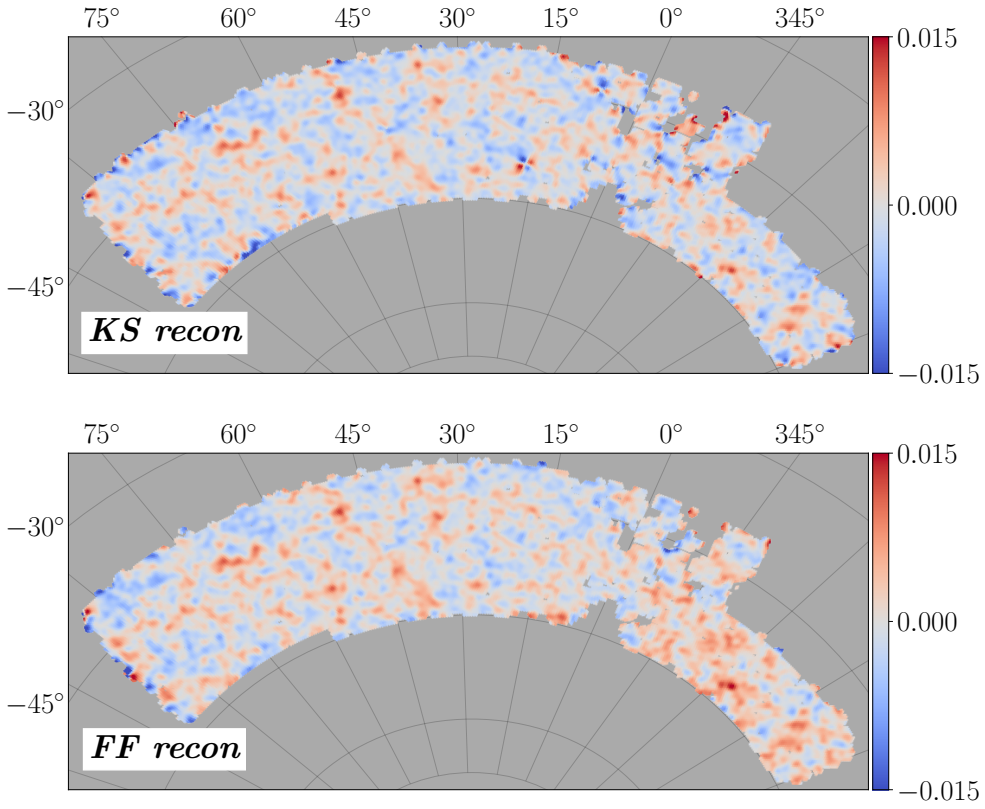

Figure 3.12: The final fitted maps for the DES Y1 data for both the direct inversion and the forward fitting method, using `nside`= 256. The area of complicated masking at right ascension < 5 deg was not used in our previous wide field mass map thesis due to the footprint introducing significant edge effects.

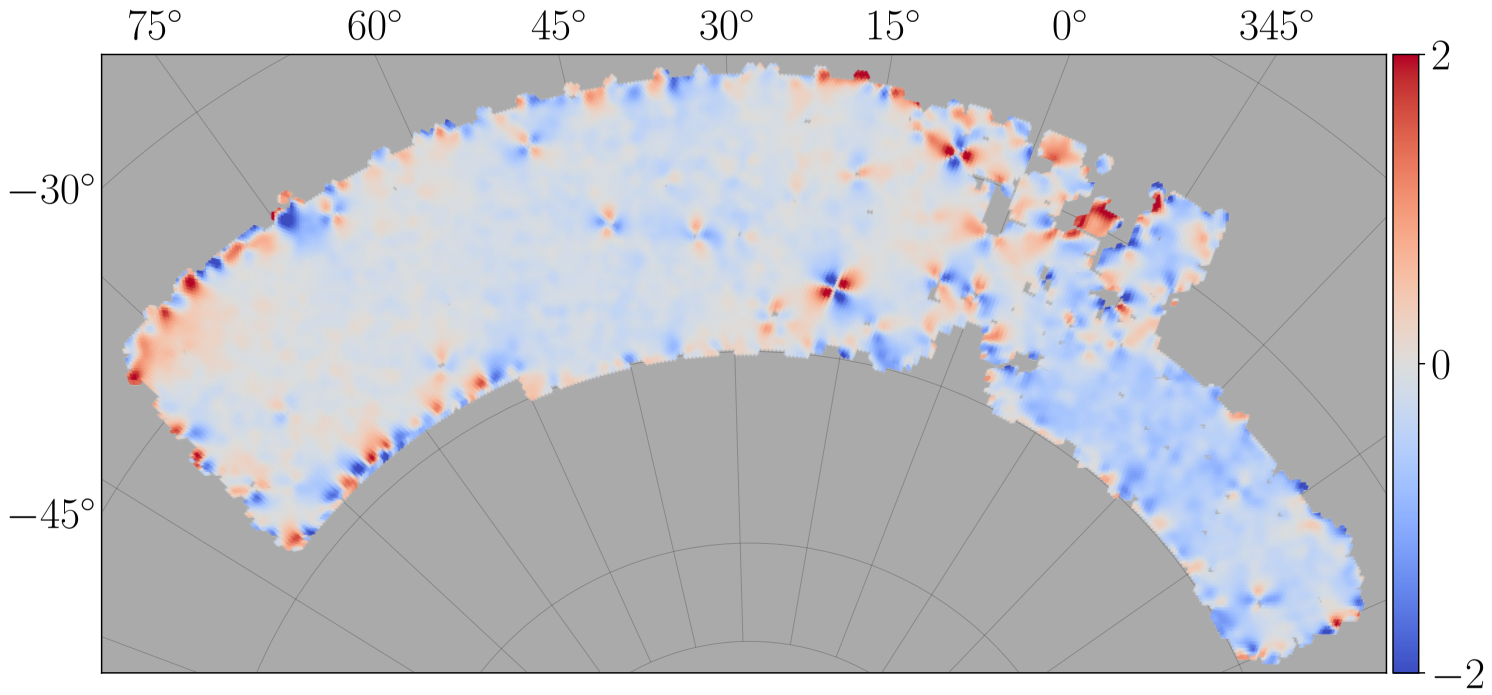

Figure 3.13: The residuals between the two reconstruction techniques, scaled in terms of the error on the forward fitting method in each pixel, and smoothed with a Gaussian of $\sigma = 20$ arcmin. As expected, the most significant differences arise in the areas around the edges and in areas of complicated masking.

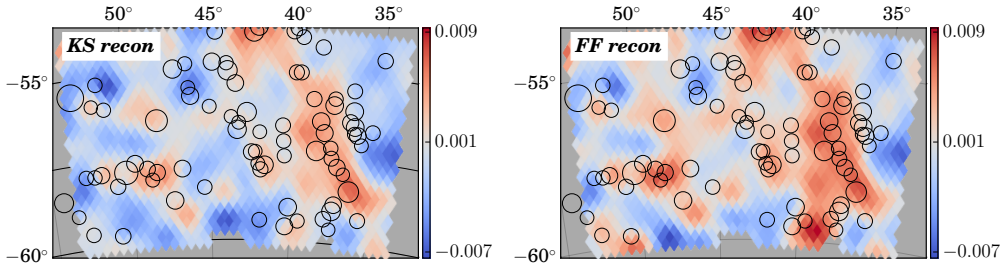

Figure 3.14: A section of the reconstructed maps, with `RedMaPPer` clusters plotted in black circles, with a radius scaling as the cluster richness λ, which is an indicator of cluster mass. Clusters were selected in the redshift range $0.1 < z < 0.4$.

Figure 3.14 shows an area of both reconstructed fields with `RedMaPPer` clusters (Rykoff et al., 2016) plotted on top. This region is on the southern edge of the survey area. Both maps produce fields of similar morphology, but the forward fitted map has higher peaks due to lacking the edge biases introduced by the direct inversion. Some clusters follow the structure picked out by the maps, with areas of over-density being more frequently populated by clusters.

3.3.2 Systematics

It is important to correlate these maps with other quantities that are expected to be uncorrelated with the shear in a pixel, to test whether our measurements are free from systematic effects. A significant correlation between our maps and another quantity would indicate how we are not solely inferring mass associated with weak lensing shear, but have a signal contaminated by another source.

We will examine the correlation between the observed shear measurements and other observed quantities which could plausibly cause systematic effects, such as the PSF, the airmass, the sky noise and background, across the *griz* filters. Using maps M^s of these observed parameters (Leistedt et al.,

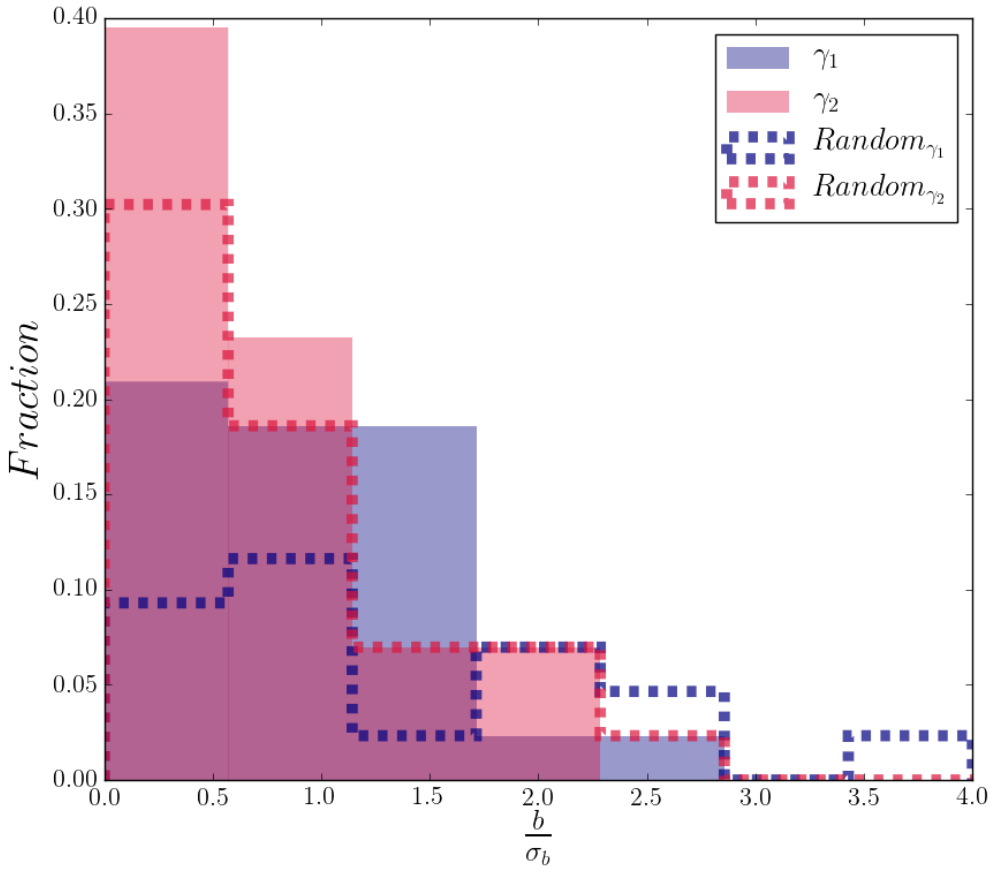

Figure 3.15: The distribution of the magnitude of systematics correlations found for both the Y1 data and for random maps generated using the Buzzard simulations. The latter give an indication of the level of correlation that can arise from random, uncorrelated maps, and therefore give an estimate of an acceptable level of correlation to be found with the Y1 maps.

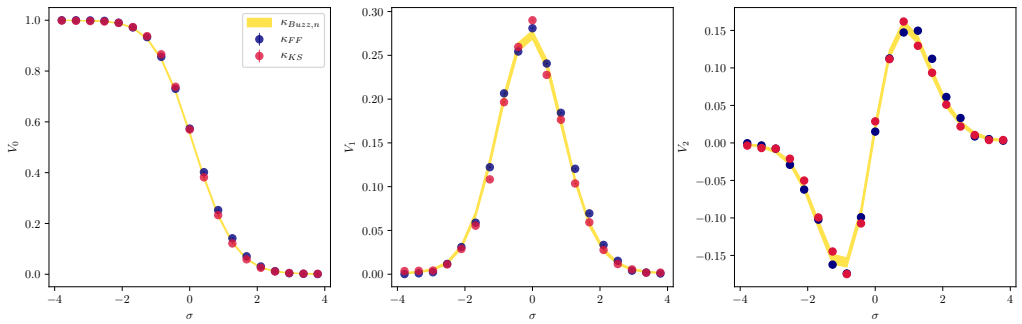

Figure 3.16: The Minkowski functionals for DES Y1 mass maps, found through both the direct inversion and the forward fitting approach. The solid yellow region shows the expected functionals for a Buzzard field with DESY1-like noise.

2016), we follow the approach used in Chang et al. (2018). Each pixel in the map is assigned a value n between 1 and 10, determined by which decile in the range for that systematic that it belongs to. We then take the average shear value of all pixels of a given n, $\hat{\gamma}_n$. A first degree polynomial is fitted between n and $\hat{\gamma}_n$, with y intercept a and gradient b. The gradient found in this way will therefore indicate a correlation between the shear estimate and the systematic, and a lack of correlation will be indicated by a gradient consistent with 0. Errors on the gradient are found by jackknife resampling.

Figure 3.15 shows the extent of these correlations found for the Y1 data; we see that the correlation between the Y1 data and systematics is no stronger than that found between the systematics maps and a completely uncorrelated map (the Buzzard map).

3.3.3 DES Y1 Minkowski functionals

Following the examination of whether the two reconstruction methods can produce reliable Minkowski functionals in Section 3.2.6, we can also examine the functionals that describe our final Y1 mass maps. We measure V_0, V_1 and V_2 (using the algorithm described later in 4.1.1) for the final Y1 convergence

maps shown in Figure 3.12. We present these measurements in Figure 3.16, also showing the measurements and uncertainties found for these quantities in the Buzzard simulation.

As we are only comparing one particular realisation of the Buzzard simulations with the Y1 results, we cannot infer cosmological information from this plot, as we don't know how representative the (finite footprint) Buzzard measurements are of the functionals expected for the Buzzard cosmology, or indeed of the real Universe. However, we see that observed Y1 Minkowski functionals appear similar to those in Buzzard. We will engage in a cosmological analysis of these results in the next chapter, where noise will require careful treatment depending on the method used (i.e. direct inversion or fitting), as shown in our earlier analysis in Section 3.2.6.

3.3.4 Reproducible research

Much modern research uses code and/or data which is never publicly accessible, meaning that the scientific ideal of reproducible and independently verifiable results is frequently difficult. Fortunately, in fields which make extensive use of computer simulation or calculation, replication of results should be possible by running the same code on the same data. Code repositories such as Github can improve this problem, and it is best practice to share the data and code used for scientific analyses. To this end, the codes used to achieve the results in this chapter will be uploaded to the a repository located at `https://github.com/bibblybobbly/ffk`. All parameters necessary to use the codes are described in this chapter, and catalogues of DES data are available at `https://www.darkenergysurvey.org/the-des-project/data-access/`. In practice, as the forward fitting routine makes use of random perturbations to explore the likelihood surface, there is no way of ensuring the same maps will be output by any given run of the routine, so the final averaged map for both the Buzzard simulation and the Y1 data will be uploaded to the repository so that accuracy metrics can be independently calculated and verified. Future cosmology surveys will require

increasingly large computing power and there is the potential issue that the pipelines used to produce cosmological constraints could become increasingly inaccessible. It is therefore encouraging that surveys such as DES and KiDS have been publishing their data.

Chapter 4

Cosmological constraints from mass maps

The motivation to produce improved maps of the matter field stems from multiple origins, but a significant contribution is the potential for weak lensing mass maps to provide cosmological constraints. These maps provide the potential to improve weak lensing studies by including information beyond 2-point analyses, and will be important in current and upcoming surveys. In the following section we will focus on Minkowski functionals, which have been used with weak lensing mass maps with promising results (Mecke et al., 1994b; Schmalzing et al., 1996; Kerscher et al., 1996). We will explore how the currently possible direct inversion mass maps can lead to cosmological constraints.

4.1 Cosmology with topology

As introduced in the previous chapter, Minkowski functionals are descriptors which can entirely encode the topological information of a space, where a N-dimensional space has $N + 1$ Minkowski functionals. They do this by measuring descriptive statistics across the surface, considering regions which have values above a given excursion threshold. In this case, we will be con-

sidering a 2D projected convergence field, meaning that there are 3 functionals ν_0, ν_1, ν_2 which can be associated with the surface area, perimeter and curvature. For a Gaussian field, they are exactly defined with knowledge of the power spectrum (Munshi et al., 2012), but this is not the case for non-Gaussian fields. The maps of such a non-Gaussian field will possess information that is ignored in a two-point analysis, so extracting it will naturally lead to improving constraints on cosmological parameters. However, they are not analytically predictable so require simulations to measure the functionals in a given cosmology. This means that inference using functionals requires generation of a power spectrum for the early Universe, a simulation package to run through to later times and produce a density field, and then a lensing pipeline to produce convergence maps from the particle positions. The resulting map will then have its functionals measured and the process is repeated for as many parameter combinations are required. This data map with unknown parameters is compared to this library of functional measurements and a likelihood calculated for between the data and the simulations. In this chapter, I will explain this process in further detail, and use the maps made with the familiar direct inversion approach to examine the potential for the functionals to improve constraints. Finally, I will apply the technique to the DES Y1 mass maps introduced in the previous chapter and combine them with other observations to improve on the constraints possible with either method alone.

4.1.1 Calculation

We introduced our methodology to calculate the Minkowski functionals in Section 3.1.4. To recap briefly, we produce maps pixelised on the sphere using `HEALPix` (Górski et al., 2005) and used an approach from Hikage et al. (2006) to measure them for discretely pixelised spaces. We defined the three functionals in our 2D space (V_0, V_1, V_2) as:

$$V_0 = \mathcal{H}(u - \nu), \tag{4.1}$$

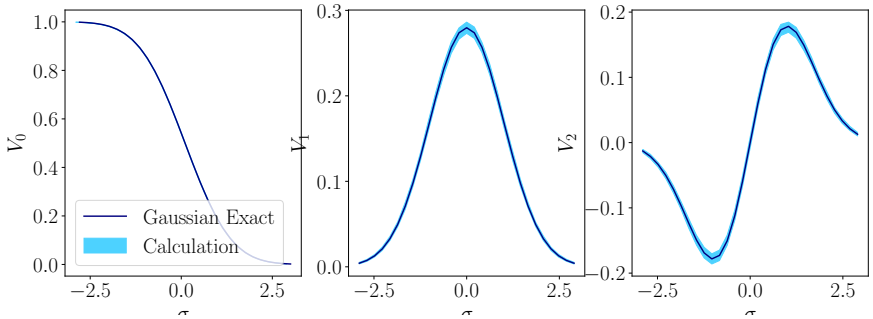

Figure 4.1: Comparing the measured Minkowski functionals for a Gaussian sky observed on a Y1 Buzzard footprint, with the solid line showing the exact predicted result and the filled region showing the standard deviation of the measurements when measured on 200 permutations. The measurement pipeline in consistent with those expected in the predictable Gaussian case, meaning that it is reliable.

$$V_1 = \frac{1}{4} F(u-\nu) \sqrt{u_{;\theta}^2 + u_{;\phi}^2}, \tag{4.2}$$

$$V_2 = \frac{1}{2\pi} F(u-\nu) \frac{2u_{;\theta}u_{;\phi}u_{;\theta\phi} - u_{;\theta}^2 u_{;\phi\phi} - u_{;\phi}^2 u_{;\theta\theta}}{u_{;\theta}^2 + u_{;\phi}^2}. \tag{4.3}$$

where a ; denotes a partial derivative, θ, ϕ are angular coordinates on the sphere, the function $F(u-\nu)$ has a value of $1/\Delta\nu$ where $\Delta\nu$ is the binning width of the thresholds of the excursion sets ν. Derivatives are calculated through taking the difference between neighbouring `HEALPix` pixels, in East-West and North-South directions.

For a Gaussian field, the Minkowski functionals can be exactly defined, which is a property that can be used to check the accuracy of the Minkowski functionals measurement routine. Figure 4.1 shows the predicted Minkowski functionals for a Gaussian field on the solid line and the range of functionals measured across 200 versions of this Gaussian distribution. The measurement pipeline is consistent with the theoretical expectation, showing that the routine is working as expected, with some small measurement errors and the finite mask introducing a variance.

4.1.2 Simulations

L-PICOLA

In order to produce cosmological constraints from Minkowski functionals, it is necessary to produce a library of the measurements in different cosmologies. This is done through the use of simulations. We choose to produce our simulations with `L-PICOLA` (Howlett et al., 2015), due to its capability to produce realistic simulations of the dark matter field significantly faster than a full N-body implementation. `L-PICOLA` is a highly parallel code that has been shown to produce accurate dark matter simulations 1000 times faster than an N-body approach(Howlett et al., 2015), and importantly reproduces clustering beyond two-point statistics. The code is adapted to output particle positions as they exit the lightcone, making map production simpler and runtime is reduced. Using quick simulations means that it is possible to build much more complete libraries of the functionals in different cosmologies, and they can produce the high number of skies required to produce accurate covariance matrices. Ideally, all simulations would be full N-body so that maximum accuracy in the clustering can be achieved, but computational limits and the demand of high numbers of independent realisations of the Universe make this presently infeasible. The `L-PICOLA` simulation package is sufficient for our current demands and we will show that it produces reliable simulations for our purposes.

`L-PICOLA` achieves these quicker outputs through implementing the comoving Lagrangian acceleration (COLA) method (Tassev et al., 2015). The simulation begins with a random field, distributing particles according to a power spectrum input by the user at a selected redshift. Simulations then seek to solve the resulting motion of these particles through cosmic time, attempting to solve an equation of motion (Bouchet et al., 1995; Scoccimarro, 1998) given as

$$\frac{\mathrm{d}^2\vec{\Psi}}{\mathrm{d}^2\tau} + H(\tau)\frac{\mathrm{d}\vec{\Psi}}{\mathrm{d}\tau} + \nabla\Phi = 0, \tag{4.4}$$

where $\vec{\Psi}$ is the displacement vector of the particle, ϕ is the gravitational potential that the dark matter particles move in and $H(\tau) = \mathrm{d}ln(a)/\mathrm{d}\tau$ is the conformal Hubble parameter. The potential is calculated using knowledge of the density contrast at a given point, relating the two through the Poisson equation. Solving this equation exactly is difficult as it requires knowledge of the matter distribution across all scales, so approximations are typically introduced. A popular approach is second order Lagrangian perturbation theory (2LPT), which attempts to solve the displacement vector by ignoring higher order contributions, and restricts itself to modelling motion on linear and quasi-linear scales. COLA goes a step further than this, using the large scale quantities known from 2LPT and saves computation for solving the equation on the smaller scales. `L-PICOLA` then uses the Kick-Drift-Kick (Quinn et al., 1997) to move the dark matter particles at each time step, using both the potential caused by the position of the particles at that given snapshot and the previously calculated 2LPT result. Particles are located on a mesh such that they can be Fourier transformed for calculating gradients. Through running this code from initial conditions through comsic time, late time clustering of particles can be modelled, without required expensive calculation of every particle position and velocity at each step. This results in such an increase in the speed of the simulation that Howlett et al. (2015) find that the bottleneck becomes the time taken to read the dark matter files, rather than the simulations themselves.

We run the `L-PICOLA` simulations to a redshift of 0.65, before running it in lightcone mode until redshift 0. This means that particle positions are output as they leave the lightcone between these two points in time and we can build convergence maps for a plane of sources located at redshift = 0.6. This corresponds to a volume of 1600 Mpc/h, and we run our simulations with 1024^3 particles spread on a 1024^3 mesh. We choose to run with a high number of time steps during the lightcone output phase (300 steps) in order to ensure that the simulations are as accurate as possible given our resource constraints, but further work could explore the minimum viable parameters

to achieve the required results. In practice, the time taken per simulation was not a particularly limiting factor, where we could produce a catalogue of dark matter particle positions in 2 hours, running on 64 cores and utilising the MPI capability on SCIAMA.

The accuracy of the weak lensing observables produced using the COLA approximation were examined in Izard et al. (2018). In this paper, they compared the convergence power spectrum produced using COLA to that produced in N-body simulations, and found that there was agreement within error bars up to an $\ell \approx 1000$. Fluri et al. (2018) used `L-PICOLA` for measuring peak statistics, and also found that errors introduced by using the COLA approximation were small. Peaks, as a probe of non Gaussian statistics, are a similar probe to Minkowski functionals. These previous studies support the viability of `L-PICOLA` for weak lensing studies.

Convergence map production

Once we know the particle positions, it is necessary to go from this three dimensional particle density field to a two dimensional projected density map. We produced these maps using the particle positions output from the routine, binned angularly and radially. A hypothetical observer was considered to be at a central location in the box, and full sky convergence maps were produced according to the assumption that there was a plane of source galaxies at redshift of 0.6. From Bartelmann & Schneider (2001), we can calculate the convergence that each particle would contribute to such source galaxy observations through:

$$\kappa_{eff}(\vec{\theta}, w) = \frac{3H_0^2\Omega_{M,0}}{2c^2} \int_0^w \mathrm{d}w' \frac{f_K(w')f_K(w-w')}{f_K w} \frac{\delta}{a(w')} \tag{4.5}$$

where $\delta = \delta(f_K(w'), \vec{\theta}, w')$ is the density contrast at a given angular and radial distance. Written in this form, it is clear to see convergence map as an integrated density contrast, weighted with some geometrical contributions dependent upon the relative positions of the objects and further reweighted

according to the matter content of the Universe. We will only consider the case where all of our sources are in a single plane.

Due to the high number of particles and files output by the `L-PICOLA` simulations, it became necessary to write a mapping routine that worked in parallel. A series of files are output at each time step, denoting the positions and velocities of particles that have left the lightcone. We are running simulations with 1024^3 particles, across a large number of `dat` files, meaning that this will be slow when done sequentially. Instead, each output file was read in by a different node on SCIAMA by being submitted as a single job on a core, angularly pixelised using `HealPIX` routines and binned across redshift. The resulting file, of size (N_{zbins}, N_{pix}) was saved as an output. Up to 50 of these jobs were running concurrently, but in practice the only limit to the extent that this can be parallelised is the number of cores that are available. We found that this level of parallelisation was sufficient to produce maps relatively quickly, whilst also being a considerate user of the communal supercomputing facilities. These smaller files were then read in by a final routine, and all particles compiled into a single array, which allows for every pixel in each redshift bin to be assigned a density contrast for that slice in cosmic time. To produce the convergence map, these over-densities are weighted according to the distance to the centre of that redshift bin and contribution to the final convergence calculated. These maps were saved at a resolution of `nside`=256 due to the current resolution limitations of the mass maps produced in the Dark Energy Survey, but higher resolution maps would capture more of the non-Gaussian information that the functionals extract.

Some of the maps are displayed in Figures 4.2, for a range of Ω_{DM} values. These figures display a masked region of the true κ map on the sky, without any direct inversion mass reconstruction applied. Increasing the matter content produces structure of increasingly large density contrast relative to the background, with more areas being of either large over or under density. In contrast, the map made in a Universe of low matter content has

much fewer peaks or deep voids, with fluctuations typically much closer to the mean level. From visually inspecting these maps, the discerning power of topological measures becomes apparent.

Figure 4.3 shows the PDF for a range of the maps made, with varying matter content. This corroborates the visible difference between the maps in Figure 4.2, where increasing the matter content produces more pixels with κ values of higher over density. The shape of the distribution functions are also different for the different matter fractions, as higher order moments become larger and the distribution looks more log normal. The shape of the distribution also changes drastically with different σ_8 values, shown in Figure 4.4. Higher σ_8 values cause more values of higher κ, as the amount of clustering increases, and again making the PDF more log normal. Comparing the σ_8 PDF with the Ω_M PDF, similar distributions can be made by varying either parameter, so there is some degeneracy introduced by both having similar effects. Accessing the information present in the PDF is another potential source of cosmological constraints from mass maps (Patton et al., 2017) but I do not consider this in this work.

Covariance matrix

Accurate covariance matrix construction is necessary in order for our final constraints to be realistic, by allowing us to accommodate for correlations between different bins in our data. The shape of the Minkowski functionals is caused by two effects - the topology of the true κ field and a further noise component that alters the maps. The correlation between any two bins will therefore have a contribution from the true cosmological covariance, and another from the noise inherent in the measurement. Due to computational constraints, I choose to approximate the covariance matrix as unchanged in varying cosmological parameters. In reality, this will not be strictly true as the shape of the functionals vary with cosmology and this will alter the covariance. In practice, this assumption is a sufficient one given the levels of the constraints that we can produce and we show later in this section that

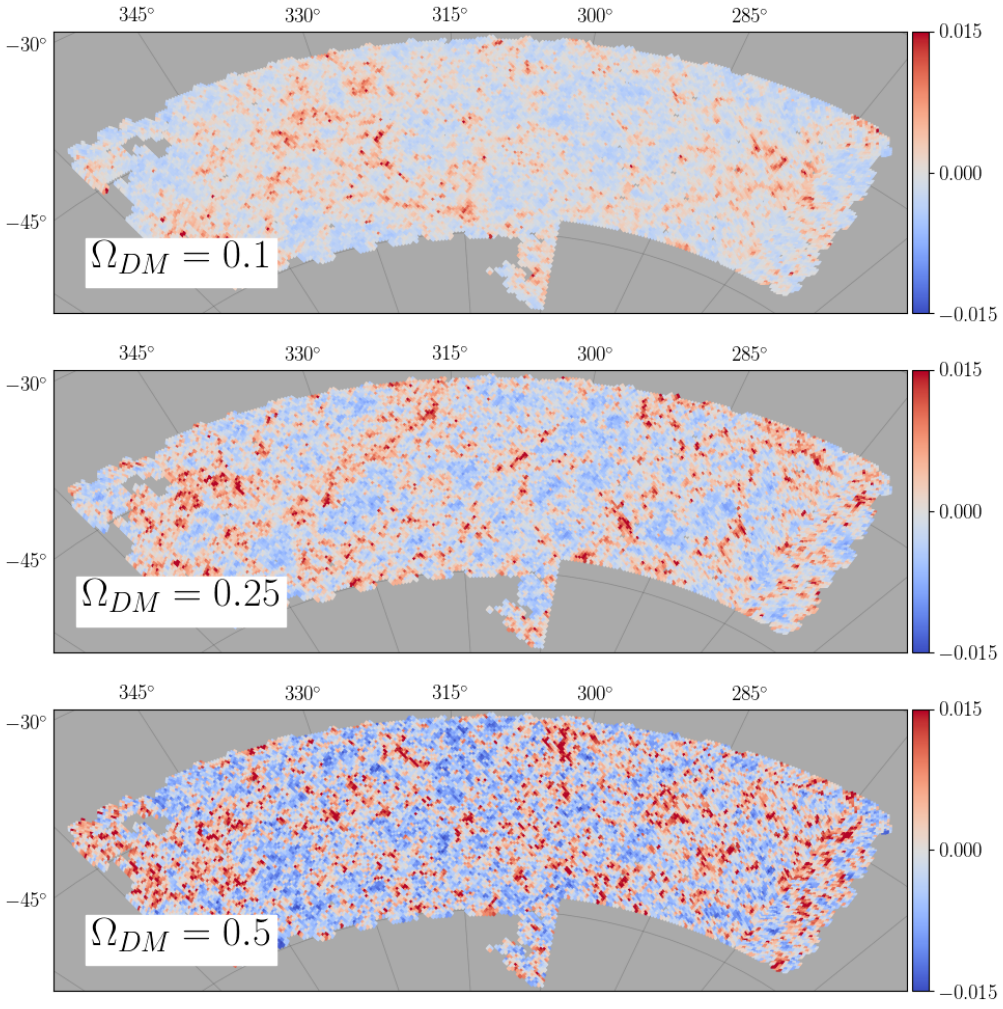

Figure 4.2: Some of the maps produced using the `L-PICOLA` simulation pipeline. A constant σ_8 was used for all maps and the matter content was changed, and the structures formed can be seen to vary across the different $Omega_{DM}$. This is what makes cosmological inference from the maps possible.

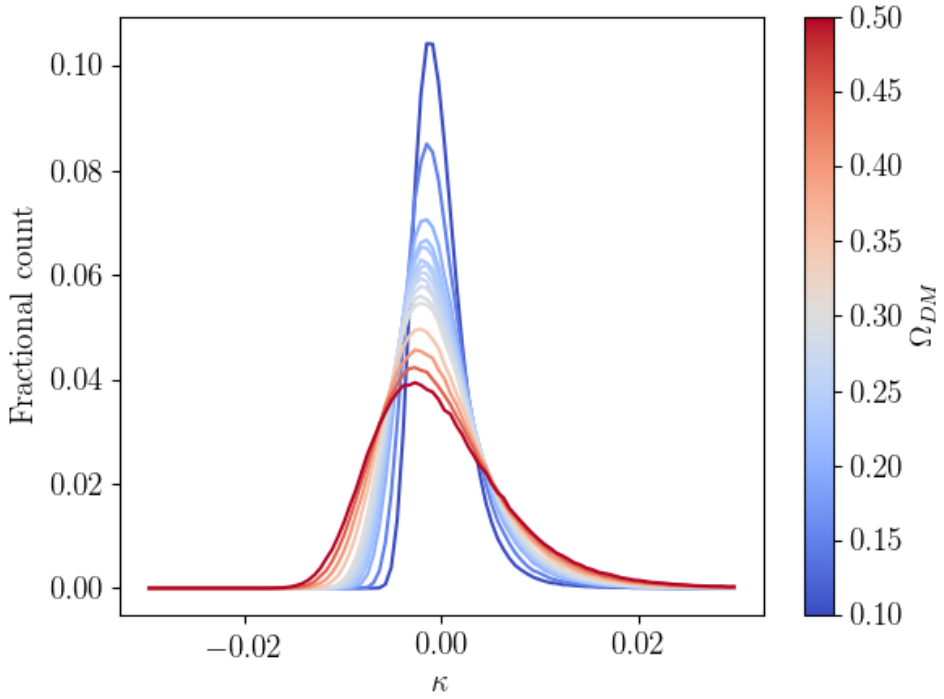

Figure 4.3: PDFs generated from a a suite of `LPICOLA` simulations, with a fixed $\sigma_8 = 0.8$ and $\Omega_B = 0.048$, whilst varying the dark matter content. Increasing the matter content produces more areas of higher over density, increasing the fraction of the pixels with higher κ values. The peak of the PDF is also shifted to a lower κ value.

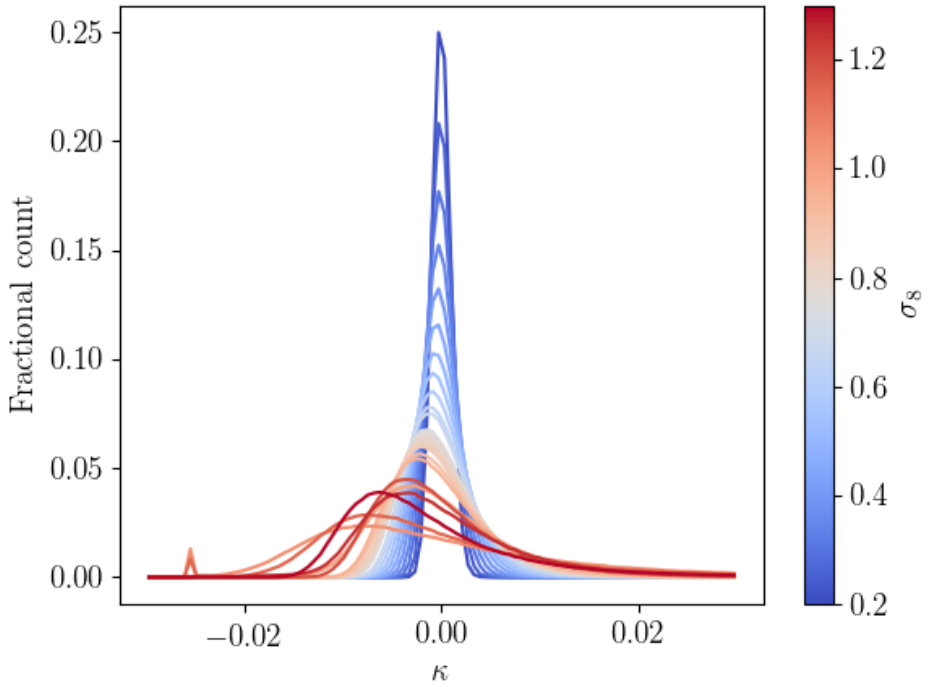

Figure 4.4: PDFs generated from a a suite of `LPICOLA` simulations, with a fixed $\Omega_D M = 0.24$ and $\Omega_B = 0.048$, whilst varying the power spectrum renormalisation factor σ_8.

our covariance matrices are suitable.

We build a covariance matrix Cov so that we can construct likelihoods χ^2 for an observed set of functionals M_{obs} relative to simulated functionals M_{sim}, according to

$$\chi^2 = (M_{obs} - M_{sim})\mathrm{Cov}^{-1}(M_{obs} - M_{sim})^\intercal \tag{4.6}$$

We build this matrix through producing many simulated maps at a reference cosmology of $\sigma_8 = 0.82$, $\Omega_b = 0.048$, $\Omega_{DM} = 0.25$ and $\Omega_\Lambda = 0.702$. The functionals are measured for each map on a selected footprint, dependent upon the data being examined. For fitting to a data set with unknown true cosmological parameters, an error field and the mean redshift of the galaxies used for shear measurement is used to build representative, repeat simulations that encapsulate mask and reconstruction noise effects. The covariance is measured between each functional measurement across n simulations according to

$$\mathrm{Cov}_{ij} = \langle (M_{sim,i,n} - \langle M_{sim,i} \rangle)(M_{sim,j,n} - \langle M_{sim,j} \rangle) \rangle \tag{4.7}$$

We build covariance matrices for each scenario that we intend to produce contours for, and include an underlying true κ field and a noise field. In this thesis, this means building covariance matrices for noiseless true κ fields and further matrices for the noisy mass reconstructions on different survey footprints. All confidence intervals presented in the following sections are calculated using covariance matrices designed in this way.

As we are attempting to produce constraints using the noisy mass maps reconstructed from DESY1 data, the covariance matrix used for this case is analysed in the following section.

Figure 4.5 shows the covariance matrix constructed for the noisy Y1 direct inversion mass maps, using a noise field from the Buzzard simulation. This covariance matrix was produced through simulating 150 full sky convergence maps in a cosmology with $\sigma_8 = 0.82$, $\Omega_b = 0.048$, $\Omega_{DM} = 0.25$ and $\Omega_\Lambda = 0.702$. The strength of the lensing effect was calculated assuming a delta

function of sources at $z = 0.6$, as this redshift is similar to that for the mean redshift of sources in both the Buzzard and DESY1 lensing catalogues introduced in chapter 3. Shear maps were made from these convergence maps using the relationships described in 2.4.1, and shape noise was added to shear in each pixel by sampling from a Gaussian distribution with a standard deviation given as

$$\sigma_{pix} = \frac{\sigma_\gamma}{\sqrt{N_{gal,pix}}} \tag{4.8}$$

where σ_γ is the standard deviation of the shape measurement. This can either be the standard deviation across all shape measurements in the survey, or for a more accurate quantification of noise it can be the standard deviation within a pixel. Although the error field (defined in equation 4.8) remains constant, new noise fields are generated each time by sampling from this error in each pixel, and added to the shear measurements before a mass map is produced. The survey mask is applied to the simulated data and mass maps are produced using the usual direct inversion approach. The Minkowski functionals are then measured for this mass map and the process is repeated on different patches of the sky using different realisations of the noise field. Through this approach, we are able to build a covariance matrix which contains contributions from both cosmological and observational effects. In total, the footprint is replicated by rotation on the sphere. A total of 40 survey footprints can therefore be produced from a single full sky true κ field, and this is replicated across 150 different skies to produce a total of 6000 realisations. A small amount of overlap, 5%, is allowed between the repeated footprints placed on the sphere.

The covariance matrix shown in Figure 4.5 is the one used to provide cosmological constraints from the Buzzard simulation, with the addition of some extra columns found when the power spectrum is also analysed. Due to the varying size of each threshold value, some of the diagonal components are difficult to see, and some covariance on the off diagonal can be seen. The strong covariance between neighbouring bins can be seen in the case of V_0, where the central bins all share a strong covariance between each other.

Conversely, in the case of V_2, neighbouring bins appear to have close to zero covariance with each other. An extra section is included in this covariance matrix to display the relationship between the functionals and the power spectrum. These bins in the C_ℓ section of the plot correspond to the mean power measured in logarithmic bins in harmonic space, when considering the spherical harmonic representation of the convergence map. This has been included as we will later use constraints from the DESY1 cosmic shear analysis to produce combined constraints, and it is necessary to ensure that the covariance between the two data sets is negligible if we are to be able to combine them in a simple way. It can be seen from this plot that there does indeed seem to be a level of covariance, but leave a full analysis of the accurate combination of Minkowski functionals with power spectrum measurements to later work.

The varying scales involved in the covariance matrix mean that it can be difficult to interpret the strength of the correlation between different bins. Figure 4.6 shows the correlation matrix, which can be found from the covariance matrix according to

$$\mathrm{Corr}_{xy} = \frac{\mathrm{Cov}_{xy}}{\sqrt{\mathrm{Cov}_{xx}}\sqrt{\mathrm{Cov}_{yy}}} \tag{4.9}$$

and the result is a matrix consisting of the Pearson coefficient between each variable. Dividing the covariance matrix by the diagonal terms has the effect of normalising the correlation when considering values that range across many different orders of magnitude. For example, an off diagonal term could appear to have a strong covariance with another parameter when compared to its autocorrelation, but this could arise due to one term being of a much larger magnitude, and the correlation actually being weak. Viewing the normalised correlation removes this source of confusion.This correlation matrix is strongly diagonal, with the autocorrelation being by far the most significant. A second plot is shown in Figure 4.7 shows the same correlation matrix, but now displayed as the base 10 logarithm of the absolute value of the correlation coefficient. The off diagonal correlations are now much more

visible and the difference in scale between the off diagonal and autocorrelation terms can be much more clearly seen, with the autocorrelation being several orders of magnitude larger than some correlations between different bins. Some correlations are negative, but the modulus of the correlation was plotted as the magnitude of the correlation is the more important initial test, rather than the sign. Whilst there are correlations between our simplified C_ℓ bins and the Minkowski functionals, a full and reliable matrix would require a complete modelling of the two point analysis pipeline. I choose to work with the approximation that the weak lensing power spectrum analysis can be combined with the Minkowski functionals as treating both data sets as uncorrelated, which will make later analysis significantly simpler, and means that the maximum benefit will be derived from combining measurements. This will provide an indication of the best possible constraints using the functionals. Whilst a complete analysis would consider this covariance and perform the analysis of both the Minkowski functionals and power spectrum, in the form of a joint analysis, this is beyond the scope of this work.

Effect of assuming a cosmology

In an ideal world, a covariance matrix would be constructed for every cosmological model that we are considering, so that it is correctly modelled in each case and the likelihood at each point in the parameter space is correct. As we change the cosmological parameters in the simulations, the shape of the functionals changes and the covariance matrix should also change to reflect this differing relationship between the bins. In reality, we find it prohibitive to produce a covariance matrix for every model, and we assume a cosmology in the centre of the models tested. This saves us extensive computing power, although we are still required to produce 150 independent realisations of the full sky to produce out covariance matrix, with each one typically taking several hours to complete on SCIAMA. It is apparent that were we to need to replicate this across the 200 different models that we consider to produce unique covariances for each model, it would take significant time even with

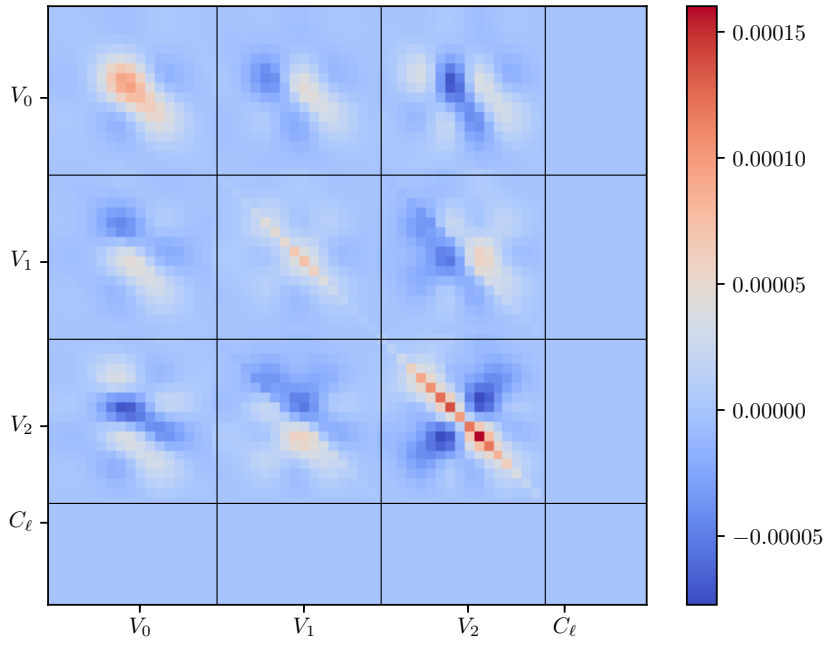

Figure 4.5: Covariance matrix constructed for the Y1 noisy mass maps when measuring the Minkowski functionals. Some off diagonal relationships exist, for example in the top left corner for the V_0 statistic, where the shape of the functionals at one threshold has a strong covariance with neighbouring bins. An evaluation of the cross correlation with the power spectrum is also included, to examine the potential for cross correlating with the Minkowski functional measurements. The broad range of scales involved mean that correlation is difficult to infer from this plot - see Figure 4.6.

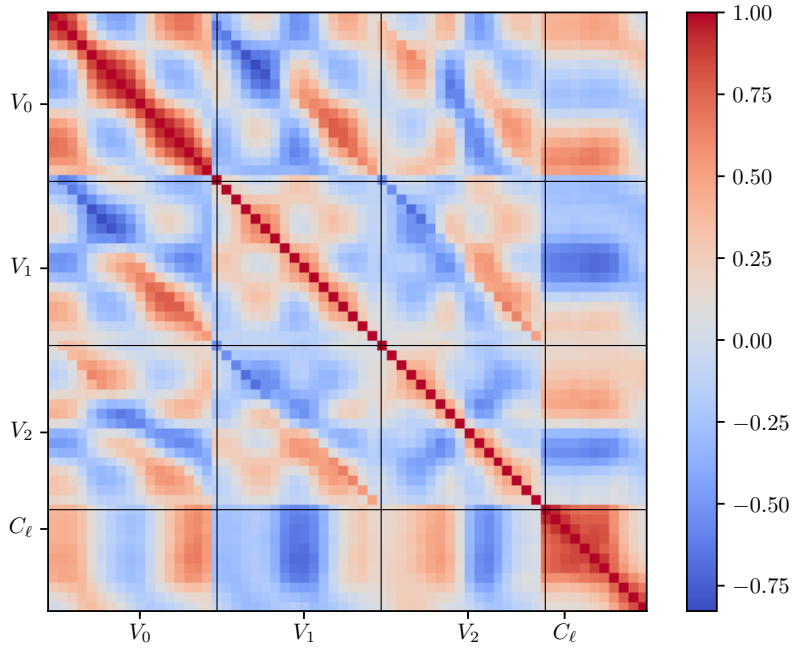

Figure 4.6: Correlation matrix for the Minkowski functionals and averaged power spectrum measurements. There is a strong diagonal and some other terms exhibit strong correlation with neighbouring bins.

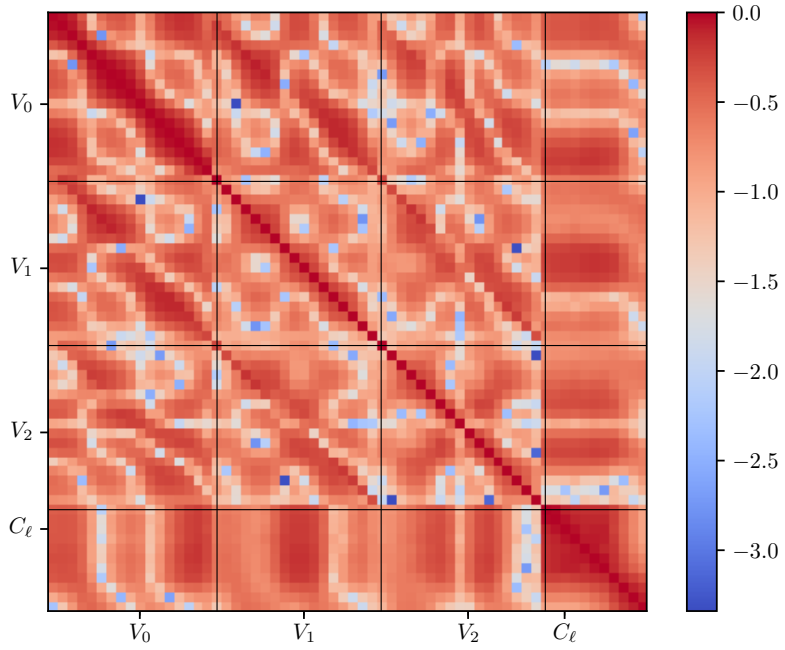

Figure 4.7: Base 10 logarithm of the modulus of the correlation matrix for the Y1 Minkowski functionals. This visualisation better shows the variation in magnitudes of correlation.

the HPC resources available at Portsmouth.

We check the validity of assuming one covariance matrix across the models by producing one comparative matrix at a cosmology significantly different from that used as the reference. For this example, we use our reference cosmology models produced earlier ($\sigma_8 = 0.82$ and $\Omega_{DM} = 0.25$) and a new alternative cosmology with significantly different parameters ($\sigma_8 = 1.1$ and $\Omega_{DM} = 0.4$), and build the matrix in the usual way. We then measure the χ^2 for each model with a reference model using each matrix, and calculate the difference between the two estimates, which is shown in Figure 4.8. The mean difference between the χ^2 measured is 14, or a fractional difference of 12%, with the fractional change also plotted in figure 4.9. Some large outliers skew these measurements, such that the median difference is much less than the mean, at a change in χ^2 of 7 for the combined measurement across the 3 functionals, each measured in 17 bins. The largest changes in the χ^2 are in the models nearest to the alternative cosmology, as the alternative covariance matrix will be more accurately modelling the χ^2 in this regime, but when viewed as a fraction of the χ^2 of that calculated by the reference cosmology, the differences do not exceed 20%. The differences are also quite uniform across the models which are far from the alternative model, albeit larger than those from the reference model.

We are primarily concerned with the effect that assuming an incorrect cosmology will have on the confidence regions measured from the functionals. The contours produced from both covariance matrices can be seen in Figure 4.10, and both matrices produce similar results. The cosmology of the map being tested is that of the Buzzard simulations, and the two different matrices produce a region of similar shape and the choice of cosmology does not appear to bias the constraints in any particular direction, despite the actual values of the χ^2 measurement changing across the parameter space. As most of the changes are relatively uniform, the likelihood is approximately that of a renormalisation. This means we can confidently use our matrix produced in a reference cosmology when producing constraints in the later analyses.

Future work could examine the potential for interpolating covariance matrices between different cosmological parameters, to improve the accuracy of the likelihood that is measured.

4.2 Minkowski Functional behaviour

In this chapter so far, I have shown that we can use `L-PICOLA` simulations to produce dark matter particle positions at late times, produce corresponding mass maps for a plane of sources at a chosen redshift and then measure the Minkowski functionals for these maps. In order to use these maps for cosmological constraints, it is necessary to characterise the behaviour of the Minkowski functionals in different combinations of parameters. As an initial approach to this, in this section I will explore how the shape of the Minkowski functionals measured for the true cosmological mass maps vary with different Ω_M and σ_8, before moving on to considering observational effects.

Using the outputs from these simulation runs, we can visually examine how changes in Ω_M and σ_8 affect the shape of the functionals, as shown in Figures 4.11 and 4.13. In these plots, the Minkoski functionals for the true convergence fields are plotted in a range of cosmologies. One parameter of σ_8 or Ω_M is kept constant and the other is varied, to show how these can alter the shape of the functionals measured. Figure 4.13 shows the effect of changing the matter content of the Universe, and a higher matter content produces higher peaks in both the V_1 and V_2 statistics. When examining these curves, it is also useful to look at the early maps and PDF plots for further context. Figure 4.14 shows the differences measured in the functionals relative to an average cosmology, to highlight the changes shown in Figure 4.13. At low values of Ω_M, the V_0 statistic produces higher values at negative thresholds and lower values at positive thresholds. As the V_0 statistic is a measure of the surface area of the values above a certain value, this can be interpreted as a low Ω_M Universe having a significantly smaller fraction of the pixels representing deeper voids, and more values are centred close to the

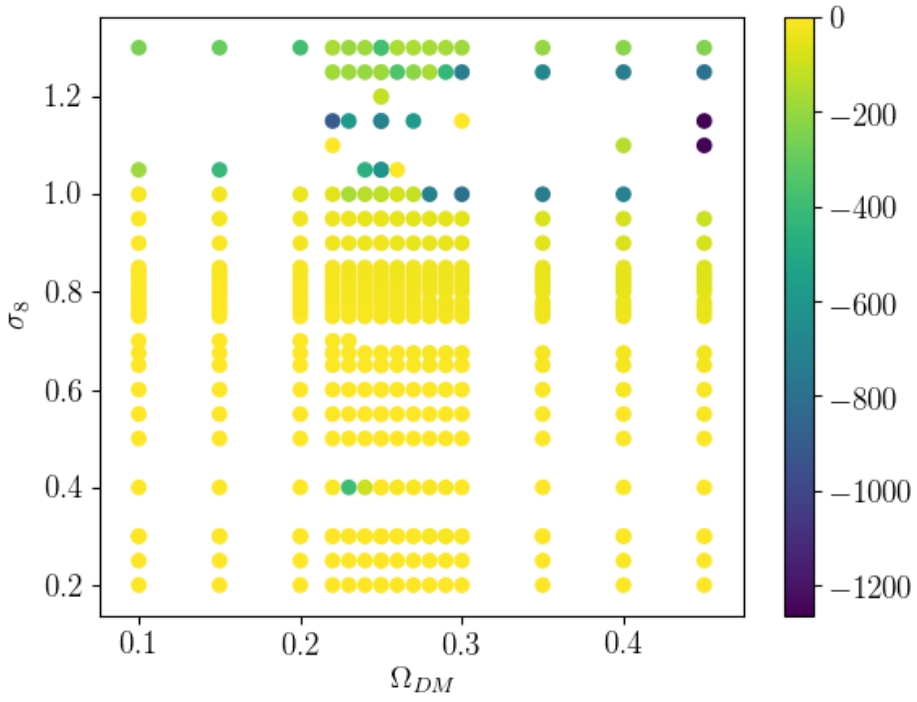

Figure 4.8: Demonstrating the effect of assuming a different cosmology when constructing the covariance matrix for producing cosmological constraints. The difference between χ^2 value calculated using a covariance matrix constructed in a reference cosmology [$\sigma_8 = 0.82$, $\Omega_{DM} = 0.25$] and one constructed in an alternative cosmology [$\sigma_8 = 1.1$, $\Omega_{DM} = 0.4$]. The change is small across most of the range of parameters considered, with the largest differences in the upper regions of the σ_8 values considered. This is expected behaviour, as the cosmologies in this area are much closer to that of our alternative cosmology. The covariance matrix from the alternative cosmology seems to have the effect of making all χ^2 measures larger.

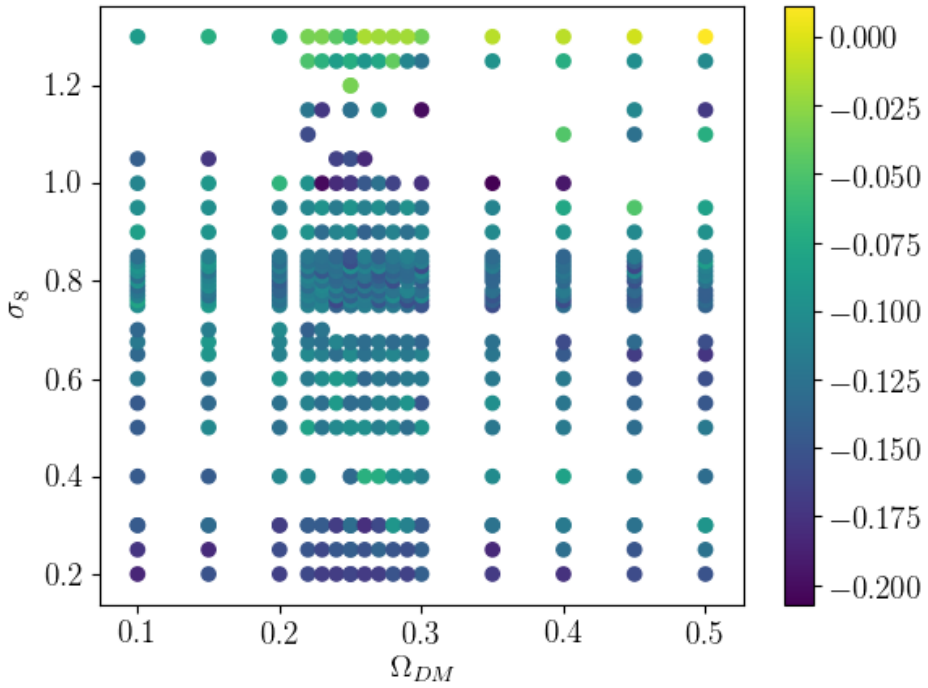

Figure 4.9: Demonstrating the effect of assuming a different cosmology when constructing the covariance matrix for producing cosmological constraints, expressing the values in figure 4.8 as fractions of the χ^2 measured in the reference cosmology. The fractional change can be seen to be relatively uniform and small (5-10 %) in the majority of the models concerned, with the largest fractional changes in the models closest to the alternative cosmology. Some large changes are also observed in the models at low σ_8, which are the furthest from the alternative cosmology.

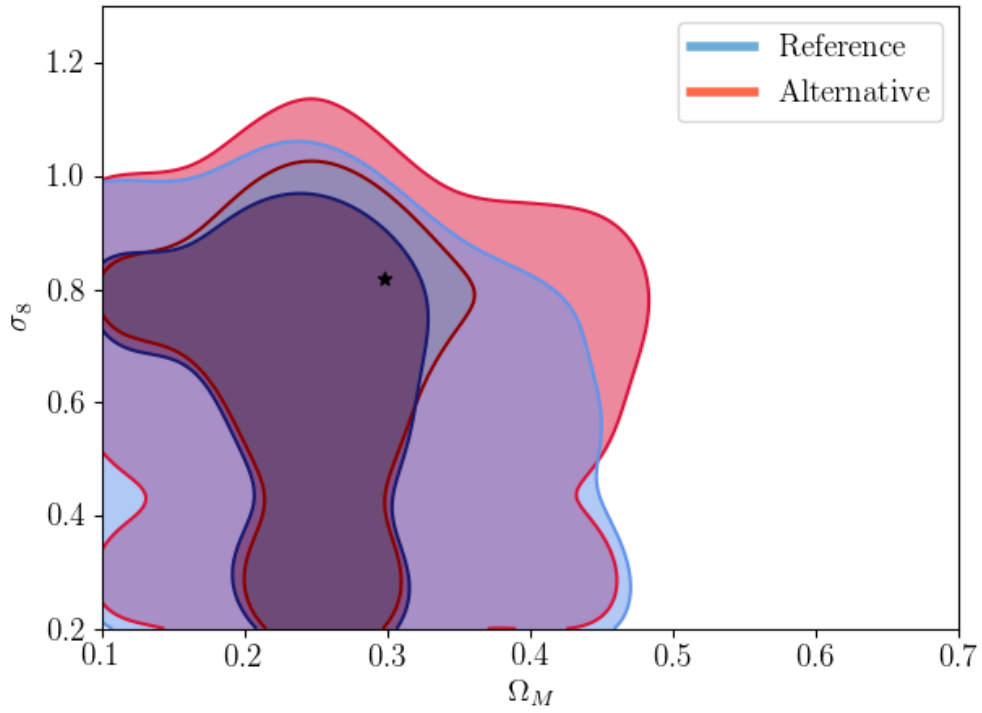

Figure 4.10: The confidence regions measured using the covariance matrices built using both the reference and alternative cosmologies for a Buzzard simulation, with the true cosmology shown as a black star. Slight differences can be seen around the edges of the contour, but they remain centred on the same area of the parameter space, meaning that our covariance cosmology does not appear to bias us away from certain parameter choices.

mean value. This means that Universes with a higher Ω_Λ content and lower matter content have their structure formation suppressed. At higher values of Ω_M, more structure at higher thresholds can form, concentrating mass into smaller haloes and deepening the voids. In the case of the V_1 statistic, higher values of Ω_M produce higher measures of the statistic across nearly all threshold values, meaning that the perimeter of the excursion sets are always larger in the universes with a higher matter content. This is due to more compact halos being formed, giving many smaller regions of a given density when compared to a lower matter content. V_2 is also shown to reach a higher magnitude negative value in the negative thresholds, and a higher positive value in the positive thresholds, meaning that the curvature of these areas is also more extreme , further supporting the story that the higher matter content produces more densely packed structures.

Figure 4.11 shows that higher σ_8 results in suppressing the height of the peak of both the V_1 and the V_2 functionals, but the behaviour is complicated. Figure 4.12 shows these deviations compared to an average cosmology, where the small changes in V_0 also become apparent. Here, higher σ_8 causes a higher value of V_0 at lower thresholds, which means a higher fraction of the map is in areas of higher overdensity, as expected for a higher σ_8 value. In the case of V_1, a higher σ_8 causes increasingly negative values, especially around $\pm 1\sigma$ thresholds, and V_2 is also suppressed at positive threshold values and enhanced at negative threshold values. A higher σ_8 therefore causes shape changes in an opposing direction to increasing Ω_M, and these parameters have a degeneracy.

Further, it is interesting to examine the shape of the Minkowski functionals for the `L-PICOLA` simulations in comparison to the functionals of a Gaussian field, and this is shown in Figure 4.15. From this figure, it is apparent that no simulation outputs a perfectly Gaussian field due to the structure formation processes that produce the final maps. These effects cause the shape of all 3 of the functionals to change. V_0 has a steeper gradient within thresholds of $\pm 1\sigma$ and has less of the distribution at values below $\approx -2\sigma$. V_1

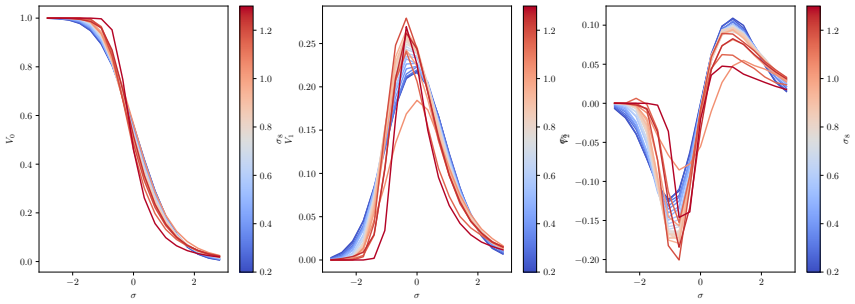

Figure 4.11: An examination of the influence of changing σ_8 at fixed Ω_M using `L-PICOLA` simulations, where the change in clustering amplitude causes large changes in the shape of the functionals.

becomes skewed compared to the Gaussian case, whereas V_2 has the sharpest differences visible in the thresholds below 0, where the non Gaussian fields reach significantly lower values for this functional. These deviations from the Gaussian fields show the extra information that the maps can contribute.

4.2.1 Effects of reconstruction

As we do not observe the κ field directly, but infer it through observed gravitational potentials, we will also need to model for the production of the mass maps if we are to be able to extract cosmological constraints from the maps.

The first effect that influences the direct inversion is that we do not observe a full sky of shear values, and this has been shown in Chapter 3 to introduce errors in the reconstruction. Using the masked shear fields from the `L-PICOLA` simulations we can explore the impact that this transformation has on the data, and this is shown in Figure 4.16, where the grey line shows the true functionals and the blue line shows the functionals for a direct inversion mass reconstruction on a masked portion of the true sky. The edge effects introduced by this reconstruction are of a significant magnitude, altering the PDF of the κ field by introducing pixels of either very high or

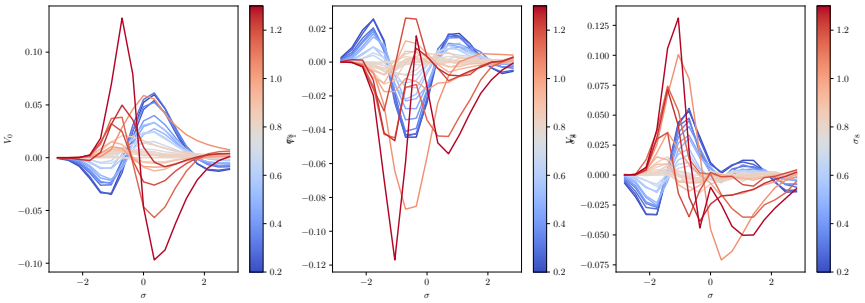

Figure 4.12: Differences between the Minkowski functionals measured in different cosmologies, displayed as a difference with a reference cosmology, for different values of σ_8. These plots more clearly highlight the differences in Figure 4.11, for example, V_0 shows a higher σ_8 produces a higher fraction of the pixels occupying κ values below the mean value of the field.

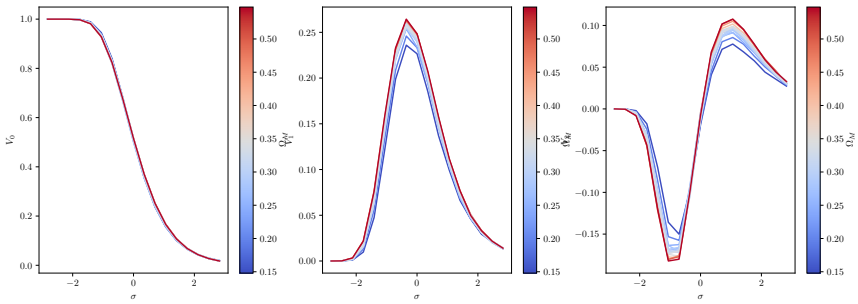

Figure 4.13: An examination of the influence of changing Ω_M at fixed σ_8 using the `L-PICOLA` simulations, where a smooth variation in the shape of the functionals can be seen. Higher matter content produces higher peaks and troughs across all of the functionals.

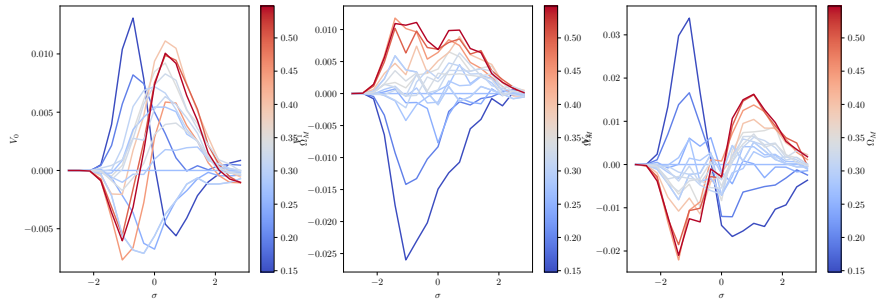

Figure 4.14: Differences between the Minkowski functionals measured in different cosmologies, displayed as a difference with a reference cosmology, for different values of Ω_M. V_0 shows that at higher Ω_M more pixels have κ values above the mean value, and the two other functionals smoothly differ in shape as Ω_M changes.

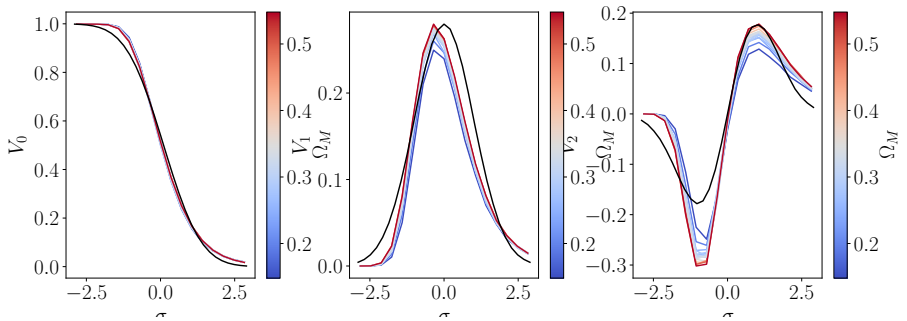

Figure 4.15: The Minkowski functionals for a range of simulations with different Ω_M compared to a Gaussian field. The Gaussian case is shown as a solid black line. The shape for all simulations differ from the Gaussian case, where structure formation introduces non-Gaussianities into the distribution.

very low convergence, and therefore altering the shape of the functionals. Figure 4.17 highlights these changes well, showing the differences between the functionals recovered through the direct inversion on a noiseless, masked sky and on a masked region in the presence of noise. In the case of the V_0 statistic, the direct inversion technique introduces an underestimate in the lower thresholds and a slight over estimate in the higher thresholds, as the edge effects introduce pixels of large convergence. These large values distort the PDF and will increase the standard deviation of the distribution, so when the field is normalised for measuring the functionals, the areas of under density become closer to 0. This is also the case for the larger overdensities, which become normalised to a lower number of standard deviations from the mean and the V_0 statistic is underestimated at higher excursion values. For V_1, the transform causes an overestimate close to 0 and an underestimate at the extremal values of the excursion sets, again as the higher standard deviation causes more of the map values to fall into a range closer to 0 when normalised, so the perimeter becomes larger in these areas. In the case of V_2, the direct inversion causes a slight underestimate of the true functionals at negative thresholds and a larger overestimate at positive threshold values.

Furthermore, adding shape noise also alters the shape of the Minkowski functionals by increasing the height of the peaks across all three of the observed functionals. Figure 4.17 shows that the V_0 functional becomes overestimated at thresholds around 0, and underestimated at higher thresholds, much of which is due to the effect of the transform. Shape noise appears to have the effect of distorting the shape even further, increasing the difference from the truth and shifting the point at which the reconstructed functionals line intersects with the true. V_1 becomes underestimated as low thresholds and significantly overestimated at positive thresholds, and the overestimation of the functionals $\pm 1\sigma$ of the mean becomes much larger. Shape noise introduces an spurious signal into the map, drastically increasing the standard deviation of the PDF and compressing the true signal closer to 0, as well as the effect on the overall topology of introducing new structures. These

structures are typically around the 1σ of the functionals for mass maps made using data from modern surveys, meaning there is a significant amount of structure introduced to the maps at this level due to shape noise. This has the effect of significantly increasing the perimeter of excursion sets that include this range. Shape noise also further distorts the V_2 functional, with the deviations from the true field becoming much more drastic than in the transform only case, which peaks in difference with the true field at $\pm 1\sigma$. All of the separate functionals therefore become distorted by the direct inversion and become markedly different from that of the true κ field alone, reiterating the importance of including the mass reconstruction in the mass map modelling when producing our library for cosmological inference. Although all of these effects remove the Minkowski functionals from their true values, if we accurately capture all of the necessary effects in our simulations, we will still be able to constrain the functionals in an unbiased way.

4.3 Calculating likelihoods

With accurate simulations of both the convergence field and the noise associated with our observations of it, we now turn to examining the potential cosmological constraints from these fields. We use the covariance matrices introduced in Section 4.1.2 in a variety of configurations depending on the field being examined. We first prioritise testing the approach on the Buzzard simulations for DESY1, before turning to examining the constrains on real DESY1 data. All maps are analysed at a scale of `nside`=256.

4.3.1 Considering ideal shear data

Firstly, we will examine the best case constraints from these fields, in the case when the convergence field could be perfectly reconstructed on masked area of the sky covering 1000 deg^2. Although this is not possible in reality, it provides an interested case study to indicate the potential of the maps. Figure 4.18 shows these best case constraints, in blue. There exists a significant

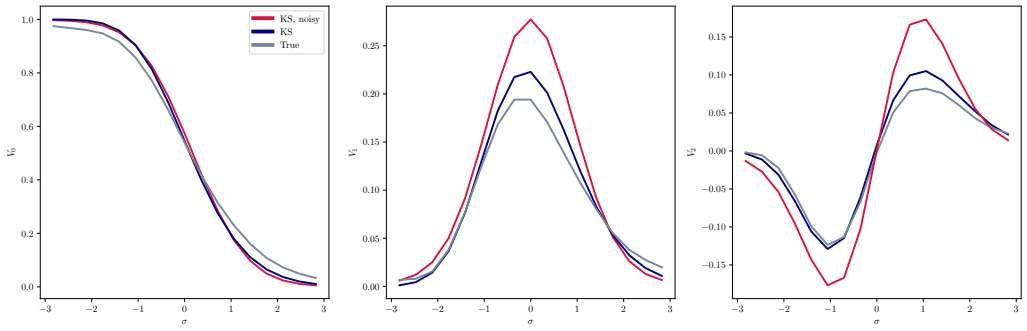

Figure 4.16: An examination of the observational effects present in the direct inversion mass mapping method, and how they affect the shape of the Minkowski functionals. The true κ functionals are those due to the cosmological structure in the Universe, and including observational effects such as noise from shape measurement and the direct inversion mass reconstruction significantly distorts the shape of the functionals measured. This highlights the importance of modelling the whole mass mapping pipeline when attempting cosmological inference with the functionals, as all three curves are made using the same true κ field, but unaccounting for the changes caused by the mass map production would give starkly different cosmological models.

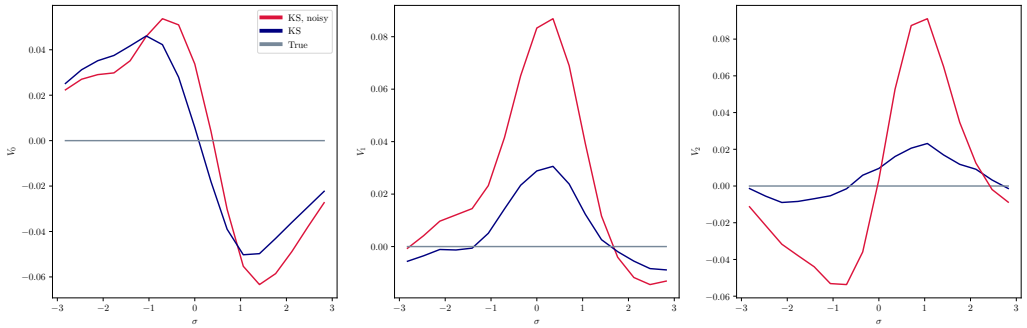

Figure 4.17: Comparison of the differences with the true Minkowski functionals for a field when reconstructed using the Kaiser-Squires direct inversion on masked and noisy data. The true κ field Minkowski functionals are used as a reference, so the smaller the value, the closer the measurement is to that of the true κ field. Shape noise is the dominant source of error.

degeneracy in the Ω_M direction. One cause of this is that Ω_M enters the final mass maps through a constant multiplicative factor, and we do not analyse the absolute values with the functionals. Therefore, they are all similarly normalised and we are insensitive to constant multiplicative factors and only detect the topological changes caused in the evolution of structure. Due to the complicated behaviour of σ_8 and Ω_M, changes in one parameter can be accomodated by changing the other to distort the functionals in a compensating way. It is also worth considering that these mass maps only probe scales above the pixel size of 20 arcmins, where some non-Gaussian information is present but there is significantly more information available at higher resolutions, which would decrease these contours further. The contours do offer some constraining power, so we will now move on to examine if it is still possible to extract cosmological information when all of the effects of the mass reconstruction are accounted for in the degradation of the shape of the functionals.

Constraints accommodating for the direct inversion

The effects introduced by the reconstruction of the Kaiser-Squires direct inversion are now added to our projected contours using the `L-PICOLA` simulations. We do this by masking the full sky true shear to an area of the Buzzard simulation, of 1000 deg^2, and producing mass maps through the usual direct inversion pipeline. Maps are produced through this approach for both the covariance matrix for the measurement and for the library of measurements at each set of parameters. As the noise is exactly known, our contours should encapsulate the true cosmology of $\sigma_8 = 0.82, \Omega_M = 0.3$. As seen in Figure 4.18, the transform has the effect of slightly expanding the confidence region, showing the reconstruction is adding an extra component to the covariance matrix beyond the contribution from variance due to the limited survey area and cosmology. Contour regions shown indicate areas of 68% and 95% confidence. The main effect of the transform is to introduce more uncertainty in the measurement of σ_8, with the high spurious κ signal

from edge effects imitating changes in clustering amplitude.

4.3.2 Constraints including shape noise

The final observational effect that we include in these simulations is that of shape noise. As shown previously, this uncertainty in the true values of shear in a pixel introduce changes to the topology of the maps and can be expected to alter the confidence regions that can be found for the cosmological models. This is modelled in the measurement pipeline by adding shape noise in all pixels in the mask according to $0.3/\sqrt{N_{gal}}$, with a galaxy density field from the Buzzard simulation. Figure 4.19 shows this contour, and it can be seen that the introduction of shape noise increases the size of the contours significantly. The degeneracy along the Ω_M direction persists from the idealised, noiseless shear maps in Section 4.3.1, but the shape noise has now expanded the contours along the σ_8 direction as well, in a much more dramatic way than applying the direct inversion alone does. The areas of κ that the shape noise introduces are interpretable as new clusters in the mass maps reconstructed, so adding such areas will degrade our ability to infer the clustering pattern. Comparing the contour to that produced using the direct inversion on perfect shear, the shape noise appears to expand the contour significantly more than the transform alone. Therefore, the limiting factor is more due to the shape noise in the shear measurements than it is due to the mass reconstruction method.

The Buzzard footprint is a somewhat pessimistic scenario - it is of lower galaxy density and across a smaller area of sky than the DESY1 area, and these maps are using the direct inversion method which is known to be a sub-optimal solution for current datasets. The ability to reconstruct reliable contours on a dataset when the noise effects are correctly modelled should therefore be seen as an encouraging validation of the potential for the functionals to be used in cosmological analyses, and probe further work to produce improved mass maps. They offer an alternative pipeline that includes non-Gaussian information, and can contribute to combine constraints. We have

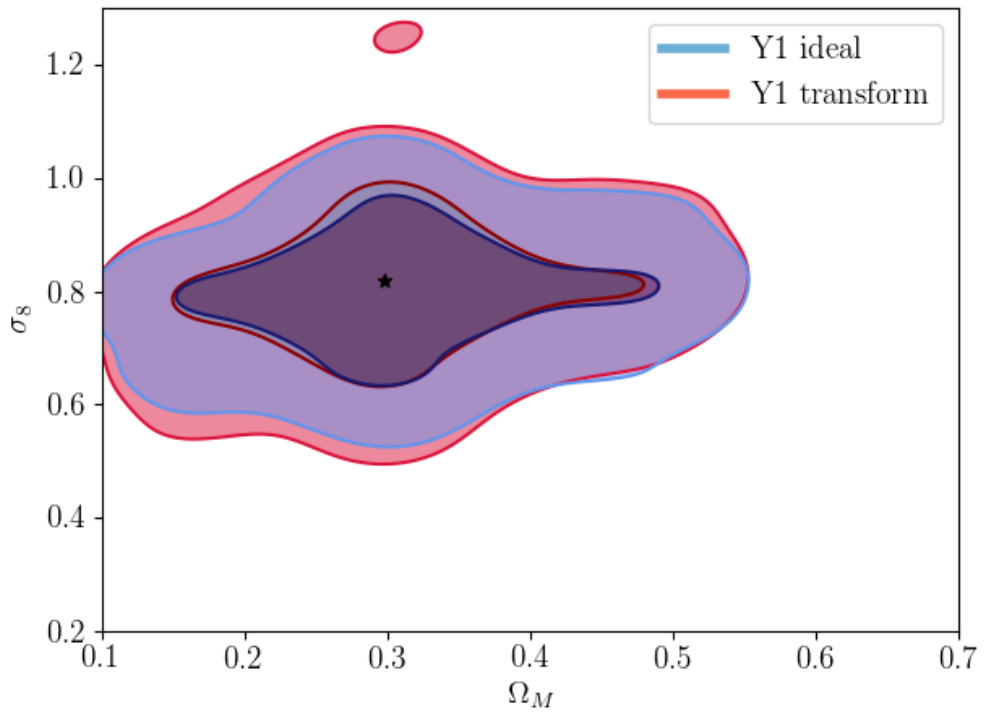

Figure 4.18: The cosmological constraints possible for a mass map produced through the Kaiser-Squires direct inversion approach on a masked area of exactly known shear, and for a reconstruction using the direct inversion on a masked field. Confidence regions indicate areas of 68% and 95%. The inversion expands the contour due to it introducing noise into the kappa field, noticeably reducing the constraining power in the σ_8 direction.

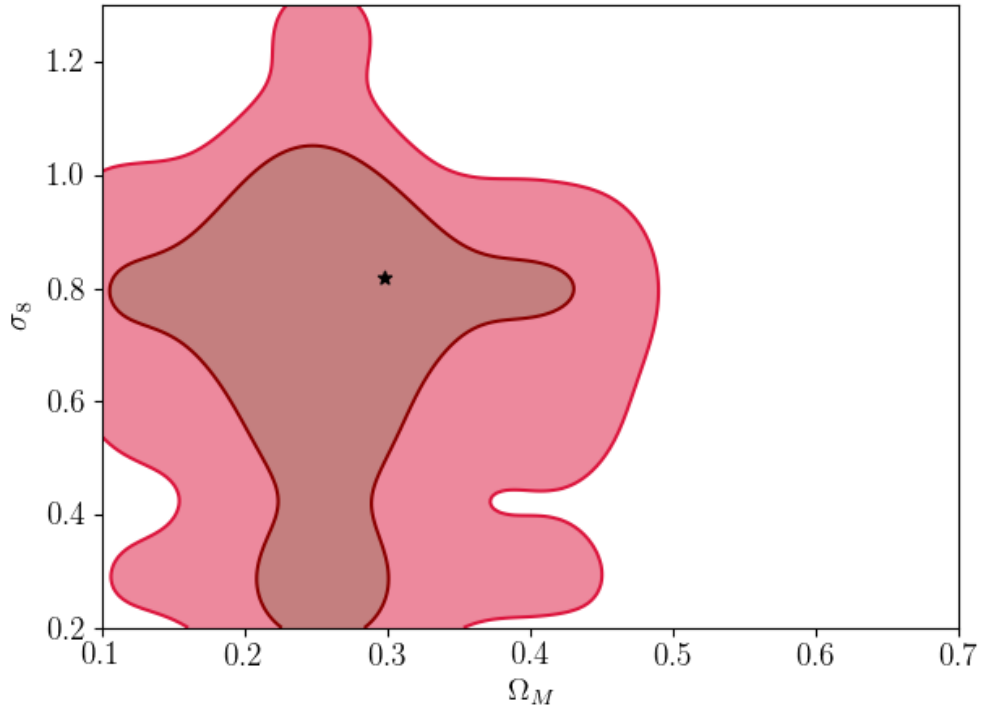

Figure 4.19: Cosmological constraints for a `L-PICOLA` simulation encapsulating both shape noise and map production effects for the direct inversion. Contours show areas of 68% and 95%, and the true cosmology lies comfortably within the 1σ range.

shown in this section that we can build a pipeline of simulated universes, produce mass maps with realistic noise and use them for self consistent inference. This is a vital achievement in order to move on to test the pipeline on more realistic simulations of the Universe, and observed data.

4.3.3 Buzzard validation

The final test that we can perform before applying the approach to data is to examine the accuracy of the constraints that we can find from the Buzzard simulations, used in the Dark Energy Survey. These simulations involve many effects beyond the LPICOLA dark matter simulations that we have used to

produce out density maps, so validating our results by getting a consistent cosmology with the Buzzard simulation settings would be an important validation step before attempting to fit to real observations. Importantly, they include convergence fields produced from sources distributed across redshift instead of at a single plane, and have populated dark matter haloes with galaxies. These will test our assumptions in approximating our sources as a delta function in redshift space and the validity of the `L-PICOLA` simulations against an N-body solution.

The cosmological confidence limit found comparing our `L-PICOLA` simulations with a shape noise according to the galaxy distribution in the Buzzard simulation can be seen in figure 4.20. Firstly and most importantly, the true cosmological parameters used in the Buzzard simulations fit comfortably within 1σ of the likelihood, which is a validation of the method. Despite the contour being large, there is a large area of the parameter space that the contour could have inhabited, or it could have found the simulations significantly far from the Buzzard simulation, so this is an important result. Interestingly, when compared to the previous self consistency checks, the region of 1-σ confidence now extends furthest in the σ_8 direction rather than in Ω_M.

4.3.4 Effects of observational errors

Redshift

Redshift estimation is a difficult but vital part of observational cosmology. Lensing is sensitive to the geometry of the system, so incorrectly modelling the arrangement of source and lens would result in incorrectly predicting the lensing amplitude. We examine the impact of an incorrect redshift measurement by producing two maps with source planes at different redshifts to the library of functional measurements. We place one plane at z = 0.5 and plot the resulting confidence contours in Figure 4.21. The contour is significantly biased by such a drastic change in redshift, but in modern weak lensing sur-

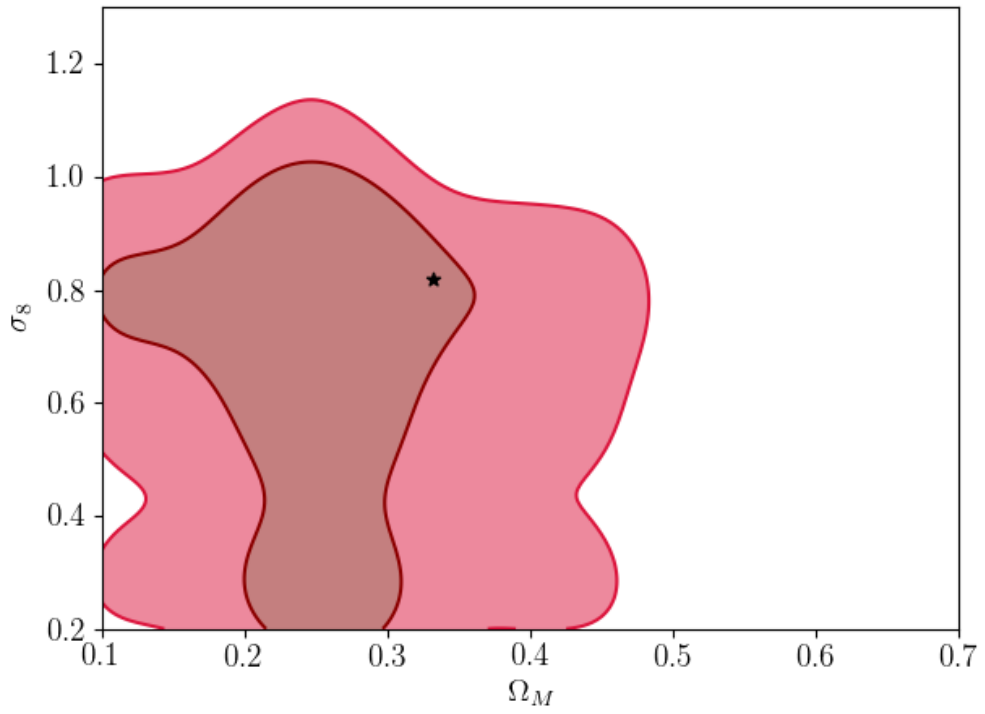

Figure 4.20: Cosmological constraints found by applying comparing our `L-PICOLA` simulations to a Buzzard simulation. The true cosmology is shown as the black star and 68% and 95% confidence regions are shown.

veys the redshift bias is expected to be significantly smaller than that used to produce this plot. Troxel et al. (2018a) states that they expect the bias in the mean redshift of the DES Y1 weak lensing catalogue to be no greater than 0.01, meaning that observing such a large discrepancy in our later analysis could not be explained by redshift errors. This error scale is similar to the scale of the redshift bins used to produce the `L-PICOLA` convergence maps.

Shape noise

The other main source of error is in shape measurement. In this section, we will consider the impact of our estimate of the noise on this shape measurement being incorrect, by producing two maps with noise on the shear drawn from a different distribution than that used in building the functionals library. We produce these alternative maps by supposing the noise in a pixel is given by $(0.2, 0.4)/\sqrt{N_{gal}}$, instead of the usual 0.3 or standard deviation of shape measurements in pixel. We then sample a noise field from this error field and produce mass maps in the usual way. This has the effect of lowering or increasing the noise added to the kappa map in a pixel, and we compare these maps to the library produced with noise drawn from a distribution of $0.3/\sqrt{N_{gal}}$. This will demonstrate how we would expect the contours to move if our data has a different noise field to that which we expect in our simulations. We produce contours for these maps, shown in figure 4.22, where the two are compared. When comparing a map with higher noise than expected, the contours are larger and the one σ confidence interval expands into higher values of Ω_M, which could be incorrectly interpreted as the data supporting a higher matter density contribution than it should do. The smaller contour does not have this effect. Larger noise can therefore be interpreted as having a similar contribution to the noise field as increasing the matter content in our simulations, whereas underestimating noise causes a loss of constraining power in the σ_8 direction. This can be most clearly seen by comparing Figure 4.16, showing how the introduction of shape noise increases the size of the peaks in the Minkowski functionals, and Figure 4.13, where increasing the

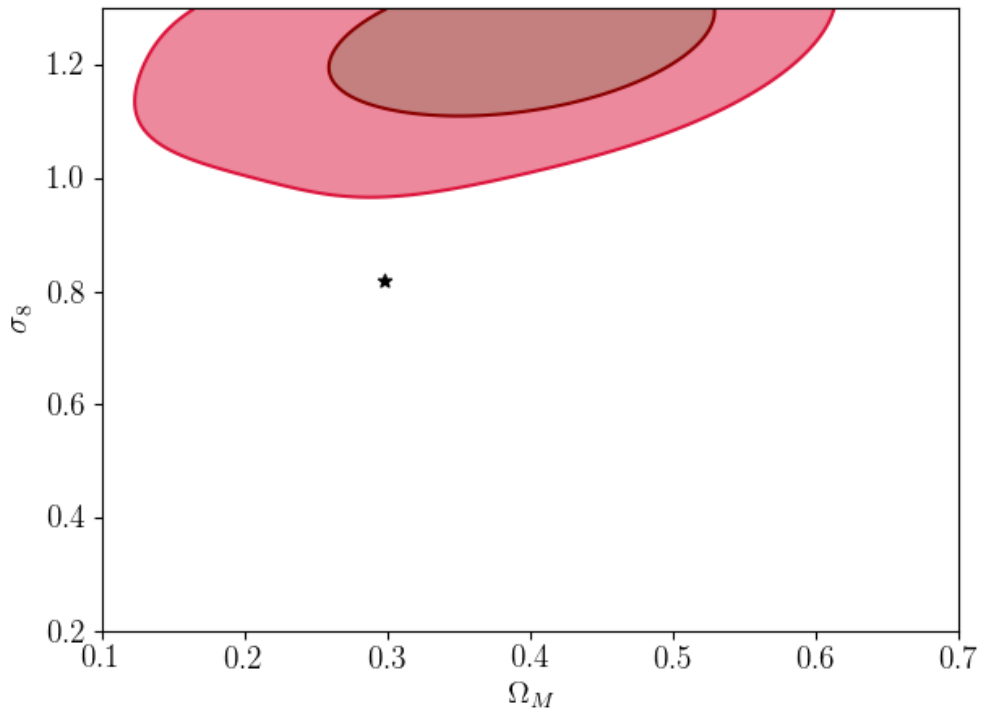

Figure 4.21: The bias introduced by incorrectly assumed redshift distribution. In this plot, a map with sources at z=0.5 was compared to our library of maps made at z=0.6, showing areas of 68% and 95% confidence. The dramatically incorrect redshift measurements cause σ_8 to be drastically over estimated, as more structure is observed in the maps than expected for lensing sources at a higher redshift.

matter content has a similar effect. In the context of the maps, the larger peaks of over density present in a universe with a high matter content become easily confused with similar large peaks in the density field introduced by the shape noise. Inaccurately modelling the noise can distort the contours in a significant way.

4.4 Cosmology with DESY1 mass maps

All of the tests in this chapter lead us to believe that applying the pipeline to the data will produce reasonable results. This section applies the same methodology to the DESY1 weak lensing catalogues to infer fundamental parameters describing the Universe, and combines our results with weak lensing power spectrum analyses to provide tighter constraints than either approach can do independently. Throughout the development of the pipeline, we believed in the importance of blinding. Our results on the Y1 data have only been run once, and all prior tests were performed with a masked `L-PICOLA` field, for ensuring there were no bugs in the pipeline. Once we were satisfied that all sections were reading in data correctly, the data map was input to the likelihood code and those results are shown in the following section. No further changes to the pipeline were permitted once it was decided to move onto analysing the data from DESY1, and no analyses were done on the Y1 data until all of the previous simulation tests were satisfied.

4.4.1 Cosmological constraints

Figure 4.23 shows the results for applying the Minkowski functional cosmological inference pipeline to the DESY1 data. This has a shape somewhat different to that for the previous simulation tests, and there are a few important differences in the Y1 footprint that will cause this. The DES Y1 data covers a much larger area of sky than the Buzzard simulation, and also has more galaxies present. These two factors will have the effect of reducing the contribution to the covariance matrix from both shape noise and the cos-

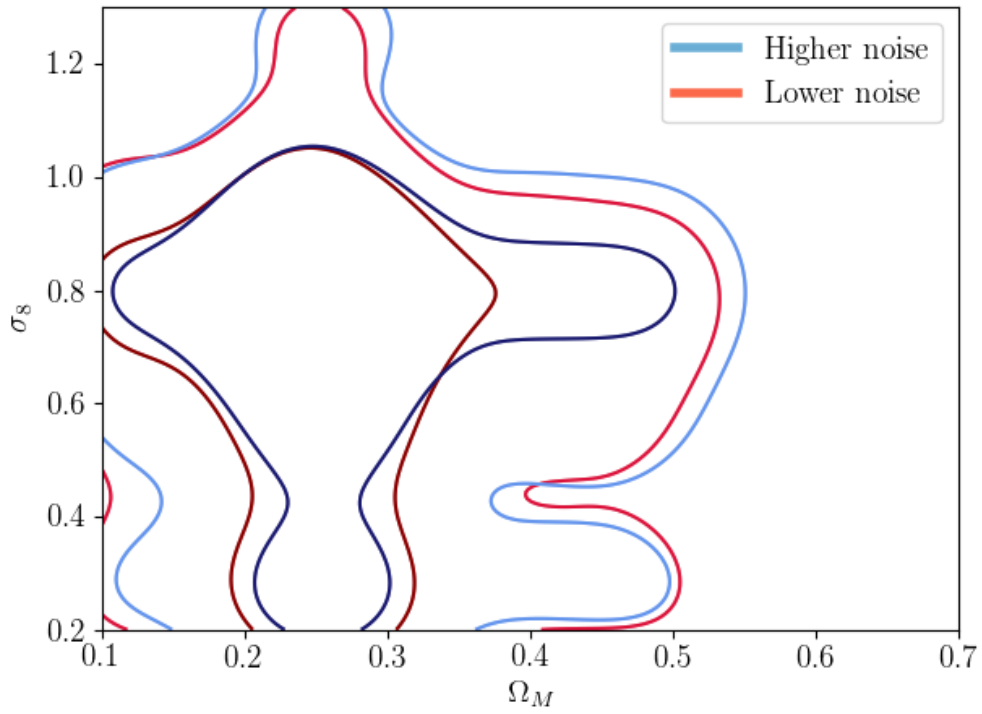

Figure 4.22: Demonstrating how incorrectly modelling the shape noise of the κ field changes the contours produced with the functionals, with 65% and 98% confidence regions shown. A higher noise is produced by modelling a larger standard deviation of shape measurements in a pixel, and a smaller noise has a smaller standard deviation. The increased noise does not seem to move the contour drastically but an underestimated noise could lead to interpreting higher Ω_M matters as being more consistent with the data The higher noise also has the effect of expanding the size of the contour region.

mological variance. The degeneracy along the Ω_M direction is still present though, as the contour is longer in that direction. We made the noise field as accurate as possible, by assigning the error in each pixel by calculating the standard deviation of shape measurements in that given pixel and dividing this by the square root of the number of galaxies present. We use the same true κ simulated skies from previous sections, but calculate a new covariance matrix to account for the new mask and error field. We also produce a new library of measurements of functionals with this noise field. The simulated output is then compared to the data using the same approach as previously to produce the contours.

4.4.2 Combining probes

The contour for the Minkowski functionals spans a significant amount of parameter space, and we would like to provide the tightest constraints possible. One way to do this is to combine measurements across different experiments, especially those with complementary degeneracies. By combining knowledge from different observations, the likelihood can be updated to include information from both and result in a smaller area to the contour. Our earlier work has led us to believe that we can combine the Minkowski functional measurements with two point analyses in such a way that we can neglect the covariance between the probes. An initial comparison of the constraints produced by the two analyses is shown in Figure 4.24, with the results from Troxel et al. (2018a) shown in the blue contour, displaying the familiar "cosmic shear banana". Immediately, one can see the remarkable agreement between the two pipelines; this is non trivial, that two different cosmological measurement pipelines find entirely consistent results, despite very different methodologies, albeit that they do share use of the same shear catalogue.

The next step is to produce the combined constraints - Figure 4.25 displays this, with both individual approaches included for ease of comparison.The combined confidence region, in light blue, is noticeably smaller than that for the DESY1 cosmic shear analysis alone, showing how the addition

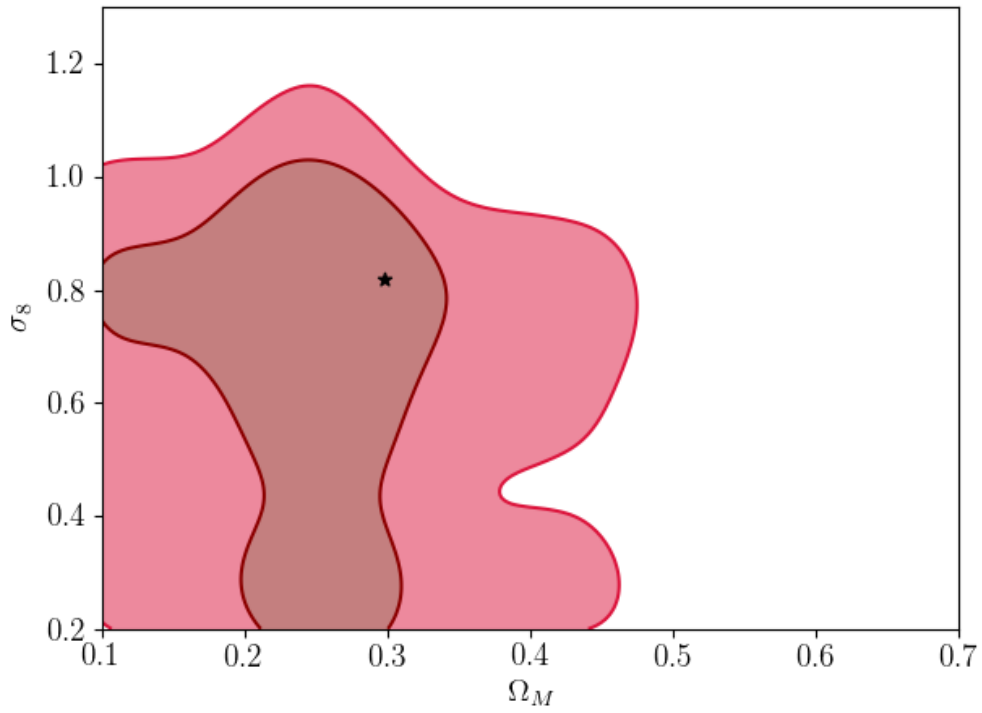

Figure 4.23: The confidence regions derived using Minkowski functional measurements of mass maps produced using the direct inversion approach on DESY1 data, with 68% and 95% confidence regions. The different survey mask and galaxy count will make this contour slightly different to that from the Buzaard simulation.

of the information from the Minkowski functionals can significantly improve the constraints. The two likelihoods can be combined by multiplying the two probabilities together, then renormalising so that the sum of all probabilities equals 1. The overlap between the two probes means that a tighter contour can be produced, reducing the uncertainty appreciably and providing a technique for improve the two point results. Individually, I find a 68% confidence interval using only Minkowski functionals of $\sigma_8 = 0.79^{+0.1}_{-0.40}$ and $\Omega_M = 0.25^{+0.07}_{-0.06}$, compared to the results from Troxel et al. (2018a) of $\sigma_8 = 0.82^{+0.07}_{-0.11}$ and $\Omega_M = 0.27^{+0.08}_{-0.04}$. The two results show a strong agreement, with the best fit result for each parameter falling within one standard deviation of the other. Figure 4.26 shows the marginalised results, separating the results for the two cosmological parameters into separate plots. For σ_8, despite the probability distribution for the Minkowski functionals being quite broad, there is still a notably narrower distribution for the combined results when compared to the DESY1 shear alone. With Ω_M, where the functionals provide a confidence region of comparable size to the DESY1 analysis, there is also a sharply noticeable narrowing of the probability distribution, and the strength of the result from the Minkowski functionals has the effect of moving the best fit result slightly lower.

Combined, I find that the final results for the two parameters are $\sigma_8 = 0.83^{+0.05}_{-0.06}$ and $\Omega_M = 0.26^{+0.04}_{-0.03}$, giving the tightest constraints on these parameters to date using only DES weak lensing data. Further, this result can be compared to those found from the CMB experiment Planck (Planck Collaboration et al., 2018) in Figure 4.27, which found $\sigma_8 = 0.8111 \pm 0.006$ and $\Omega_M = 0.315 \pm 0.007$. The contour shown is for the 68% and 95% confidence regions in the Planck TT + TE + EE analysis. There is some discussion in the field about the level of agreement between CMB and weak lensing studies, especially in the Ω_M - σ_8 plane where these is the suggestion of a disagreement between the probes. The marginalised confidence region for σ_8 places the Planck result comfortably within my 68% confidence region, and the Planck Ω_M result within my 95% confidence region. This is an important

result, indicating consistency between the two results measured at early and late times in the Universe, especially when there is ongoing debate about the level of agreement between the CMB and later time observations. Using low redshift weak lensing results with high redshift CMB measurements would be a powerful cross correlation to provide combined constraints from both probes, but this requires careful consideration of the covariance matrix for the two experiments, which is beyond the scope of this thesis. As the confidence regions will shrink with future data sets, the functionals will provide an important additional source of information for lensing studies, and allowing for a stronger detection of potential deviations between the two surveys.

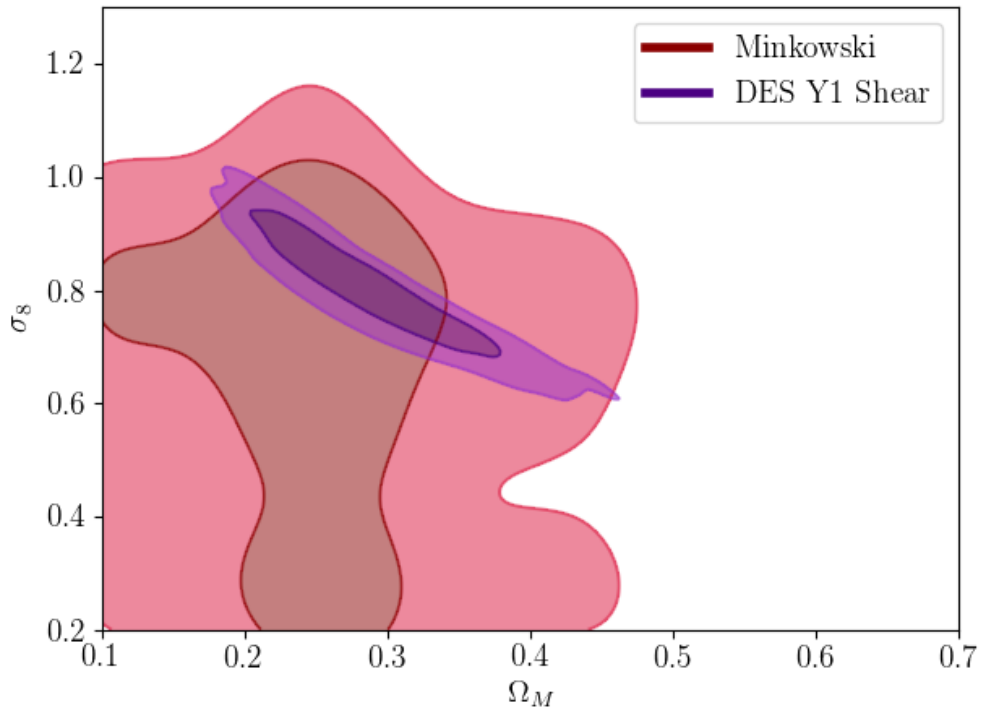

Figure 4.24: Comparing the constraints found in the DESY1 two point measurements and the Minkowski functionals pipeline. The DES Y1 shear shows a degeneracy from high σ_8 and low Ω_M, to lower σ_8 and higher Ω_M. Interestingly, despite the contours from the Minkowski functionals being significantly larger, they do not exhibit the same degeneracy. The two approaches show significant overlap, which is a reassuring result considering they use the same data set. The darker colour contour indicates the 68% confidence region, and the lighter shows the 95% region.

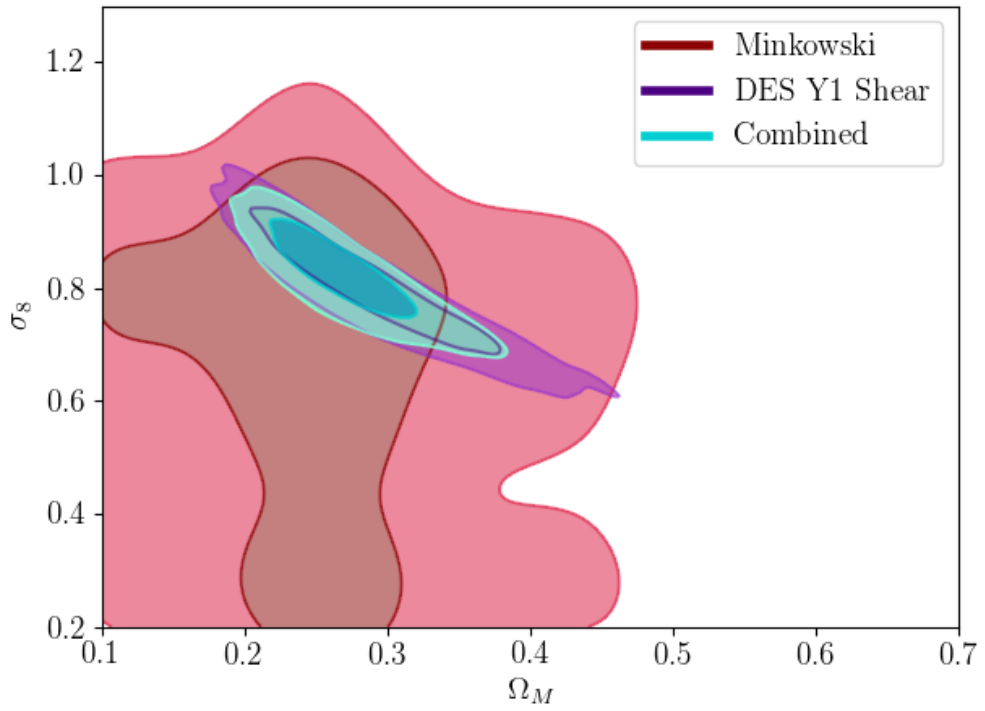

Figure 4.25: Combined constraints from the DESY1 cosmic shear analysis, which is improved through the addition of the information from the Minkowski functional results, with 68% and 95% confidence regions shown. The light blue, combined measurement shows a marked reduction in the size of both confidence regions, showing the power of including the functionals.

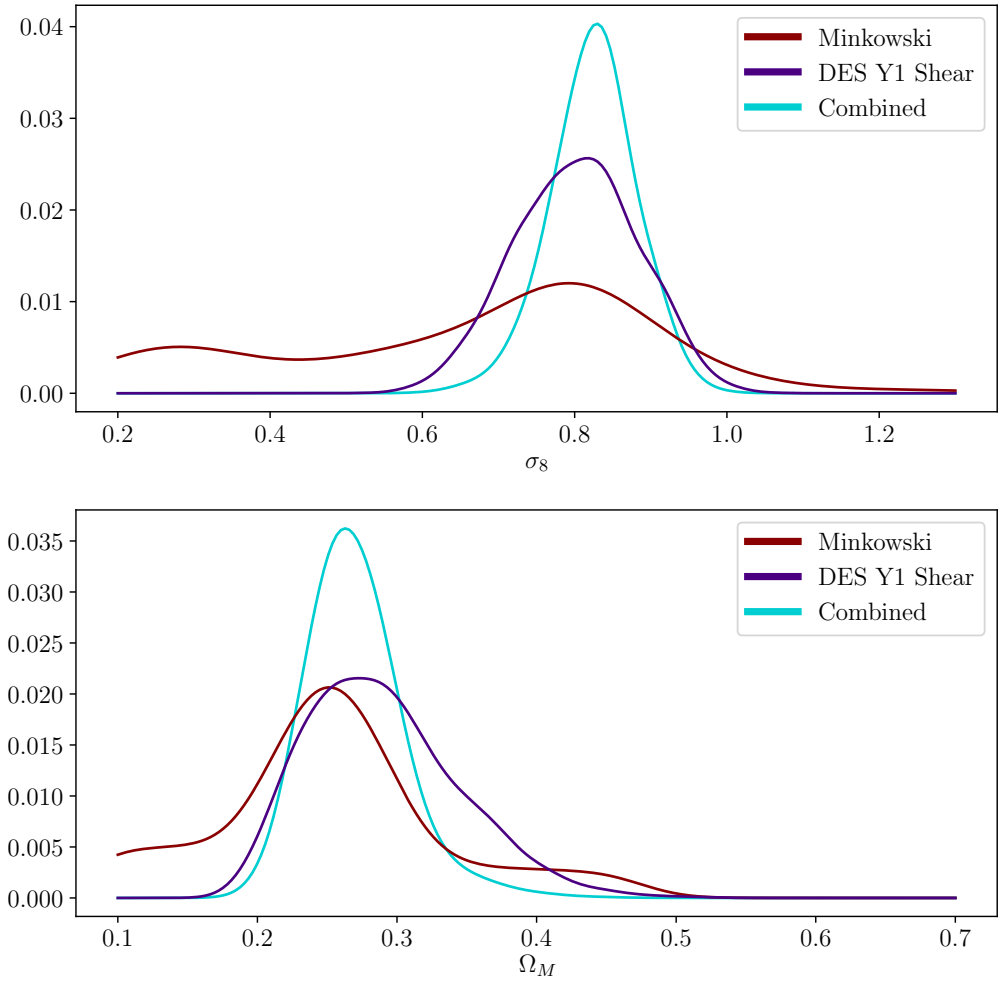

Figure 4.26: The marginalised constraints for the two parameters, with the probability shown on the y axis. The combined result is shown in light blue and the distribution is much narrow that either the functionals or DESY1 can produce alone.

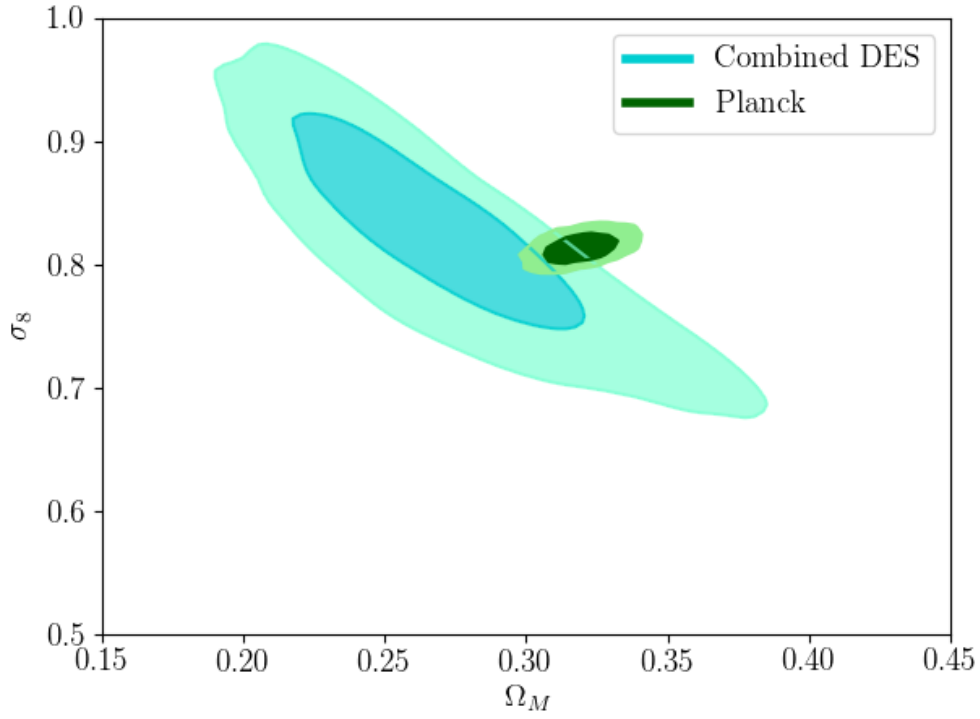

Figure 4.27: Comparing the combined results from Minkowski functionals + DESY1 with the Planck results.

Chapter 5

Future mass mapping applications

5.1 Y3 mapping

The Dark Energy Survey Year 1 introduced many new techniques and approaches. In subsequent years, the survey will provide weak lensing measurements over an area 3 times larger and with more galaxies, meaning that measurements will only improve. In this chapter, I will consider the potential of the next such data set to come available, that of Y3. The Y3 data has a similar galaxy density toe DESY1 in the previous chapter, but over the full DES footprint. This analysis is still ongoing, but the maturity of it allows for preliminary analysis with realistic simulations. All of the work presented in this chapter is my own, but the Y3 mapping effort will involve considerable effort from many across the collaboration.

5.1.1 DES Y3 simulations

As with the first year data, the mass reconstructions will be validated using Buzzard simulations introduced in Section 3.2.3. These were updated to cover the larger Y3 footprint. Mass maps were produced using both the forward fitting routine described in Chapter 3 and the direct inversion method from

Section 2.4.1 and compared to the known truth from the simulations. It was decided in the DES mass mapping group that the reference maps would now be made at an `nside` =128, so the following maps are all at this scale. In practice, this will improve the performance of the forward fitting algorithm when compared to the direct inversion even more, as the edge effects will be more dominant at this scale. These maps were chosen at this scale because of the range of methods now being employed in the Dark Energy Survey, some of which struggle at higher resolution. The level of shape noise in the maps is similar to that of Y1, so structures are only expected to be reliably detected at scales corresponding to `nside` =256.

5.1.2 Buzzard map reconstructions

The Buzzard simulations output a galaxy catalogue with similar properties to the Dark Energy Survey Year 3 data. These simulations were similar to those described in Section 3.2.3, but for evaluation of the reconstruction methods the cosmology of the true convergence field does not matter. A mass map was produced using both the direct inversion and the forward fitting pipeline using source galaxies in the redshift range $0.2 < z < 1.3$, pixelised on the sphere to produce localised shear estimates. Figure 5.1 shows mass maps made using the direct inversion and the forward fitting pipeline at an `nside` =128. Both maps show similar structures in the central regions of the mask, with some large κ values on the pereiphery of the direct inversion map, exhibiting behaviour similar to that seen in the Y1 footprint. The difference between the two maps is shown in Figure 5.3, i.e κ_{KS} - κ_{FF}, and Figure 5.2 shows the residuals for each reconstructed map when compared to the known true κ map. Both of these figures tell a similar story to that of the mass maps in DESY1, where the forward fitted map agrees well with that found from the direct inversion in the central areas of the mask, whereas on the outer regions of the mask where edge effects dominant, there is significant disagreement between the two methods. Further, when these areas of disagreement between the two methods are compared to the residuals with the true convergence

field, the forward fitted map is shown to be more accurately reconstructing the mass distribution in these areas of large disagreement. Unlike some of the DESY1 footprints analysed, the larger pixels and higher galaxy count in this simulation mean that there are no holes in the centre of the mask, so the direct inversion map only suffers from serious degradation around the edge of the mask. It will be interesting to see how smooth the final DESY3 map will be, and how this affects the mass maps produced.

Fidelity of the mass map reconstructions

Further to these visual comparisons, I have also performed some initial tests to quantify the accuracy of the reconstructions. Considering a Pearson correlation coefficient between the reconstructed map and the true κ map, the direct inversion finds a result of 0.52 and the forward fitted map has a value of 0.63, which is a similar level of disagreement to the Y1 Buzzard tests, which had values of 0.37 and 0.48 for the two approaches on the smaller but noisier Buzzard Y1 footprint. A combination of the complicated masking and reduced resolution serve to aggravate the edge effects in DESY3. In Chang et al. (2018), we produced our best case mass maps using the direct inversion by making maps at an `nside`=1024, and then smoothed the maps to lower resolutions as required. When this approach is used on the DESY3 data, the direct inversion can achieve a Pearson correlation coefficient of 0.6, which is significantly better than the transform at `nside` =128 but still worse than the forward fitted map, showing that the edge effects will still persist and cannot be completely removed.

Further, the probability distribution functions for the reconstructed maps can be compared to that of the true κ field in Figure 5.4, where the left hand plot shows the distribution for the reconstructed maps and the right hand plots show the residuals with the true field. Similar to as seen in chapter 3, the edge effects from the direct inversion introduce regions of large κ which significantly distort the PDF. These are visible at the tails of the mass map. In terms of the Jensen-Shannon divergence, introduced in Section 3.2.5, the

two distributions have values of $D_{JS} = 0.021$ for the direct inversion map and $D_{JS} = 0.011$ for the forward fitted map when compared to the true κ field. Approximately twice the information is lost in the direct inversion when compared to the forward fitted alternative, supporting the visual impression that the forward fitting approach performs significantly better at retaining information about the κ distribution.

This work analysing a realistic DESY3 data footprint highlights the upcoming challenges in producing reliable mass maps. Alternative reconstruction methods to the direct inversion will remain an important aspect of research in order to be able to produce accurate maps on future data sets.

5.2 Minkowski functionals

Following our analysis of Minkowski functionals for DESY1 in chapter 4, I will now examine their potential application to the DESY3 footprint.

Figure 5.5 shows the constraints that would be produced if it were possible to perfectly reconstruct the mass maps within the mask, without shape noise or edge effects. The figure shows the contours for both Buzzard Y1 and Y3 masks, indicating 68% and 95% confidence regions. The volume of the contour is noticeable smaller, and the constrains move from $\sigma_8 = 0.80^{+0.07}_{-0.08}, \Omega_M = 0.25^{+0.06}_{-0.08}$ for the Y1 footprint, to $\sigma_8 = 0.81^{+0.06}_{-0.07}, \Omega_M = 0.25^{+0.05}_{-0.07}$ for the Y3 footprint. This is due to the much larger area of the DESY3 footprint, which covers 5000 deg^2 compared to the smaller DESY1 area of 1400 deg^2. Unfortunately, as we do not recover the κ field perfectly, it is necessary to account for the effects of noise on the maps, and Figure 5.6 shows how the direct inversion influences the area of the confidence region. The masking of the DESY3 footprint is significantly more complicated than that of the Buzzard Y1 simulation, and our results in Section 5.1 have shown that there will be significant edge effects. There is a noticeable change in the size of both the 68% and 95% confidence regions due to including the transform, but the increase in constraining power due to the increased footprint in DESY3 means

that the the size of the contour remains smaller than that found for the best case, LSS sample variance limited DESY1 result. The constraints from DESY3 should still be much better than that for DESY1 when the shape noise is expected to be similar in the two datasets.

In Figure 5.7, I compare the 68% and 95% confidence regions found using Minkowski functionals for realistic simulations of the DESY3 data. Galaxy number density is taken from the Buzzard simulations and shape noise added in each pixel according to $0.3/\sqrt{N_{gal}}$. The same result is also shown for the Buzzard Y1 map, for comparison, with the Y3 result in blue and the true cosmology shown as the black star. There is a marked difference between the constraints found with each approach, where the Y3 result has a smaller fraction of the likelihood at lower and higher σ_8 values, meaning that constraints should be tigher relative to Y1 and suggests further promise when combined with other analyses. The potential of the Minkowski functionals to improve on measurements of these cosmological parameters mean that including them in cosmological analyses will become more important, as modern cosmology seeks to exactly quantify the level of agreement between low and high redshift probes of the Universe. To accurately include these results with two point analyses, it will be important to develop a more thorough evaluation of the covariance, but results in this thesis show that it is expected to be a fruitful endeavour.

5.2.1 The future for mass mapping

The motivations for studying and improving mass maps come from a variety of sources, and the future is exciting. The information that convergence maps contain beyond the two point analyses will make them vital additions to future surveys as they seek to probe non linear structure formation. Work in this thesis has shown the potential improvements Minkowski functionals can provide to cosmological constraints, and work such as Vicinanza et al. (2019) suggests that they will improve measurements on the next generation of surveys. Combined with peak statistics, they are a powerful tool for cosmology, and further analysis of the cosmological dependence of moments and the PDF provide a rich ground of further research. Mass maps are also useful for correlating with other observations, such as galaxies for examining the bias, and one of the most striking pieces of evidence for dark matter, the Bullet cluster, makes use of weak lensing mass maps through correlating with observable x-ray gas. As it becomes possible to make these maps across significant fractions of the sky, our tools will need updating to handle the requirements and produce maps that do justice to the data. As such, the forward fitting approach introduced in this thesis is one contribution to this goal, showing that we can now make superior maps on the sphere than previously achieved. Improving upon this approach to improve both angular and radial resolution will be a priority for upcoming mass mapping efforts, and it is easy to imagine a forward fitting approach that hypothesises the mass distribution through different redshift slices, potentially to the point where increases in the computing power available could lead to it being feasible for the lensing effect to be hypothesised for each galaxy individually.

Thomas Kuhn described scientific progress as being a series of "paradigm shifts", where the improvement of our knowledge is not a smooth linear increase, but by sporadic jumps caused by surprising results that challenge the status quo. For this purpose alone, analyses that allow us to examine the cosmos using new tools should always be encouraged. Once a sufficient body of work that contradicts the current paradigm is built up, there is a shift

towards a new approach. We may be witnessing the beginning of such a shift due to the persistence of H_0 and σ_8 tensions previously mentioned. Using mass maps, we can extract all of the information present in lensing studies to comprehensively conclude the existence of such tension. If disagreements between early and late time probes persist, we could be on the precipice of an exhilarating change of thought in cosmology.

5.3 Conclusions

In this thesis, I have introduced the current state of cosmology and the well tested ΛCDM model that is the favoured description of the Universe. Astronomical surveys have developed to the point where they are observing large numbers of galaxies across a significant fraction of the sky and out to distant redshifts. Combined with a well understood theory of gravity and equations governing the evolution of the Universe, the field has reached a point where fundamental properties of the Universe can be derived from these late time observations, and I have focused on the power of one such leading probe, weak lensing. Weak lensing causes coherent distortions in the shape of distant objects, and has the advantage of being indifferent to the properties of the lensing material, meaning it can detect non luminous matter. This is particularly useful as we believe the majority of matter in the Universe is dark matter, and reliable detection of its contribution to the Universe is one of the leading questions in the field.

The strength of the gravitational lensing effect can be measured by observing galaxy shapes, and detecting a preferential direction to the ellipticity. Using the well understood relationships between lensing distortions and the gravitational field from which they arise, it is possible to move from a map of the gravitational shear to maps of the underlying mass distribution. This provides us with an unbiased way to map the large scale structure in the Universe. In Chapter 2, I showed how these mass maps are usually made using the Kaiser-Squires direct inversion, and highlighted my contributions

to producing the Dark Energy Year 1 maps using the technique. The direct inversion is built upon the assumption of a shear field that is completely sampled and comprises of uniform noise. In modern surveys, these assumptions are not true and the resulting mass maps are less accurate than they could potentially be. To correct for this, in Chapter 3 I have introduced an approach which accounts for these two assumptions by forward fitting to observational data. This technique means it is possible to make mass maps across large fractions of the curved sky without introducing errors from the mass reconstruction method, and I have shown how the pipeline produces more accurate maps using a range of metrics.

In Chapter 4, I explored how these mass maps can be used to constrain two vital parameters that describe the Universe, Ω_M and σ_8, through the use of Minkowski functionals. These are particularly well suited to an application with mass maps as they are topological descriptors used to describe surfaces, and encode information that goes beyond that included in two point analyses. By using dark matter simulations in universes with different combinations of parameters, I built a library of the functionals and the parameters they related to. This library was then compared to simulated data sets and real survey maps, with a likelihood calculated for each set of parameters by comparing their simulated functionals to those from the observed map. I then constructed confidence regions for the two cosmological parameters and combined these with the likelihood from two point analysis to show the improvement in constraining power possible by including this extra information.

Finally, I showed the potential of these mass maps when applied to a data set similar to DES Y3, where the forward fitted maps produced significantly more reliable κ distributions than the direct inversion, and the Minkowski functionals are shown to be expected to provide tighter constraints with the larger footprint. In future, the information present in mass maps will be an important contribution for maximising the potential of cosmological surveys and ensuring the reliability of future results. This is of particular importance

at a time when late time probes are being compared to early time constraints from surveys such as Planck, and any disagreement between the two is being interpreted as indicative of an error in the ΛCDM model. In order to ensure our confidence in the standard cosmological model, it is necessary to test it with as many tools as possible, with a significant need to leave room for discovery in the case that our model is incorrect. Due to this, Minkowski functionals and mass maps from weak lensing play an important role in the field. In the future, surveys will have mapped the majority of the sky through significant fractions of the history of the Universe, and such fantastic data sets deserve to be maximally utilised.

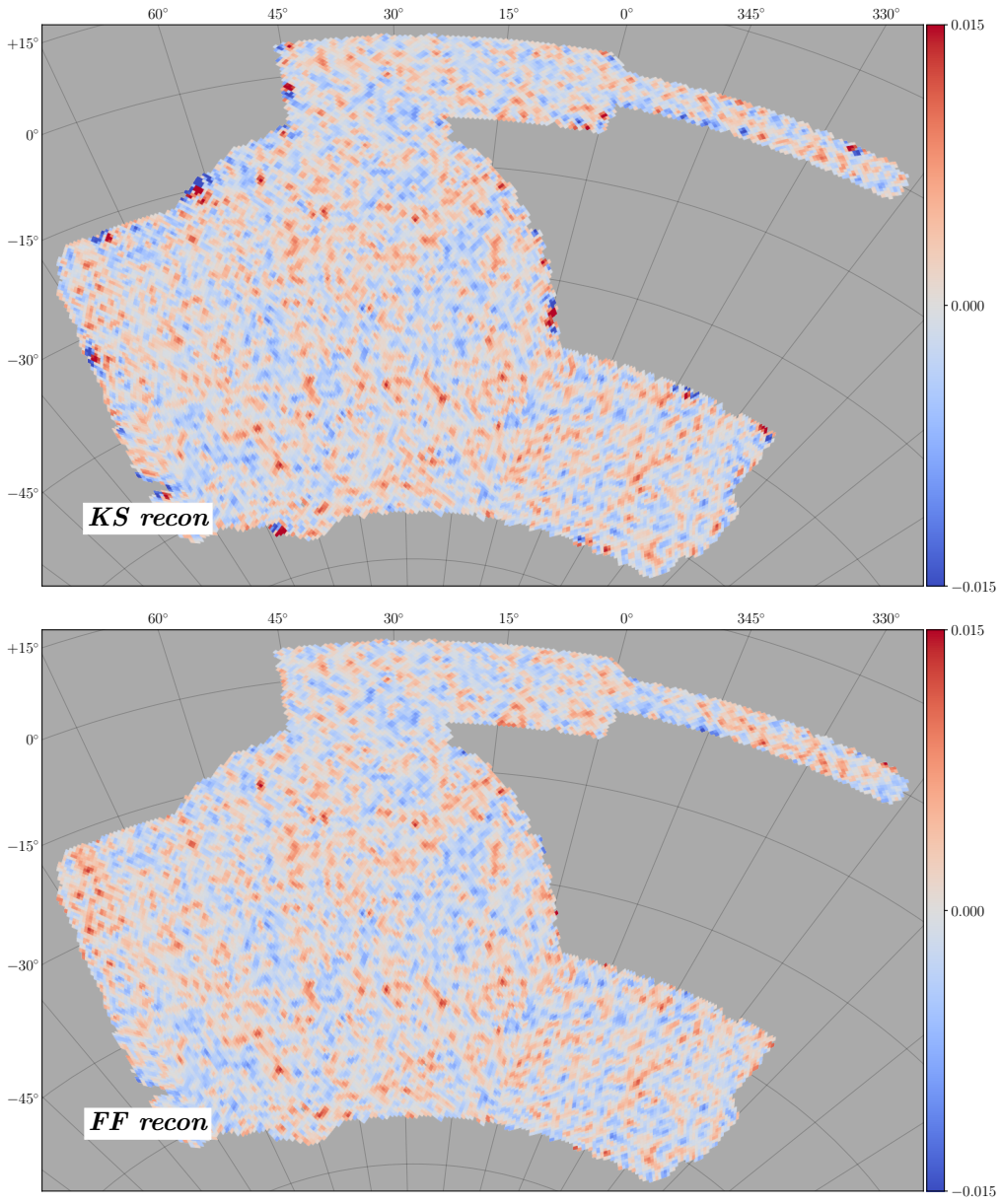

Figure 5.1: Comparing the two reconstructed mass maps using the direct inversion and the forward fitting algorithm at an `nside =128`.

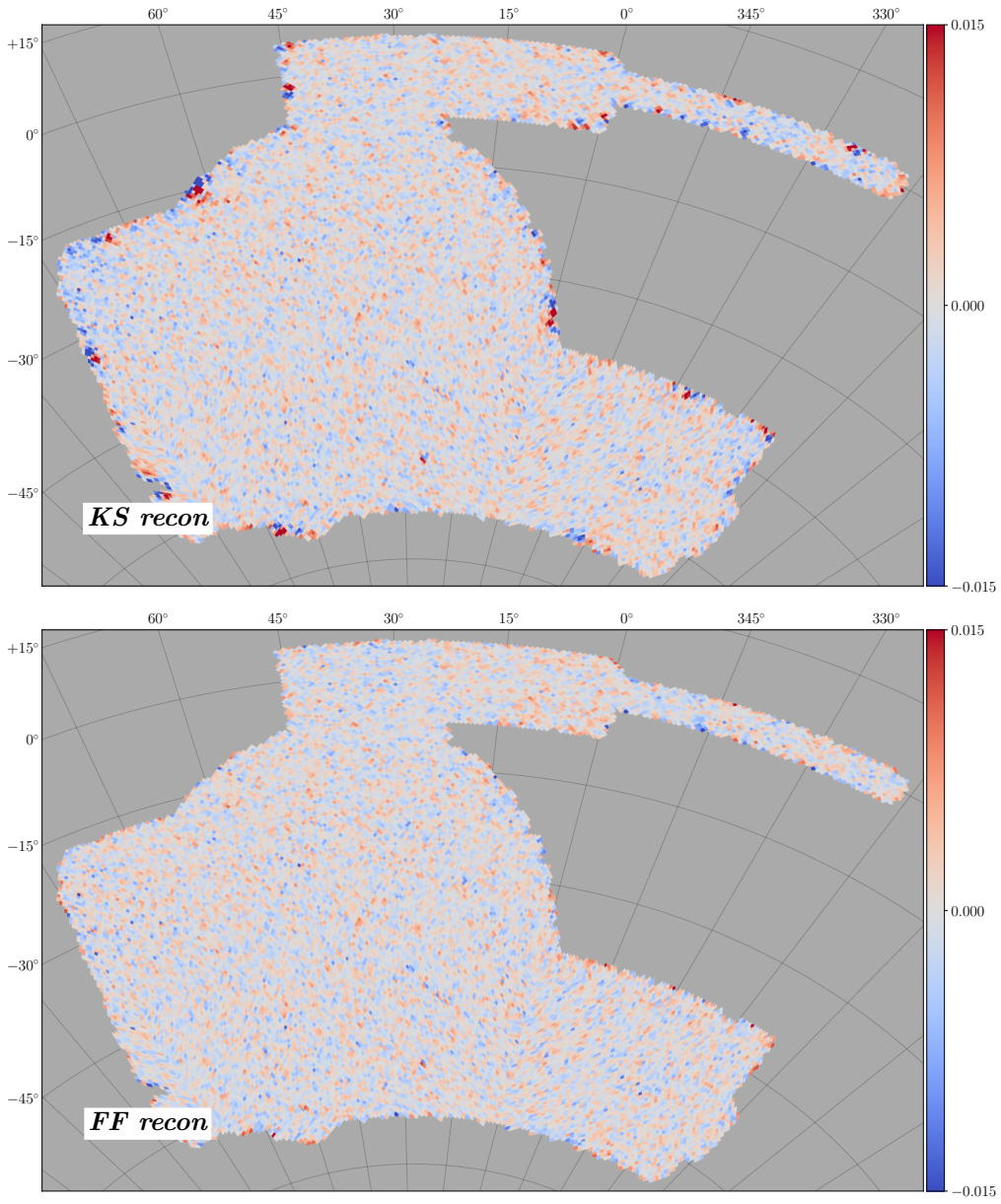

Figure 5.2: Comparing the residuals found for the two mass mapping methods using the Buzzard simulations for DESY3.

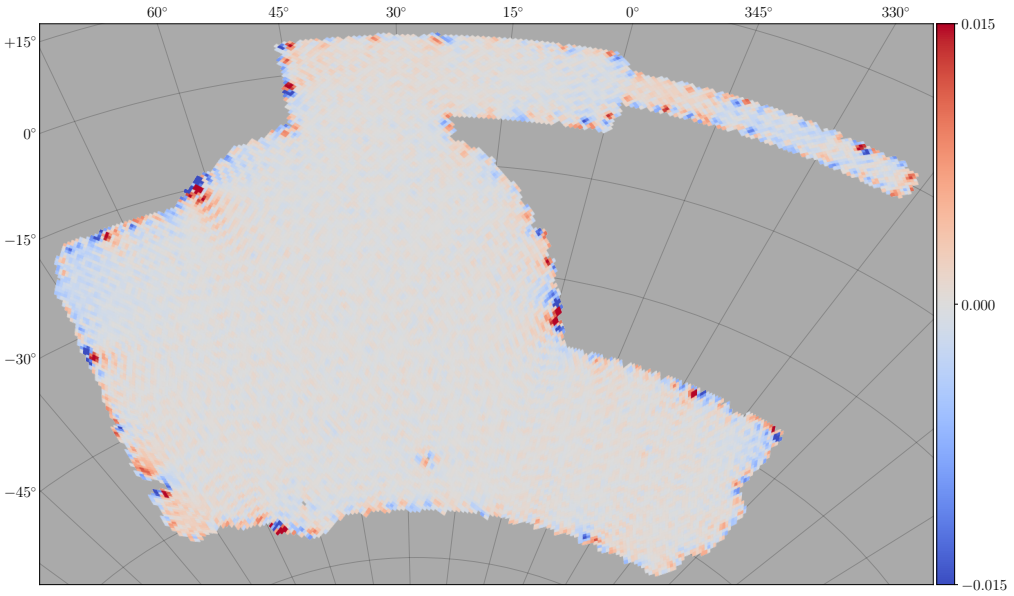

Figure 5.3: Subtracting the forward fitted map from that made using the direct inversion to highlight areas of disagreement.

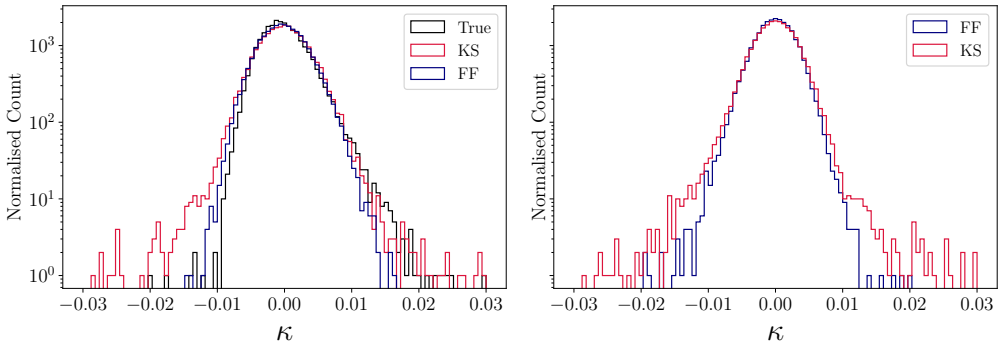

Figure 5.4: Considering the PDF of the reconstructed maps, compared to the known true distribution. The left hand plot shows the PDF for the two methods compared to the true field, and the right hand plot shows the residuals for each methods. In each plot, the edge effects for the direct inversion can be seen to cause signficant high κ deviations in the PDF, and visible in the maps shown previously. The forward fitted map performs significantly better in this regard, with residuals solely due to shape noise.

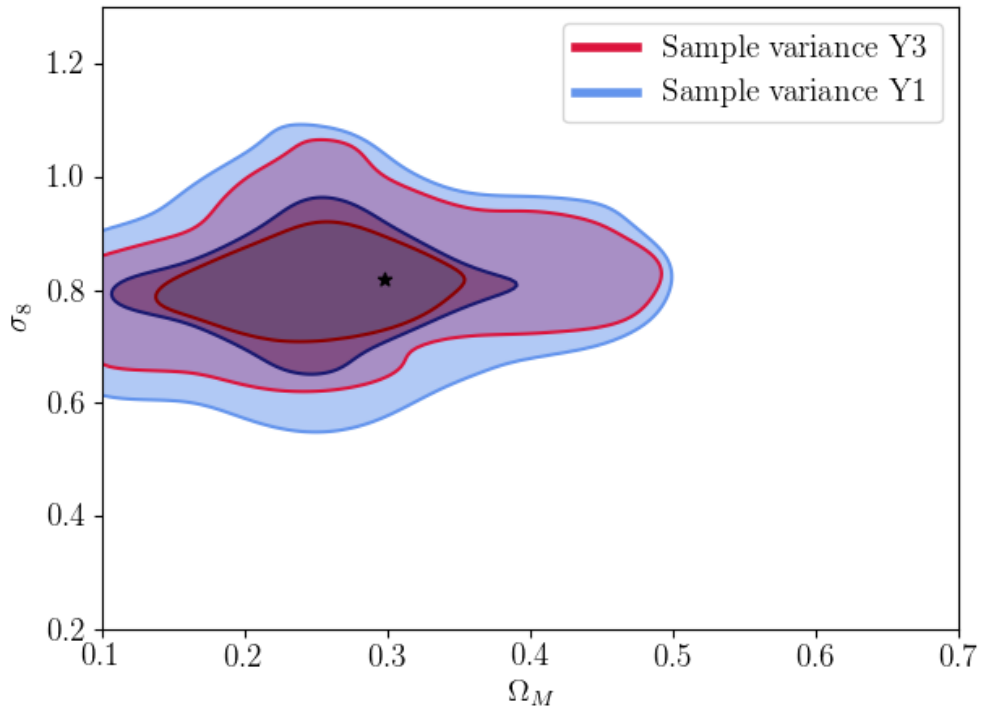

Figure 5.5: Examining the effect of the large scale structure sample variance on the measurement of the Minkowski functionals. The BuzzardY1 footprint is included for comparison, and the larger area of the Y3 data can be seen to reduce the area of the confidence region in Y3. Contours indicate regions of 68% and 95% confidence.

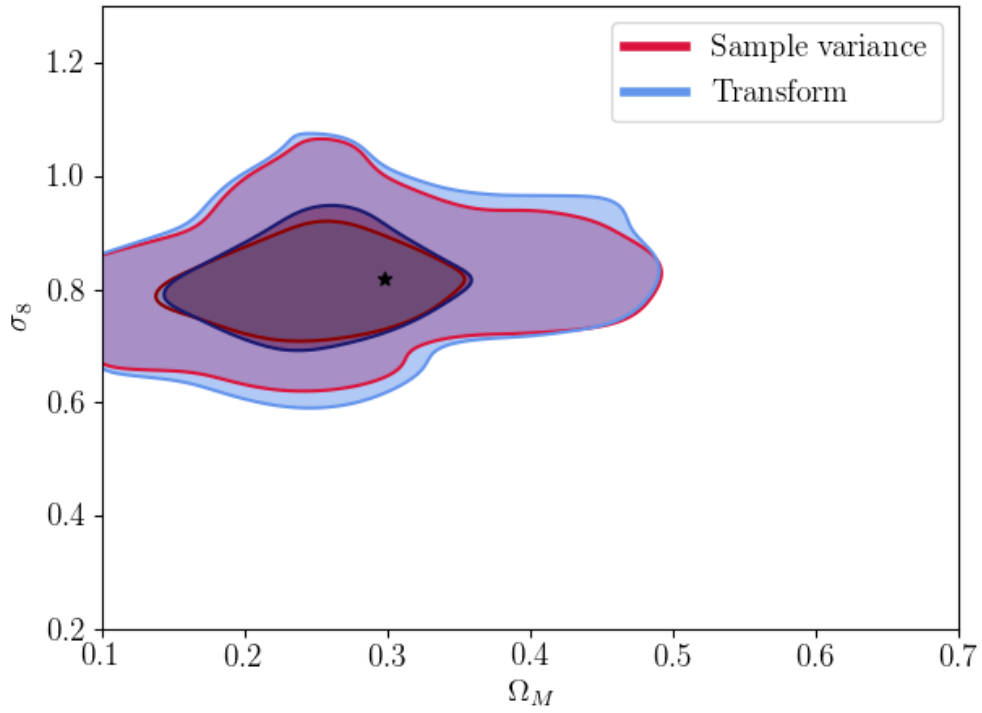

Figure 5.6: Demonstrating the effect of the direct inversion mass reconstruction on the Minkowski functionals when evaluating a DESY3 footprint. Mass maps were produced using noiseless shear on a masked sky. The contour is seen to expand, to a size similar to the LSS sample variance in Y1, as seen in Figure 5.5. Contours show areas representing 68% and 95% confidence regions.

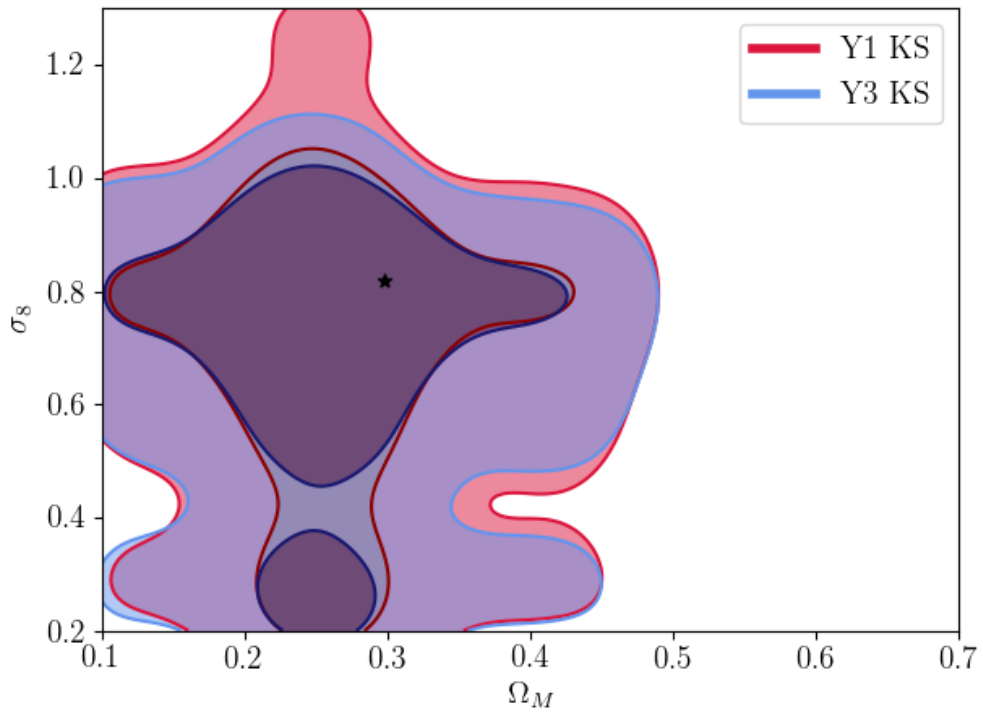

Figure 5.7: Comparing the confidence regions found using `L-PICOLA` simulations on a DESY3 Buzzard simulation footprint and that for the DESY1 Buzzard footprint. Despite the large scale structure sample variance being lower in the Y3 data set, the final contour has a significant contribution from shape noise that reduces the constraining power. The constraining power in the σ_8 direction appears to improve.

Appendix A

Modelling the noise in forward fitted mass maps

Accurate quantification of the uncertainties for pixels in the fitted convergence maps is integral to understanding their reliability.

A final fitted map is produced through averaging 40 maps resulting from our method pipeline. However, the error on the claimed convergence in each pixel of this final map is difficult to quantify. It might be thought that this could be well estimated from the standard deviation of the convergence across these 40 fits in a given pixel, but this is found, for edge pixels, to be much larger than the typical residuals between the final map and the true convergence.

This can be understood by noting that a good overall fit to the data can be obtained even if the relatively small number of edge pixel values are a poorer fit. Figure A.1 shows how the mean χ^2 of the fitted shear changes as a function of the distance from the edge of the map; edge pixels are consistently further from $\chi^2/n_{\rm pix} = 1$ in all of our fitted maps. This produces a larger spread of realisations of κ in these pixels, and its standard deviation therefore has a larger range than the residuals between mean maps and the truth, as shown in Figure A.2.

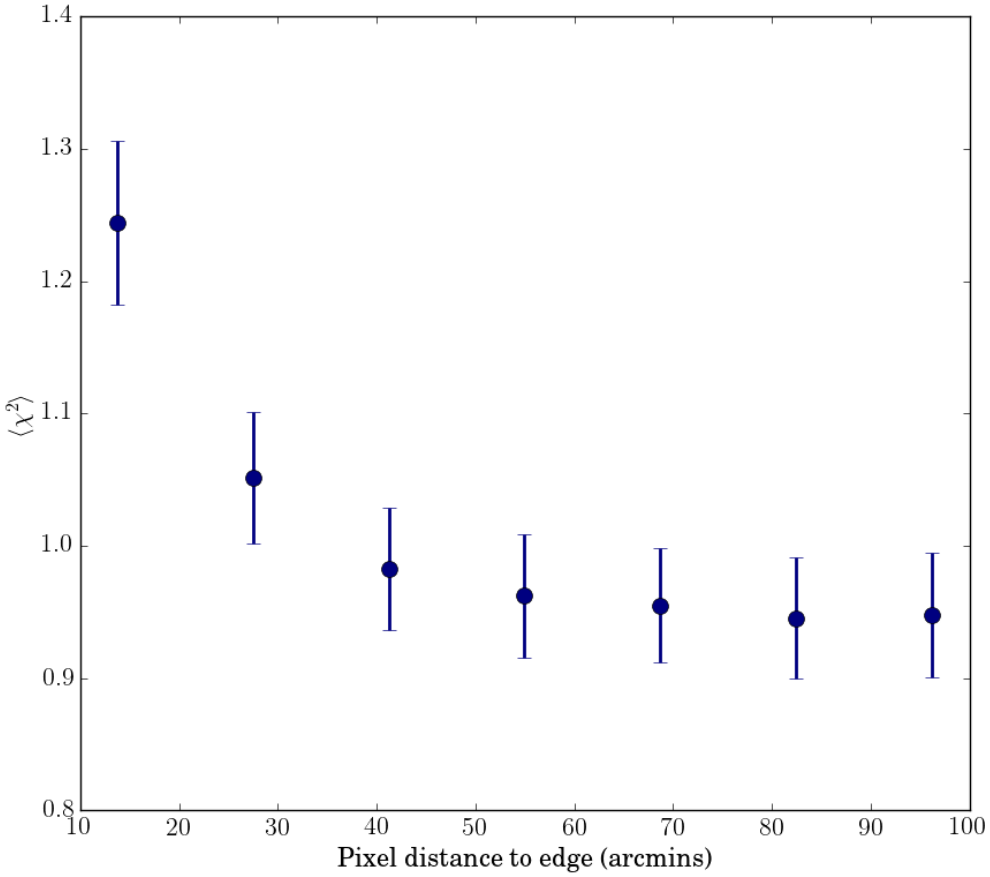

Figure A.1: The average χ^2 for a set of pixels, as a function of the distance of these pixels to the edge of the fitted region, is shown for an ensemble of fits. This highlights how the routine preferentially constrains γ values in the centre of the map at the expense of producing worse γ estimates in the outer areas of the map. The overall fit to all pixels has $\chi^2/n = 1$, but as can be seen this does not force the variance for an outer pixel to be the same as that in the central region of the map.

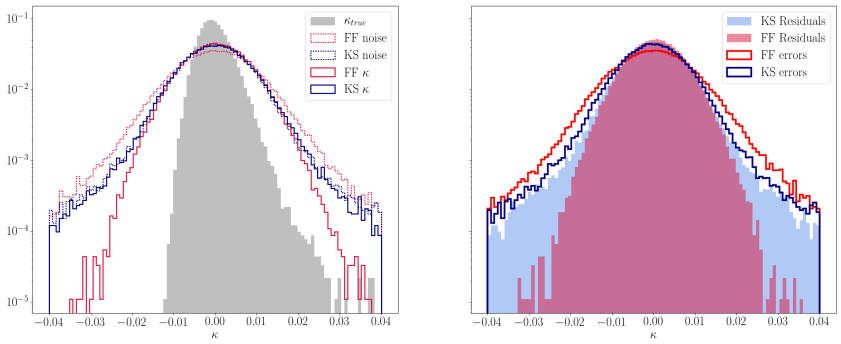

Figure A.2: Left: Distribution of convergence and associated noise for the Buzzard simulation and reconstruction. The solid lines represent reconstructed κ distributions for Buzzard. The dashed lines show expected noise, if we estimate error in each pixel from the standard deviation of κ values in an ensemble of reconstructions. Note that the dashed estimated noise distributions appear much wider than the solid reconstructed distributions (see text for explanation). Right: Distribution of noise estimated in two ways. The solid lines show the estimate from s.d. on κ from an ensemble of reconstructions. The filled regions show residuals directly measured between our mean reconstruction and the true convergence field.

Appendix B

UPR16 Form

FORM UPR16

Research Ethics Review Checklist

Please include this completed form as an appendix to your thesis (see the Research Degrees Operational Handbook for more information

UNIVERSITY OF PORTSMOUTH

Postgraduate Research Student (PGRS) Information			**Student ID:**	792522
PGRS Name:	BENJAMIN SAMUEL MAWDSLEY			
Department:	ICG	**First Supervisor:**	DAVID BACON	
Start Date: (or progression date for Prof Doc students)	**OCT 2015**			
Study Mode and Route:	Part-time ☐ Full-time ☒	MPhil ☐ PhD ☐	MD ☐ Professional Doctorate ☐	

Title of Thesis:	Mapping the Universe with weak lensing
Thesis Word Count: (excluding ancillary data)	31930

If you are unsure about any of the following, please contact the local representative on your Faculty Ethics Committee for advice. Please note that it is your responsibility to follow the University's Ethics Policy and any relevant University, academic or professional guidelines in the conduct of your study

Although the Ethics Committee may have given your study a favourable opinion, the final responsibility for the ethical conduct of this work lies with the researcher(s).

UKRIO Finished Research Checklist:
(If you would like to know more about the checklist, please see your Faculty or Departmental Ethics Committee rep or see the online version of the full checklist at: http://www.ukrio.org/what-we-do/code-of-practice-for-research/)

a)	Have all of your research and findings been reported accurately, honestly and within a reasonable time frame?	YES ☒ NO ☐
b)	Have all contributions to knowledge been acknowledged?	YES ☒ NO ☐
c)	Have you complied with all agreements relating to intellectual property, publication and authorship?	YES ☒ NO ☐
d)	Has your research data been retained in a secure and accessible form and will it remain so for the required duration?	YES ☒ NO ☐
e)	Does your research comply with all legal, ethical, and contractual requirements?	YES ☒ NO ☐

Candidate Statement:

I have considered the ethical dimensions of the above named research project, and have successfully obtained the necessary ethical approval(s)

Ethical review number(s) from Faculty Ethics Committee (or from NRES/SCREC):	E9B5-FB85-9E08-0E7A-7C69-7149-D963-6200

If you have *not* submitted your work for ethical review, and/or you have answered 'No' to one or more of questions a) to e), please explain below why this is so:

Signed *(PGRS)*: 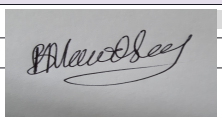 **Date:** 6/12/2019

UPR16 – April 2018

Appendix C

Ethical review

University of Portsmouth

Certificate of Ethics Review

Project Title:	Mapping the Universe with weak lensing
User ID:	792522
Name:	Benjamin Samuel Mawdsley
Application Date:	02/11/2017 11:42:43

You must download your certificate, print a copy and keep it as a record of this review.

It is your responsibility to adhere to the University Ethics Policy and any Department/School or professional guidelines in the conduct of your study including relevant guidelines regarding health and safety of researchers and University Health and Safety Policy.

It is also your responsibility to follow University guidance on Data Protection Policy:

- General guidance for all data protection issues
- University Data Protection Policy

You are reminded that as a University of Portsmouth Researcher you are bound by the UKRIO Code of Practice for Research; any breach of this code could lead to action being taken following the University's Procedure for the Investigation of Allegations of Misconduct in Research.

Any changes in the answers to the questions reflecting the design, management or conduct of the research over the course of the project must be notified to the Faculty Ethics Committee. **Any changes that affect the answers given in the questionnaire, not reported to the Faculty Ethics Committee, will invalidate this certificate.**

This ethical review should not be used to infer any comment on the academic merits or methodology of the project. If you have not already done so, you are advised to develop a clear protocol/proposal and ensure that it is independently reviewed by peers or others of appropriate standing. A favourable ethical opinion should not be perceived as permission to proceed with the research; there might be other matters of governance which require further consideration including the agreement of any organisation hosting the research.

GovernanceChecklist
A1-BriefDescriptionOfProject: Gravity can bend the path along which light travels, and change the apparent shape of distant galaxies. These slight changes in the shape of galaxies are due to an effect that we call weak lensing, and this project will use this effect to produce maps of the distribution of matter in the Universe using observations of the sky. I will use a combination of established mapping techniques and new routines to try and produce these maps, and study what can be learnt from them.
A2-Faculty: Technology
A3-VoluntarilyReferToFEC: No
A5-AlreadyExternallyReviewed: No

Certificate Code: E9B5-FB85-9E08-0E7A-7C69-7149-D963-6200 Page 1

B1-HumanParticipants: No
HumanParticipantsDefinition
B2-HumanParticipantsConfirmation: Yes
C6-SafetyRisksBeyondAssessment: No
SafetyRisksBeyondAssessmentWarning
D2-PhysicalEcologicalDamage: No
PhysicalEcologicalDamageWarning
D4-HistoricalOrCulturalDamage: No
HistoricalOrCulturalDamageWarning
E1-ContentiousOrIllegal: No
ContentiousOrIllegalWarning
E2-SociallySensitiveIssues: No
SociallySensitiveWarning
F1-InvolvesAnimals: No
InvolvesAnimalsWarning
F2-HarmfulToThirdParties: No
HarmfulToThirdPartiesWarning
G1-ConfirmReadEthicsPolicy: Confirmed
G2-ConfirmReadUKRIOCodeOfPractice: Confirmed
G3-ConfirmReadConcordatToSupportResearchIntegrity: Confirmed
G4-ConfirmedCorrectInformation: Confirmed

Bibliography

Abbott T. M. C., et al., 2018, Phys. Rev. D, 98, 043526

Adelman-McCarthy J. K., et al., 2008, ApJS, 175, 297

Ahmad Q. R., et al., 2001, Phys. Rev. Lett., 87, 071301

Alam S., et al., 2017, Monthly Notices of the Royal Astronomical Society, 470, 2617

Alcock C., et al., 2000a, ApJ, 541, 270

Alcock C., et al., 2000b, ApJ, 542, 281

Bacon D. J., Refregier A. R., Ellis R. S., 2000, MNRAS, 318, 625

Bartelmann M., Schneider P., 2001, Phys. Rept., 340, 291

Becker M. R., 2013, Monthly Notices of the Royal Astronomical Society, 435, 115

Benítez N., 2000, ApJ, 536, 571

Bernstein G., Huterer D., 2010, MNRAS, 401, 1399

Beutler F., et al., 2016, Monthly Notices of the Royal Astronomical Society, 464, 3409

Blandford R. D., Saust A. B., Brainerd T. G., Villumsen J. V., 1991, MNRAS, 251, 600

Böhm V., Hilbert S., Greiner M., Enßlin T. A., 2017, PhysRevD, 96, 123510

Bonnett C., et al., 2016, Phys. Rev. D, 94, 042005

Bonvin V., et al., 2016, Monthly Notices of the Royal Astronomical Society, 465, 4914

Bouchet F. R., Colombi S., Hivon E., Juszkiewicz R., 1995, Astronomy and Astrophysics, 296, 575

Bridle S., King L., 2007, New Journal of Physics, 9, 444

Bruzual G., Charlot S., 2003, Monthly Notices of the Royal Astronomical Society, 344, 1000

Carter P., Beutler F., Percival W. J., Blake C., Koda J., Ross A. J., 2018, MNRAS, 481, 2371

Castro P. G., Heavens A. F., Kitching T. D., 2005, Phys. Rev. D, 72, 023516

Catelan P., Kamionkowski M., Blandford R. D., 2001a, Monthly Notices of the Royal Astronomical Society, 320, L7

Catelan P., Kamionkowski M., Blandford R. D., 2001b, Monthly Notices of the Royal Astronomical Society, 320, L7

Cawthon R., et al., 2017, Submitted to: Mon. Not. Roy. Astron. Soc.

Chang C., Jain B., 2014, Monthly Notices of the Royal Astronomical Society, 443, 102

Chang C., et al., 2015, Phys. Rev. Lett., 115, 051301

Chang C., et al., 2018, Monthly Notices of the Royal Astronomical Society, 475, 3165

Chisari N. E., Dvorkin C., 2013, Journal of Cosmology and Astroparticle Physics, 2013, 029

Clerkin L., Kirk D., Lahav O., Abdalla F. B., Gaztañaga E., 2015, MNRAS, 448, 1389

Clowe D., Gonzalez A., Markevitch M., 2004, ApJ, 604, 596

Coe D., Benítez N., Sánchez S. F., Jee M., Bouwens R., Ford H., 2006, Astronomical Journal, 132, 926

Coleman G. D., Wu C.-C., Weedman D. W., 1980, ApJS, 43, 393

Conley A., Carlberg R. G., Guy J., Howell D. A., Jha S., Riess A. G., Sullivan M., 2007, ApJl, 664, L13

Conroy C., Wechsler R. H., Kravtsov A. V., 2006, The Astrophysical Journal, 647, 201

Crittenden R. G., Turok N. G., eds, 2001, Structure formation in the universe Vol. 565

Crocce M., Pueblas S., Scoccimarro R., 2006, Monthly Notices of the Royal Astronomical Society, 373, 369

Davis C., et al., 2017, Submitted to: Mon. Not. Roy. Astron. Soc.

De Rham C., Gabadadze G., Tolley A. J., 2011, Phys. Rev. Lett., 106, 231101

DeRose J., et al., 2019, arXiv e-prints, p. arXiv:1901.02401

Dietrich J. P., Hartlap J., 2010, Monthly Notices of the Royal Astronomical Society, 402, 1049

Dodelson S., 2003, Modern Cosmology. Academic Press

Dodelson S., Zhang P., 2005, Phys. Rev. D, 72, 083001

Drlica-Wagner A., et al., 2018, Astrophys. J. Suppl., 235, 33

Einstein A., 1915, Sitzungsberichte der Königlich Preußischen Akademie der Wissenschaften (Berlin, pp 844–847

Eisenstein D. J., Seo H.-J., Sirko E., Spergel D. N., 2007, The Astrophysical Journal, 664, 675

Flaugher B., et al., 2015, The Astronomical Journal, 150, 150

Fluri J., Kacprzak T., Sgier R., Refregier A., Amara A., 2018, Journal of Cosmology and Astroparticle Physics, 2018, 051

Friedmann A., 1922, Zeitschrift fur Physik, 10, 377

Gatti M., et al., 2017, Submitted to: Mon. Not. Roy. Astron. Soc.

Gatti M., et al., 2019, arXiv e-prints, p. arXiv:1911.05568

Górski K. M., Hivon E., Banday A. J., Wandelt B. D., Hansen F. K., Reinecke M., Bartelmann M., 2005, ApJ, 622, 759

Guy J., et al., 2007, Astronomy and Astrophysics, 466, 11

Hamilton A. J. S., 1998, Linear Redshift Distortions: a Review. Kluwer Academic, p. 185, doi:10.1007/978-94-011-4960-0˙17

Heavens A., 2003, Monthly Notices of the Royal Astronomical Society, 343, 1327

Heymans C., Heavens A., 2003, arXiv e-prints, pp astro–ph/0310495

Heymans C., et al., 2012, MNRAS, 427, 146

Hikage C., Komatsu E., Matsubara T., 2006, ApJ, 653, 11

Hikage C., et al., 2019, Publications of the ASJ, 71, 43

Hilbert S., Xu D., Schneider P., Springel V., Vogelsberger M., Hernquist L., 2017, MNRAS, 468, 790

Hildebrandt H., et al., 2017, MNRAS, 465, 1454

Hildebrandt H., et al., 2018, arXiv e-prints, p. arXiv:1812.06076

Hirata C., Seljak U., 2003, Monthly Notices of the Royal Astronomical Society, 343, 459

Hirata C. M., Seljak U. c. v., 2004, Phys. Rev. D, 70, 063526

Horndeski G. W., 1974, International Journal of Theoretical Physics, 10, 363

Howlett C., Manera M., Percival W. J., 2015, Astronomy and Computing, 12, 109

Hoyle B., et al., 2018, Monthly Notices of the Royal Astronomical Society, 478, 592

Hubble E., 1929, Proceedings of the National Academy of Sciences, 15, 168

Huff E., Mandelbaum R., 2017, arXiv e-prints, p. arXiv:1702.02600

Hull M., Koyama K., Tasinato G., 2016, Phys. Rev., D93, 064012

Humphreys E. M. L., Reid M. J., Moran J. M., Greenhill L. J., Argon A. L., 2013, The Astrophysical Journal, 775, 13

Isserlis L., 1918, Biometrika, 12, 134

Izard A., Fosalba P., Crocce M., 2018, MNRAS, 473, 3051

Jarvis M., et al., 2016, Monthly Notices of the Royal Astronomical Society, 460, 2245

Jeffrey N., et al., 2018, Submitted to: Mon. Not. Roy. Astron. Soc.

Joachimi B., Semboloni E., Hilbert S., Bett P. E., Hartlap J., Hoekstra H., Schneider P., 2013, Monthly Notices of the Royal Astronomical Society, 436, 819

Joachimi B., et al., 2015, Space Science Reviews, 193, 1

Kacprzak T., et al., 2016, Monthly Notices of the Royal Astronomical Society, 463, 3653

Kaiser N., 1987, Mon. Not. Roy. Astron. Soc., 227, 1

Kaiser N., Squires G., 1993, ApJ, 404, 441

Kenna-Allison M., GümrükçüoÇ§lu A. E., Koyama K., 2019, PhysRevD, 99, 104032

Kerscher M., Schmalzing J., Buchert T., 1996, in Coles P., Martinez V., Pons-Borderia M.-J., eds, Astronomical Society of the Pacific Conference Series Vol. 94, Mapping, Measuring, and Modelling the Universe. p. 247 (arXiv:astro-ph/9512105)

King, L. J. Schneider, P. 2003, A&A, 398, 23

Kinney A. L., Calzetti D., Bohlin R. C., McQuade K., Storchi-Bergmann T., Schmitt H. R., 1996, ApJ, 467, 38

Kirk D., et al., 2015, Space Science Reviews, 193, 139

Kitching T. D., et al., 2014, Monthly Notices of the Royal Astronomical Society, 442, 1326

Koyama K., 2008, General Relativity and Gravitation, 40, 421

Koyama K., 2016, Reports on Progress in Physics, 79, 046902

Kratochvil J. M., Haiman Z., May M., 2010, Phys. Rev. D, 81, 043519

Kullback S., Leibler R. A., 1951, Ann. Math. Statist., 22, 79

Laigle C., et al., 2016, Astrophys. J. Suppl., 224, 24

Lanusse F., Starck J.-L., Leonard A., Pires S., 2016, Astronomy and Astrophysics, 591, A2

Leistedt B., et al., 2016, ApJS, 226, 24

Leistedt B., McEwen J. D., BÃ$\frac{1}{4}$ttner M., Peiris H. V., 2017, Monthly Notices of the Royal Astronomical Society, 466, 3728

Lemaître G., 1927, Annales de la Société Scientifique de Bruxelles, 47, 49

Lesgourgues J., 2011, arXiv e-prints, p. arXiv:1104.2932

Lewis A., Bridle S., 2002a, PhysRevD, 66, 103511

Lewis A., Bridle S., 2002b, Phys. Rev., D66, 103511

Linton M. S., Pourtsidou A., Crittenden R., Maartens R., 2018, Journal of Cosmology and Astroparticle Physics, 2018, 043

Liu J., Petri A., Haiman Z., Hui L., Kratochvil J. M., May M., 2015, PhysRevD, 91, 063507

Ma Z., Hu W., Huterer D., 2006, The Astrophysical Journal, 636, 21

Macaulay E., et al., 2019, MNRAS, 486, 2184

Mackey J., White M., Kamionkowski M., 2002, Monthly Notices of the Royal Astronomical Society, 332, 788

Mandelbaum R., et al., 2015, Monthly Notices of the Royal Astronomical Society, 450, 2963

Manzotti A., et al., 2017, ApJ, 846, 45

Marian L., Bernstein G. M., 2007, Phys. Rev. D, 76, 123009

Massey R., et al., 2007, Nature, 445, 286

Mawdsley B., et al., 2019, arXiv e-prints, p. arXiv:1905.12682

Mecke K. R., Buchert T., Wagner H., 1994a, Astron. Astrophys., 288, 697

Mecke K. R., Buchert T., Wagner H., 1994b, Astronomy and Astrophysics, 288, 697

Moore T., 2012, A General Relativity Workbook. University Science Books, https://books.google.co.uk/books?id=L-CAMAEACAAJ

Munshi D., van Waerbeke L., Smidt J., Coles P., 2012, MNRAS, 419, 536

NASA/Chandra 2006, Bullet Cluster, https://chandra.harvard.edu/photo/2006/1e0657/more.html

Newman J. A., 2008, ApJ, 684, 88

Niikura H., et al., 2019, Nature Astronomy, 3, 524

Oguri M., et al., 2017, Publications of the Astronomical Society of Japan, 70

Patton K., Blazek J., Honscheid K., Huff E., Melchior P., Ross A. J., Suchyta E., 2017, Mon. Not. Roy. Astron. Soc., 472, 439

Peacock J. A., 1998, Cosmological Physics. Cambridge University Press, doi:10.1017/CBO9780511804533

Penzias A. A., Wilson R. W., 1965, ApJ, 142, 419

Percival W. J., 2013, arXiv e-prints, p. arXiv:1312.5490

Perlmutter S., et al., 1999, ApJ, 517, 565

Petri A., Haiman Z., Hui L., May M., Kratochvil J. M., 2013, Phys. Rev. D, 88, 123002

Petri A., Liu J., Haiman Z., May M., Hui L., Kratochvil J. M., 2015, Phys. Rev., D91, 103511

Phillips M. M., 1993, ApJl, 413, L105

Pietrzyński G., et al., 2013, Nature, 495, 76

Pires S., Starck J. L., Amara A., Teyssier R., Réfrégier A., Fadili J., 2009, MNRAS, 395, 1265

Planck Collaboration et al., 2018, arXiv e-prints, p. arXiv:1807.06209

Pskovskii I. P., 1977, Soviet Astronomy, 21, 675

Pskovskii Y. P., 1984, Soviet Astronomy, 28, 658

Quinn T., Katz N., Stadel J., Lake G., 1997, arXiv e-prints, pp astro–ph/9710043

Reddick R. M., Wechsler R. H., Tinker J. L., Behroozi P. S., 2013, ApJ, 771, 30

Riess A. G., Press W. H., Kirshner R. P., 1996, ApJ, 473, 88

Riess A. G., et al., 1998, Astronomical Journal, 116, 1009

Riess A. G., et al., 2018, ApJ, 855, 136

Rozo E., et al., 2016, Monthly Notices of the Royal Astronomical Society, 461, 1431

Rykoff E. S., et al., 2016, The Astrophysical Journal Supplement Series, 224, 1

Samuroff S., et al., 2019, MNRAS, 489, 5453

Schaye J., et al., 2015, MNRAS, 446, 521

Schmalzing J., Górski K. M., 1997, Monthly Notices of the Royal Astronomical Society, 297, 355

Schmalzing J., Kerscher M., Buchert T., 1996, in Bonometto S., Primack J. R., Provenzale A., eds, Dark Matter in the Universe. p. 281 (arXiv:astro-ph/9508154)

Schneider P., Seitz C., 1995, Astronomy and Astrophysics, 294, 411

Scoccimarro R., 1998, MNRAS, 299, 1097

Seitz C., Schneider P., 1995, Astronomy and Astrophysics, 297, 287

Seitz S., Schneider P., 1998, ArXiv Astrophysics e-prints,

Serjeant S., 2010, Observational Cosmology. Cambridge University Press

Shannon C. E., 1948, Bell System Technical Journal, 27, 379

Sheldon E., 2015, NGMIX: Gaussian mixture models for 2D images, Astrophysics Source Code Library (ascl:1508.008)

Springel V., 2005a, Monthly Notices of the Royal Astronomical Society, 364, 1105

Springel V., 2005b, Monthly Notices of the Royal Astronomical Society, 364, 1105

Starck J.-L., Fadili M.-J., Murtagh F., 2007, IEEE Transactions on Image Processing, 16, 297

Starck J.-L., Murtagh F., Fadili J., 2015, Sparse Image and Signal Processing: Wavelets and Related Geometric Multiscale Analysis, 2 edn. Cambridge University Press, doi:10.1017/CBO9781316104514

Tassev S., Eisenstein D. J., Wand elt B. D., Zaldarriaga M., 2015, arXiv e-prints, p. arXiv:1502.07751

Troxel M., Ishak M., 2015, Physics Reports, 558, 1

Troxel M. A., et al., 2018a, PhysRevD, 98, 043528

Troxel M. A., et al., 2018b, MNRAS, 479, 4998

Van Waerbeke L., et al., 2000, Astronomy and Astrophysics, 358, 30

Van Waerbeke L., et al., 2013, Monthly Notices of the Royal Astronomical Society, 433, 3373

Vicinanza M., Cardone V. F., Maoli R., Scaramella R., Er X., Tereno I., 2019, PhysRevD, 99, 043534

Vikram V., et al., 2015, Phys. Rev., D92, 022006

Wallis C. G. R., McEwen J. D., Kitching T. D., Leistedt B., Plouviez A., 2017, arXiv e-prints, p. arXiv:1703.09233

Wittman D. M., Tyson J. A., Kirkman D., Dell'Antonio I., Bernstein G., 2000, Nature, 405, 143

Wright B. S., Koyama K., Winther H. A., Zhao G.-B., 2019, Journal of Cosmology and Astroparticle Physics, 2019, 040

Yang X., Kratochvil J. M., Wang S., Lim E. A., Haiman Z., May M., 2011, Phys. Rev. D, 84, 043529

Zhao G.-B., et al., 2017, Nature Astronomy, 1, 627

Zuntz J., Kacprzak T., Voigt L., Hirsch M., Rowe B., Bridle S., 2013, MNRAS, 434, 1604

Zuntz J., et al., 2015, Astronomy and Computing, 12, 45

Zuntz J., et al., 2017, Submitted to: Mon. Not. Roy. Astron. Soc.

Zuntz J., et al., 2018, MNRAS, 481, 1149